

DEPARTMENT OF PHYSICS, UNIVERSITY OF JYVÄSKYLÄ

**JET TRANSVERSE MOMENTUM DISTRIBUTIONS
MEASURED BY ALICE**

**BY
TOMAS SNELLMAN**

PHD thesis

Supervisors: Jan Rak, Dong Jo Kim

Jyväskylä, Finland
December, 2018

3 Contents

4 1 Introduction	8
5 1.1 Quantum chromodynamics	9
6 1.1.1 Foundation of QCD	9
7 1.1.2 Asymptotic Freedom	10
8 1.2 heavy-ion physics	14
9 1.2.1 History	14
10 1.3 Features of Heavy-Ion Collisions	16
11 1.3.1 Collision Geometry	16
12 1.3.2 Nuclear Geometry	17
13 1.3.3 Hydrodynamical Modelling	20
14 1.4 Flow	23
15 1.4.1 Anisotropic Flow	24
16 1.5 Hard processes	25
17 1.5.1 pQCD factorization	25
18 1.5.2 Jet hadronisation	28
19 1.5.3 Jet energy loss	32
20 1.5.4 New paradigm of jet Quenching	38
21 1.5.5 Jet shape measurements	41
22 1.6 QGP in Small systems	41
23 1.6.1 Collective phenomena	43
24 1.6.2 Absence of jet quenching	44
25 1.6.3 Centrality determination in small systems	44
26 2 Experimental Setup	48
27 2.1 CERN	48
28 2.2 Large Hadron Collider	49
29 2.2.1 LHC experiments	50
30 2.3 ALICE	51
31 2.3.1 Tracking	52
32 2.3.2 TPC	54
33 2.3.3 TPC upgrade	54
34 2.3.4 Particle identification	58
35 2.3.5 Electromagnetic Calorimeter	59
36 2.3.6 Forward and trigger detectors	59
37 2.3.7 Muon spectrometer	62

38	2.3.8 Triggers	62
39	3 Event and track selection	65
40	3.1 Event selection	65
41	3.2 Track selection	65
42	3.3 Cluster selection	67
43	4 Analysis method	68
44	4.1 Jet Finding	68
45	4.1.1 Anti k_T algorithm	69
46	4.2 Definition of j_T	70
47	4.3 Unfolding detector effects	71
48	4.3.1 Bayesian unfolding	73
49	4.3.2 Toy Monte Carlo	75
50	4.3.3 Pythia Response matrices	75
51	4.3.4 Unfolding algorithm	77
52	4.3.5 Unfolding closure test	77
53	4.4 Background	80
54	4.4.1 Perpendicular cone background	80
55	4.4.2 Random background	80
56	4.4.3 Auto-correlations	82
57	4.4.4 Background methods	82
58	4.5 Fitting	82
59	5 Systematic errors	85
60	5.1 Background	85
61	5.2 Unfolding	85
62	5.2.1 Effect of number of iterations	86
63	5.2.2 Effect of different prior	88
64	5.2.3 Effect of p_T truncation	88
65	5.3 Tracking	89
66	5.4 EMCal clusters	90
67	5.5 Summary/Combining systematics	90
68	5.6 Additional checks	91
69	5.6.1 Comparison between A and C side	91
70	6 Results	93
71	6.1 Fitting	93
72	6.1.1 RMS values from fitted distributions	93
73	6.2 High multiplicity	93

⁷⁴	7	Discussion	96
⁷⁵	7.1	Dihadron j_T	96
⁷⁶	7.2	Comparing dihadron and jet j_T results	97
⁷⁷	7.2.1	Different R parameters	98
⁷⁸	7.2.2	Leading tracks versus jet	99
⁷⁹	8	Summary	101
⁸⁰	Appendices		102
⁸¹	A	Additional graphs	102

⁸² List of Figures

⁸³	1	QCD phase diagram	12
⁸⁴	2	η/s vs $(T - T_c)/T_c$	13
⁸⁵	3	The definitions of the Reaction Plane and Participant Plane coordinate systems	16
⁸⁶	4	Interaction between partons in central and peripheral collisions.	17
⁸⁷	5	An illustration of the multiplicity distribution in ALICE measurement with centrality classes.	18
⁸⁸	6	The results of one Glauber Monte Carlo simulation.	21
⁸⁹	7	Schematic representation of a heavy-ion collision	22
⁹⁰	8	Charged particle spectra	23
⁹¹	9	Illustration of flow in momentum space in central and peripheral collisions.	24
⁹²	10	QCD Leading Order	26
⁹³	11	Hard scattering	27
⁹⁴	12	Jet showering	28
⁹⁵	15	Measurements of the nuclear modification factor R_{AA} in central heavy-ion collisions	33
⁹⁶	16	A comparison between observed $R_{AA}(\Delta\phi, p_T)$ and R_{AA} using v_2	34
⁹⁷	17	Elliptic flow, v_2 from $p_T = 1$ to 60 GeV/c	35
⁹⁸	18	Photon spectrum	37
⁹⁹	20	Calculations of the intial energy density in small collision systems at RHIC and the resulting hydrodynamic evolution.	42
¹⁰⁰	21	Two-particle correlation results in PbPb, pPb, and pp collisions at the LHC [].	43
¹⁰¹	22	RpA in proton-lead collisions	45

108	23	Distribution of the sum of amplitudes in the V0A hodoscopes (Pb-going), as well as the NBD-Glauber fit (explained in the text). Centrality classes are indicated by vertical lines. The inset shows a zoom-in on the most peripheral events. [1]	46
112	24	Top: Scatter plot of number of participating nucleons versus impact parameter; Bottom: Scatter plot of multiplicity versus the number of participating nucleons from the Glauber fit for V0A. The quantities are calculated with a Glauber Monte Carlo of p-Pb (left) and Pb-Pb (right) collisions. [1]	47
117	25	CERN collider complex	48
118	26	ALICE	52
119	27	ITS	53
120	28	TPC	55
121	29	<i>left</i> Cross-section of a GEM foil. (Not to scale). The hole diameters are $d_{\text{in}} = 50 \pm 5 \mu\text{m}$ and $d_{\text{out}} = 70 \pm 5 \mu\text{m}$ and pitch is either 140 or 280 μm . <i>right</i> The amplification of a GEM foil is based on the Townsend avalanche phenomenon. Electrons entering the electric field inside the hole are accelerated.	56
126	30	The EMCal detector arc, where the segmentation into 10 full size and 2 $1/3$ -sized (5 and 1 per side) supermodules can be seen.	60
128	31	The exploded EMCal tower view	61
129	32	A simple example of the antil- k_T algorithm in progress. The red tracks in the leftmost figure are identified to have the smallest $k_{T,i}$ in the event and are combined into the red track of the middle figure. As this continues the remaining tracks are added to this or other jets. One tracks was deemed to be isolated enough to be counted as a protojet by itself. Note that the rightmost figure is zoomed out.	70
135	33	Illustration of \vec{j}_T . The jet fragmentation transverse momentum, \vec{j}_T , is defined as the transverse momentum component of the track momentum, \vec{p}_{track} , with respect to the jet momentum, \vec{p}_{jet}	71
138	34	Inclusive j_T with background	72
139	35	Results from unfolding in Toy Monte Carlo	76
140	36	Jet p_T in unfolding closure test	78
141	37	j_T Response matrices in individual $p_{T\text{jet}}$ bins	78
142	38	Pythia closure test results. Fake tracks include also tracks that do exist in the true dataset, but for one reason or another were not given j_T values. j_T is only calculated for tracks that are associated with jets	79
145	39	Background estimation	81

147	40	Flowchart representation of the perpendicular cone background procedure	81
148	41	j_T background with two different methods	83
149	42	Comparison of the effect of background method on j_T signal.	86
150	43	j_T signal with random bacgkround subtraction fits in different jet p_T bins	86
151	44	Differences between perpendicular cone and random background subtraction in the resulting RMS values.	87
152	45	Resulting signal distributions from SVD unfolding with the perpendicular cone background methods. These are compared to the results from the Bayesian algorithm to estimate the systematic uncertainty.	87
153	46	Differences between Bayesian and SVD unfolding in the resulting RMS values	87
154	47	Unfolding with different number of iterations	88
155	48	Effect of changing prior from true distribution in PYTHIA to the unfolded distribution. Missing figure	88
156	49	Effect of changing minimum jet p_T used in unfolding from 5 to 10 GeV	89
157	50	Relative systematic errors resulting from tracking efficiency uncertainty.	89
158	51	Results from PYTHIA simulations with Cluster energies scaled up and down by 2 %. Additionally jet momenta were scaled by 2 % when determining the jet p_T bin.	90
159	52	Relative systematic errors resulting from cluster energy uncertainty.	91
160	53	Comparison of inclusive j_T distributions between A and C side for minimum bias and EMCAL triggered data.	92
161	54	j_T signal fits in different jet p_T bins	93
162	55	RMS values extracted from the fits for the gaussian (narrow) and inverse gamma (wide) components	94
163	56	RMS values extracted from the fits for the gaussian (narrow) and inverse gamma (wide) components	94
164	57	j_T distributions for high multiplicity p–Pb events. Replace figure	95
165	58	Dihadron j_T results	96

181	59	RMS values of the narrow and wide j_T components in the dihadron correlation analysis. Results from pp collisions at $\sqrt{s} = 7$ TeV (circular symbols) and from p–Pb collisions at $\sqrt{s_{NN}} = 5.02$ TeV (square symbols) are compared to PYTHIA 8 tune 4C simulations at $\sqrt{s} = 7$ TeV (short dashed line) and at $\sqrt{s} = 5.02$ TeV (long dashed line). Different panels correspond to different x_{\parallel} bins with $0.2 < x_{\parallel} < 0.4$ on the left, $0.4 < x_{\parallel} < 0.6$ in the middle, and $0.6 < x_{\parallel} < 1.0$ on the right. The statistical errors are represented by bars and the systematic errors by boxes. [2]	97
190	60	Jet j_T results are compared to results obtained in the dihadron analysis. Dihadron trigger p_T bins are converted to jet p_T bins using observed mean $p_{T,jet}$ values in $p_{T,trigger}$ bins. Dihadron results are for $0.2 < x_{\parallel} < 0.4$	98
194	61	Pythia R parameters j_T	99
195	62	Pythia R parameters RMS	100
196	63	Results of calculating j_T with respect to the jet axis or the leading hadron. The assumption is that because the leading hadron is an imperfect estimate of the jet axis, low j_T tracks should on average be shifted to higher j_T	100

200 1 Introduction

201 REWRITE At sufficiently high energies quarks and gluons are no longer bound to
202 hadrons, but they form a deconfined state known as Quark-Gluon plasma (QGP).
203 The main goal of heavy-ion physics is the study of QGP and its properties. One
204 of the experimental observables that is sensitive to the properties of QGP is the
205 azimuthal distribution of particles in the plane perpendicular to the beam direc-
206 tion.

207 When nuclei collide at non-zero impact parameter (non-central collisions), their
208 overlap region is asymmetric. This initial spatial asymmetry is converted via multi-
209 ple collisions into an anisotropic momentum distribution of the produced particles.
210 For low momentum particles ($p_T \lesssim 3$ GeV/c), this anisotropy is understood to
211 result from hydrodynamically driven flow of the QGP [3–7].

212 One way to characterize this anisotropy is with coefficients from a Fourier se-
213 ries parametrization of the azimuthal angle distribution of emitted hadrons. The
214 second order coefficient, v_2 which is also known as elliptic flow, shows clear depen-
215 dence on centrality. The collision geometry is mainly responsible for the elliptic
216 flow. Higher harmonics don't depend that much on centrality. These higher har-
217 monics carry information about the fluctuations in collisions. The event-by-event
218 fluctuations have an increasing importance in measurements and it has been ob-
219 served that measurements of elliptic flow in central collisions and measurements
220 of higher order harmonics are consistent with the assumption that flow in these
221 cases is mainly due to fluctuations [8].

222 At LHC energies $\sqrt{s_{NN}} = 2.76\text{GeV}$ it has been observed that in general there
223 is little difference to flow at RHIC energies. The v_2 coefficient is about 20% greater
224 at LHC than at RHIC, depending on the centrality bin. The particle identified
225 v_2 for kaons and pions follows the same trend. However it was observed that for
226 proton v_2 the quark number scaling does not work [9]. So far there is no agreement
227 of why this scaling breaks down at LHC or why it works so well at RHIC energies.

228

229 **1.1 Quantum chromodynamics**

230 **1.1.1 Foundation of QCD**

231 There are four known basic interactions in the universe: gravity, electromagnetic,
232 weak and strong interactions. The standard model of particle physics includes
233 three of these, excluding the gravitational interaction. The theory of strong inter-
234 actions is known as Quantum Chromodynamics (QCD).

235 The development of QCD began after the introduction of new powerful particle
236 accelerators that were capable of particle physics research in the 1950s. Before this
237 particles were mainly discovered from cosmic rays. Positrons, neutrons and muons
238 were discovered in the 1930s and charged pions were discovered in 1947 []. The
239 neutral pion was discovered in 1950 [10].

240 The Lawrence Berkeley National Laboratory started the Bevalac accelerator in
241 1954, Super Proton Synchrotron (SPS) in CERN began operating in 1959 and the
242 Alternating Gradient Synchrotron (AGS) at Brookhaven started in 1960. With
243 an energy of 33 GeV AGS was the most powerful accelerator of that time. By
244 the beginning of 1960s several new particles had been discovered. These included
245 antiprotons, antineutrons, Δ -particles and the six hyperons (Ξ^0 , Ξ^- , Σ^\pm , Σ^0 and
246 Λ).

247 Facing this avalanche of new particles, physicists started the search for symme-
248 tries within them. Already in 1932 Heisenberg [11] had proposed an isospin model
249 to explain similarities between the proton and the neutron. In 1962 Gell-Mann
250 and Ne'eman presented that particles sharing the same quantum numbers (spin,
251 parity) could be organised using the symmetry of SU(3). [12] Heisenberg's Isospin
252 model followed the symmetry of SU(2). Using the SU(3) model known baryons
253 and mesons could be presented as octets. This also lead to the discovery of the
254 Ω^- particle since this was missing from the SU(3) decouplet that included heavier
255 baryons.

256 The most simple representation of SU(3) was a triplet. Inside this triplet parti-
257 cles would have electric charges $2/3$ or $-1/3$. However, these had not been detected.
258 In 1964 Gell-Mann [13] and Zweig proposed that baryons and mesons would be
259 bound states of these three hypothetical triplet particles that Gell-Mann called
260 quarks. Now we know that these are the u , d and s quarks. This original quark
261 model without colour was violating the Pauli exclusion principle. For example
262 the Ω^- particle is comprised of three s quarks which would have exactly the same
263 quantum states.

264 The first one to present the idea of colour was Greenberg already in 1964 [14].
265 In 1971 Gell-Mann and Fritsch presented their model, which solved the antisym-
266 metry problem. They added a colour quantum number to quarks, which separated
267 quarks of the same species. In the new colour model the baryonic wave function

268 became

$$(qqq) \rightarrow (q_r q_g q_b - q_g q_r q_b + q_b q_r q_g - q_r q_b q_g + q_g q_b q_r - q_b q_g q_r), \quad (1)$$

269 The colour model was also supported by experimental evidence. The decay
270 rate of a neutral pion with the addition of colours is

$$\Lambda(\pi^0 \rightarrow \gamma\gamma) = \frac{\alpha^2}{2\pi} \frac{N_c^2}{3^2} \frac{m_\pi^3}{f_\pi^2}. \quad (2)$$

271 For $N_c = 3$ this gives 7.75 eV and the measured value is (7.86 ± 0.54) eV [15].

272 Another observable that combines the colour information also to the number
273 of quark flavours is the Drell-Ratio R [16]

$$R = \frac{\sigma(e^+ + e^- \rightarrow \text{hadrons})}{\sigma(e^+ + e^- \rightarrow \mu^+ + \mu^-)} = N_c \sum_f Q_f^2. \quad (3)$$

274 This ratio has the numerical value 2 when including the three light quarks u , d
275 and s . When the collision energy reaches the threshold of heavy quark (c and
276 b) production processes this increases to $^{10}/_3$ (for $f = u, d, s, c$) and $^{11}/_3$ (for $f =$
277 u, d, s, c, b). The energy threshold ($\sqrt{s} \approx 350$ GeV) of $t\bar{t}$ production, has not been
278 reached so far by any e^+e^- colliders.

279 The colour model explained why no free quarks had been observed as only
280 colour neutral states are possible. The simplest ways of producing a colour neu-
281 tral object are the combination of three quarks, and the combination of a quark-
282 antiquark pair. These are known as baryons and mesons.

283 After the addition of colour the main ingredients of QCD had been estab-
284 lished. The final quantum field theory of Quantum Chromodynamics formed
285 quickly between 1972 and 1974. Main part of this was the work by Gross, Wilczek,
286 Politzer and George for non-abelian gauge field theories [17–21]. Gross, Wilczek
287 and Politzer received the Nobel Prize in Physics for their work. The role of gluons
288 as a colour octet was presented by Fritzsch, Gell-Mann and Leutwyler in 1973 [22].
289 The theory had now 8 massless gluons to mediate the strong interaction.

290 However, these gluons had not been discovered. Indirect evidence of the ex-
291 istence had been seen as it was observed that only about half of the momentum
292 of protons was transported by the quarks [23]. Direct evidence should be seen in
293 electron-electron collisions as a third, gluonic, jet in addition to two quark jets.
294 Three jet events were first seen in 1979 at the PETRA accelerator at DESY [24–26].

295 1.1.2 Asymptotic Freedom

296 In Quantum Electrodynamics (QED) the electric charge is screened. In the vicinity
297 of a charge, the vacuum becomes polarized. Virtual charged particle-antiparticle

298 pairs around the charge are arranged so that opposing charges face each other.
299 Since the pairs also include an equal amount opposite charge compared to the
300 original charge the average charge seen by an observer at a distance is smaller.
301 When the distance to the charge increases the effective charge decreases until the
302 coupling constant of QED reaches the fine-structure constant $\alpha = \frac{1}{137}$.

303 Contrary to QED, QCD is a non-abelian theory. In other words the generators
304 of the symmetry group of QCD, SU(3), do not commute. This has the practical
305 consequence that gluons interact also with other gluons, whereas in QED the
306 neutral carrier particles, photons, only interact with charged particles. There
307 is screening also in QCD because of the colour charges, but in addition to that
308 there is antiscreening because of the gluon interactions. In QCD the antiscreening
309 effect dominates over screening. Thus for larger distances to the colour charge
310 the coupling constant is larger. This explains why no free colour charges can be
311 observed. When the distance between charges increases the interaction strengthens
312 until it is strong enough to produce a new quark-antiquark pair.

313 On the other hand, at very small distances the coupling constant approaches
314 0. This is called asymptotic freedom. For large energies and small distances
315 the coupling constant is negligible. In 1975 Collins [27] predicted a state where
316 individual quarks and gluons are no longer confined into bound hadronic states.
317 Instead they form a bulk QCD matter that Edward Shuryak called Quark-Gluon
318 plasma in his 1980 review of QCD and the theory of superdense matter [28]. QGP
319 can be seen as a separate state of matter. A schematic view of a phase diagram
320 for QCD matter is shown in Fig. 1.

321 In the early universe at the age of 10^{-6} s after the Big Bang the conditions
322 preferred the existence of QGP instead of hadronic matter. Nowadays bulk QCD
323 matter, its properties and its phase transitions between hadronic matter and the
324 quark-gluon plasma (QGP) can be explored in the laboratory, through collisions
325 of heavy atomic nuclei at ultra-relativistic energies. The study of QCD matter at
326 high temperature is of fundamental and broad interest. The phase transition in
327 QCD is the only phase transition in a quantum field theory that can be probed by
328 any present or foreseeable technology.

329 One important property of the QGP is the shear viscosity to entropy ratio,
330 η/s . It is believed that this ratio has an universal minimum value of $1/4\pi \approx 0.08$,
331 among all substances in nature. This limit would be reached in the strong coupling
332 limit of certain gauge theories [30]. The temperature dependance of the ratio is
333 shown in Fig. 2. The minimum value of η/s is found in the vicinity of the critical
334 temperature, T_c [31]. Finding the η/s values in QGP matter would therefore also
335 provide a way of determining the critical point of QCD matter.

336 The η/s value for the matter created in Au-Au collisions at RHIC ($\sqrt{s_{NN}}$) has
337 been estimated to be 0.09 ± 0.015 [31], which is very close to the lowest value for a

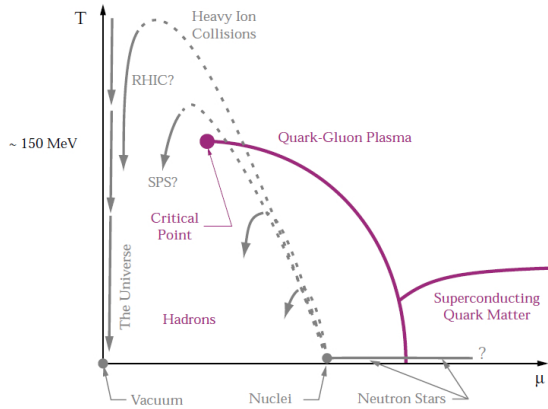


Figure 1: A schematic outline for the phase diagram of QCD matter at ultra-high density and temperature. The quark chemical potential μ that is on the x-axis represents the imbalance between quarks and antiquarks. At zero temperature this corresponds to the number of quarks but at higher temperatures there are also additional pairs of quarks and antiquarks. Along the horizontal axis the temperature is zero, and the density is zero up to the onset transition where it jumps to nuclear density, and then rises with increasing μ . Neutron stars are in this region of the phase diagram, although it is not known whether their cores are dense enough to reach the quark matter phase. Along the vertical axis the temperature rises, taking us through the crossover from a hadronic gas to the quark-gluon plasma. This is the regime explored by high-energy heavy-ion colliders. [29]

wide class of thermal quantum field theories [30] for all relativistic quantum field theories at finite temperature and zero chemical potential. This suggests that the matter created goes through a phase where it is close to the critical point of QCD.
 338
 339
 340
 341

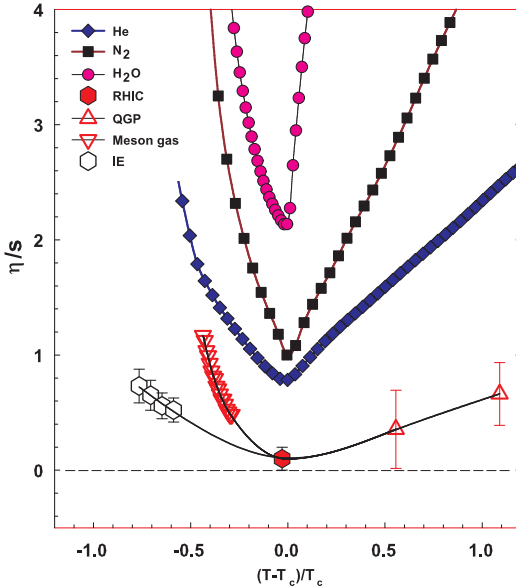


Figure 2: η/s as a function of $(T - T_c)/T_c$ for several substances as indicated. The calculated values for the meson-gas have an associated error of $\sim 50\%$. The lattice QCD value $T_c = 170$ MeV is assumed for nuclear matter. The lines are drawn to guide the eye. [31]

342 1.2 heavy-ion physics

343 The Quark Gluon Plasma (QGP) is experimentally accessible by colliding heavy-
344 ions at high energies. Nowadays research of Heavy-Ion Collisions is mainly per-
345 formed at two particle colliders; The Relativistic heavy-ion Collider (RHIC) at
346 BNL in New York, USA and the Large Hadron Collider (LHC) at CERN in Switzer-
347 land. Energy densities at these colliders should be enough to produce QGP and
348 convincing evidence of the creation has been seen at both colliders.

349 The development of heavy-ion physics is strongly connected to the development
350 of particle colliders. Experimental study of relativistic heavy-ion collisions has been
351 carried out for three decades, beginning with the Bevalac at Lawrence Berkeley
352 National Laboratory (LBNL) [32], and continuing with the AGS at Brookhaven
353 National Laboratory (BNL) [33], CERN SPS [34], RHIC at BNL and LHC at
354 CERN.

355 1.2.1 History

356 The first heavy-ion collisions were performed at the Bevalac experiment at the
357 Lawrence Berkeley National Laboratory [32] and at the Joint Institute for Nu-
358 clear Research in Dubna [35] at energies up to 1GeV per nucleon. In 1986 the
359 Super Proton Synchrotron (SPS) at CERN started to look for QGP signatures in
360 O+Pb collisions. The center-of-mass energy per colliding nucleon pair ($\sqrt{s_{NN}}$)
361 was 19.4 GeV [34]. These experiments did not find any decisive evidence of the
362 existence of QGP. In 1994 a heavier lead (Pb) beam was introduced for new experi-
363 ments at $\sqrt{s_{NN}} \approx 17$ GeV. At the same time the Alternating Gradient Synchrotron
364 (AGS) at BNL, Brookhaven collided ions up to ^{32}S with a fixed target at energies
365 up to 28 GeV [33]. Although the discovery of a new state of matter was reported
366 at CERN, these experiments provided no conclusive evidence of QGP. Now SPS
367 is used with 400 GeV proton beams for fixed-target experiments, such as the SPS
368 heavy-ion and Neutrino Experiment (SHINE) [36], which tries to search for the
369 critical point of strongly interacting matter.

370 The Relativistic heavy-ion Collider (RHIC) at BNL in New York, USA started
371 its operation in 2000. The top center-of-mass energy per nucleon pair at RHIC, 200
372 GeV, was reached in the following years. The results from the experiments at RHIC
373 have provided a lot of convincing evidences that QGP was created [3,4,37,38]. The
374 newest addition to the group of accelerators capable of heavy-ion physics is the
375 Large Hadron Collider (LHC) at CERN, Switzerland. LHC started operating in
376 November 2009 with proton-proton collisions. First Pb-Pb heavy-ion runs started
377 in November 2010 with $\sqrt{s_{NN}} = 2.76$ TeV, over ten times higher than at RHIC.
378 Among the six experiments at LHC, the Large Ion Collider Experiment (ALICE)
379 is dedicated to heavy-ion physics. Also CMS and ATLAS have active heavy-ion

`380` programs.

Table 1: Summary of datasets

Run 1 (2009-2013)			Run 2 (2015-2018)		
pp	0.9 TeV	$\sim 200 \mu\text{b}^{-1}$	pp	5.02 TeV	$\sim 1.3 \text{ pb}^{-1}$
	2.76 TeV	$\sim 100 \text{ nb}^{-1}$		13.0 TeV	$\sim 25 \text{ pb}^{-1}$
	7.0 TeV	$\sim 1.5 \text{ pb}^{-1}$	p-Pb	5.02 TeV	$\sim 3 \text{ nb}^{-1}$
	8.0 TeV	$\sim 2.5 \text{ pb}^{-1}$		8.16 TeV	$\sim 25 \text{ nb}^{-1}$
p-Pb	5.02 TeV	$\sim 15 \text{ nb}^{-1}$	XeXe	5.44 TeV	$\sim 0.3 \mu\text{b}^{-1}$
Pb-Pb	2.76 TeV	$\sim 75 \mu\text{b}^{-1}$	Pb-Pb	5.02 TeV	$\sim 1 \text{ nb}^{-1}$

381 1.3 Features of Heavy-Ion Collisions

382 1.3.1 Collision Geometry

383 In contrast to protons atomic nuclei are objects with considerable transverse size.
 384 The properties of a heavy-ion collision depend strongly on the impact parameter
 385 b which is the vector connecting the centers of the two colliding nuclei at their
 386 closest approach. One illustration of a heavy-ion collision is shown in Fig. 3.

387 Impact parameter defines the reaction plane which is the plane spanned by b
 388 and the beam direction. Ψ_{RP} gives the angle between the reaction plane and some
 389 reference frame angle. Experimentally the reference frame is fixed by the detector
 390 setup. Reaction plane angle cannot be directly measured in high energy nuclear
 collisions, but it can be estimated with the event plane method [39].

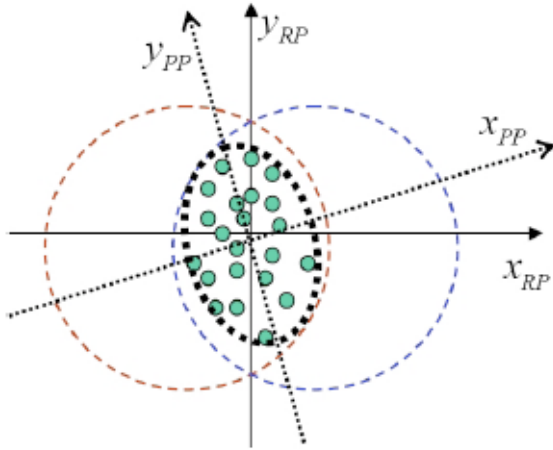


Figure 3: The definitions of the Reaction Plane and Participant Plane coordinate systems [40]. The dashed circles represent the two colliding nuclei and the green dots are partons that take part in the collision. x_{PP} and x_{RP} are the participant and reaction planes. The angle between x_{RP} and x_{PP} is given by Eq. (4). y_{PP} and y_{RP} are lines perpendicular to the participant and reaction planes.

391
 392 Participant zone is the area containing the participants. The distribution of
 393 nucleons in the nucleus exhibits time-dependent fluctuations. Because the nucleon
 394 distribution at the time of the collision defines the participant zone, the axis of
 395 the participant zone fluctuates and can deviate from the reaction plane. The angle
 396 between the participant plane and the reaction plane is defined by [41]

$$\psi_{PP} = \arctan \frac{-2\sigma_{xy}}{\sigma_y^2 - \sigma_x^2 + \sqrt{(\sigma_y^2 - \sigma_x^2)^2 + 4\sigma_{xy}^2}}, \quad (4)$$

397 where the σ -terms are averaged over the energy density.

$$\sigma_y^2 = \langle y^2 \rangle - \langle y \rangle^2, \sigma_x^2 = \langle x^2 \rangle - \langle x \rangle^2, \sigma_{xy} = \langle xy \rangle - \langle x \rangle \langle y \rangle \quad (5)$$

398 The impact parameter is one way to quantize the centrality of a heavy-ion
399 collision but it is impossible to measure in a collision. It can be estimated from
400 observed data using theoretical models, but this is always model-dependent and
401 to compare results from different experiments one needs an universal definition for
402 centrality. The difference between central and peripheral collisions is illustrated
403 in Fig. 4. In a central collision the overlap region is larger than in a peripheral
404 collision. Larger overlap region translates into a larger number of nucleons partici-
405 pating in the collision, which in turn leads to a larger number of particles produced
406 in the event.

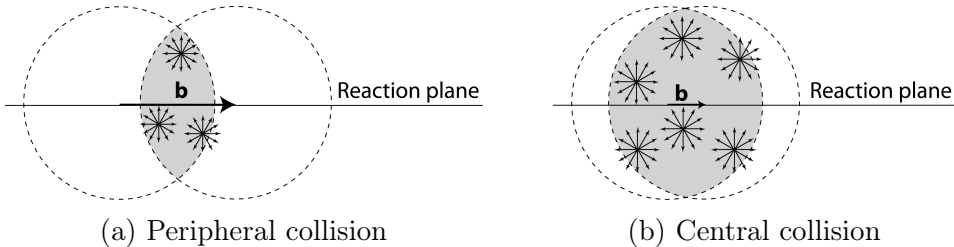


Figure 4: Interaction between partons in central and peripheral collisions. The snowflakes represent elementary parton-parton collisions. When the impact parameter b is large the number of elementary collisions is small. Particle production is small. Smaller impact parameter increases the number of elementary collisions. This increases particle production.

407 Usually centrality is defined by dividing collision events into percentile bins by
408 the number participants or experimentally by the observed multiplicity. Centrality
409 bin 0-5% corresponds to the most central collisions with the highest multiplicity
410 and higher centrality percentages correspond to more peripheral collisions with
411 lower multiplicities. A multiplicity distribution from ALICE measurements [42]
412 illustrating the centrality division is shown in Fig. 5. The distribution is fitted
413 using a phenomenological approach based on a Glauber Monte Carlo [43] plus a
414 convolution of a model for the particle production and a negative binomial distri-
415 bution.

416 1.3.2 Nuclear Geometry

417 To model heavy-ion collisions one must first have a description as good as possible
418 of the colliding objects. Atomic nuclei are complex ensembles of nucleons. The
419 nuclei used in heavy-ion physics have in the order of 200 nucleons. Mostly used

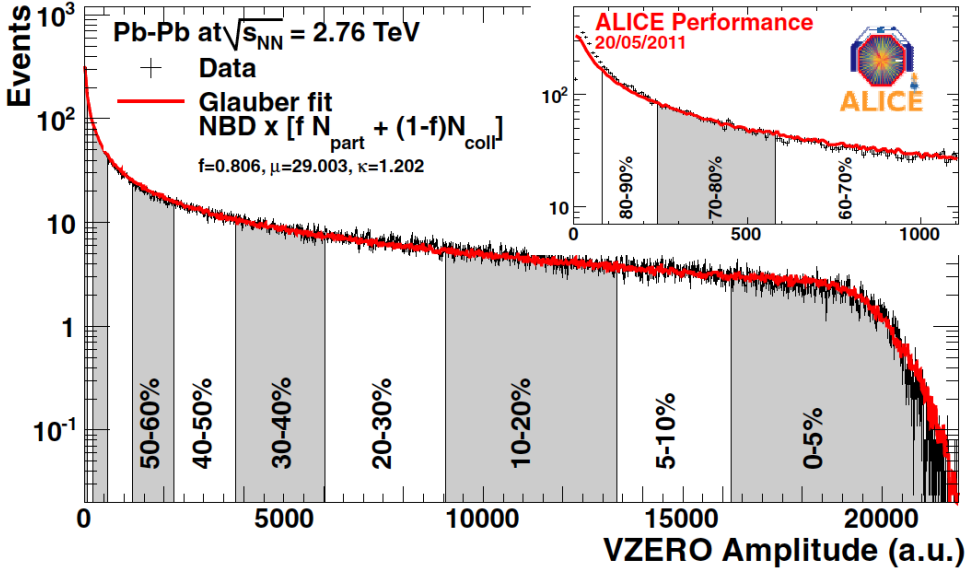


Figure 5: An illustration of the multiplicity distribution in ALICE measurements. The red line shows the fit of the Glauber calculation to the measurement. The data is divided into centrality bins [42]. The size of the bins corresponds to the indicated percentile.

⁴²⁰ nuclei are ²⁰⁸Pb at LHC and ¹⁹⁷Au at RHIC. The distribution of these nucleons
⁴²¹ within a nucleus is not uniform and is subject to fluctuations in time.

⁴²² Nuclear geometry in heavy-ion collisions is often modelled with the Glauber
⁴²³ Model. The model was originally developed to address the problem of high energy
⁴²⁴ scattering with composite particles. Glauber presented his first collection of papers
⁴²⁵ and unpublished work in his 1958 lectures [44]. In the 1970's Glauber's work
⁴²⁶ started to have utility in describing total cross sections. Maximon and Czyz applied
⁴²⁷ it to proton-nucleus and nucleus-nucleus collisions in 1969 [45].

⁴²⁸ In 1976 [46] Białas, Bleszyński, and Czyz applied Glauber's approach to
⁴²⁹ inelastic nuclear collisions. Their approach introduced the basic functions used in
⁴³⁰ modern language including the thickness function and the nuclear overlap function.
⁴³¹ Thickness function is the integral of the nuclear density over a line going through
⁴³² the nucleus with minimum distance s from its center

$$T_A(s) = \int_{-\infty}^{\infty} dz \rho(\sqrt{s^2 + z^2}). \quad (6)$$

⁴³³ This function gives the thickness of the nucleus, i.e. the amount material seen by
⁴³⁴ a particle passing through it.

⁴³⁵ Overlap function is an integral of the thickness functions of two colliding nuclei
⁴³⁶ over the overlap area. This can be seen as the material that takes part in the
⁴³⁷ collision. It is given as a function of the impact parameter b

$$T_{AB}(b) = \int ds^2 T_A(\bar{s}) T_B(\bar{s} - \bar{b}) \quad (7)$$

⁴³⁸ The average overlap function, $\langle T_{AA} \rangle$, in an A-A collisions is given by [47]

$$\langle T_{AA} \rangle = \frac{\int T_{AA}(b) db}{\int (1 - e^{-\sigma_{pp}^{inel} T_{AA}(b)}) db}. \quad (8)$$

⁴³⁹ Using $\langle T_{AA} \rangle$ one can calculate the mean number of binary collisions

$$\langle N_{coll} \rangle = \sigma_{pp}^{inel} \langle T_{AA} \rangle, \quad (9)$$

⁴⁴⁰ where the total inelastic cross-section, σ_{pp}^{inel} , gives the probability of two nucleons
⁴⁴¹ interacting. The number of binary collisions is related to the hard processes in a
⁴⁴² heavy-ion collision. Each binary collision has equal probability for direct produc-
⁴⁴³ tion of high-momentum partons. Thus the number of high momentum particles is
⁴⁴⁴ proportional to $\langle N_{coll} \rangle$.

⁴⁴⁵ Soft production on the other hand is related to the number of participants.
⁴⁴⁶ It is assumed that in the binary interactions participants get excited and further
⁴⁴⁷ interactions are not affected by previous interactions because the time scales are
⁴⁴⁸ too short for any reaction to happen in the nucleons. After the interactions ex-
⁴⁴⁹ cited nucleons are transformed into soft particle production. Production does not
⁴⁵⁰ depend on the number of interactions a nucleon has gone through. The average
⁴⁵¹ number of participants, $\langle N_{part} \rangle$ can also be calculated from the Glauber model

$$\begin{aligned} \langle N_{part}^{AB}(b) \rangle &= \int ds^2 T_A(\bar{s}) \left[1 - \left[1 - \sigma_{NN} \frac{T_B(\bar{s} - \bar{b})}{B} \right]^B \right] \\ &+ \int ds^2 T_B(\bar{s}) \left[1 - \left[1 - \sigma_{NN} \frac{T_A(\bar{s} - \bar{b})}{A} \right]^A \right]. \end{aligned} \quad (10)$$

⁴⁵² Glauber calculations require some knowledge of the properties of the nuclei.
⁴⁵³ One requirement is the nucleon density distribution, which can be experimen-
⁴⁵⁴ tally determined by studying the nuclear charge distribution in low-energy elec-
⁴⁵⁵ tron scattering experiments [43]. The nucleon density is usually parametrized by
⁴⁵⁶ a Woods-Saxon distribution

$$\rho(r) = \frac{\rho_0}{1 + \exp\left(\frac{r-R}{a}\right)}, \quad (11)$$

457 where ρ_0 is the nucleon density in center of the nucleus, R is the nuclear radius
 458 and a parametrizes the depth of the skin. The density stays relatively constant as
 459 a function of r until around R where it drops to almost 0 within a distance given
 460 by a .

461 Another observable required in the calculations is the total inelastic nucleon-
 462 nucleon cross-section $\sigma_{\text{inel}}^{\text{NN}}$. This can be measured in proton-proton collisions at
 463 different energies.

464 There are two often used approaches to Glauber calculations. The optical ap-
 465 proximation is one way to get simple analytical expressions for the nucleus-nucleus
 466 interaction cross-section, the number of interacting nucleons and the number of
 467 nucleon-nucleon collisions. In the optical Glauber it is assumed that during the
 468 crossing of the nuclei the nucleons move independently and they will be essentially
 469 undeflected.

470 With the increase of computational power at hand the Glauber Monte Carlo
 471 (GMC) approach has emerged as a method to get a more realistic description of
 472 the collisions. In GMC the nucleons are distributed randomly in three-dimensional
 473 coordinate system according to the nuclear density distributions. Also nuclear
 474 parameters, like the radius R can be sampled from a distribution. A heavy-ion
 475 collision is then treated as a series of independent nucleon-nucleon collisions, where
 476 in the simplest model nucleons interact if their distance in the plane orthogonal
 477 to the beam axis, d , satisfies

$$d < \sqrt{\sigma_{\text{inel}}^{\text{NN}}} \quad (12)$$

478 The average number of participants and binary collisions can then be determined
 479 by simulating many nucleus-nucleus collisions. The results of one GMC Pb-Pb
 480 event with impact parameter $b = 9.8$ fm is shown in Fig. 6

481 1.3.3 Hydrodynamical Modelling

482 The relativistic version of hydrodynamics has been used to model the deconfined
 483 phase of a heavy-ion collision with success. Heavy-ion collisions produce many
 484 hadrons going into all directions. It is expected that tools from statistical physics
 485 would be applicable to this complexity [48]. The power of relativistic hydrodynam-
 486 ics lies in its simplicity and generality. Hydrodynamics only requires that there is
 487 local thermal equilibrium in the system. In order to reach thermal equilibrium the
 488 system must be strongly coupled so that the mean free path is shorter than the
 489 length scales of interest [49].

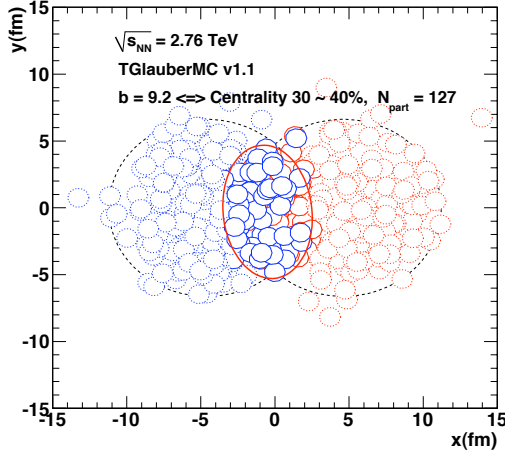


Figure 6: The results of one Glauber Monte Carlo simulation. Big circles with black dotted boundaries represent the two colliding nuclei. The participant zone is highlighted with the solid red line. Small red and blue circles represent nucleons. Circles with thick boundaries are participants i.e. they interact with at least one nucleon from the other nucleus. Small circles with dotted boundaries are spectators which do not take part in the collision.

490 The use of relativistic hydrodynamics in high-energy physics dates back to
 491 Landau [50] and the 1950's, before QCD was discovered. Back then it was used
 492 in proton-proton collisions. Development of hydrodynamics for the use of heavy-
 493 ion physics has been active since the 1980's, including Bjorken's study of boost-
 494 invariant longitudinal expansion and infinite transverse flow [51]. Major steps
 495 were taken later with the inclusion of finite size and and dynamically generated
 496 transverse size [52, 53], a part of which was done at the University of Jyväskylä.
 497 The role of hydrodynamics in heavy-ion physics was strengthened when QGP was
 498 observed to behave like a liquid by RHIC [3].

499 The evolution of a heavy-ion event can be divided into four stages. A schematic
 500 representation of the evolution of the collisions is shown in Fig. 7. Stage 1 follows
 501 immediately the collision. This is known as the pre-equilibrium stage. Hydrody-
 502 namic description is not applicable to this regime because thermal equilibrium is
 503 not yet reached. The length of this stage is not known but it is assumed to last
 504 about $1 \text{ fm}/c$ in proper time τ .

505 The second stage is the regime where thermal equilibrium or at least near-
 506 equilibrium is reached. In this stage hydrodynamics should be applicable if the
 507 temperature is above the deconfinement temperature [49]. This lasts about $5 - 10 \text{ fm}/c$
 508 until the temperature of the system sinks low enough for hadronization to

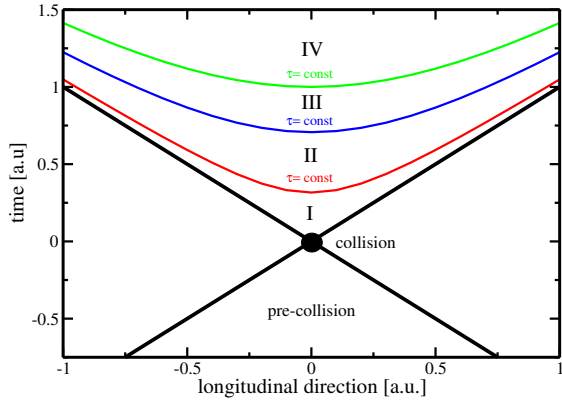


Figure 7: Schematic representation [49] of a heavy-ion collision as the function of time and longitudinal coordinates z . The various stages of the evolution correspond to proper time $\tau = \sqrt{t^2 - z^2}$ which is shown as hyperbolic curves separating the different stages.

509 occur. Now the system loses its deconfined, strongly coupled, state and hydrodynamics
 510 can no longer be used. The third stage is the hadron gas stage where the
 511 hadrons still interact. This ends when hadron scattering becomes rare and they
 512 no longer interact. In the final stage hadrons are free streaming and they fly in
 513 straight lines until they reach the detector.

514 The hydrodynamical approach treats the ensemble of particles as a fluid. It
 515 uses basic equations from hydrodynamics and thermodynamics but with a few
 516 modifications to account for the relativistic energies. The calculation is based
 517 on a collection of differential equations connecting the local thermal variables like
 518 temperature, pressure etc. to local velocities of the fluid. One also needs equations
 519 of state that connect the properties of the matter, e.g. temperature and pressure
 520 to density. Given initial conditions and equations of state the calculation gives the
 521 time-evolution of the system.

522 At first only ideal hydrodynamics was used. Ideal hydrodynamics does not
 523 include viscosity but it is a relatively good approximation and it could predict
 524 phenomena like elliptic flow. For more detailed calculations also viscosity must be
 525 considered and viscosity itself is an interesting property of QGP.

526 1.4 Flow

527 In a heavy-ion collision the bulk particle production is known as flow. The pro-
 528 duction is mainly isotropic but a lot of studies including my thesis focus on the
 529 small anisotropies. After the formation of the QGP, the matter begins to expand
 530 as it is driven outwards by the strong pressure difference between the center of the
 531 collision zone and the vacuum outside the collision volume. The pressure-driven
 532 expansion is transformed into flow of low-momentum particles in the hadroniza-
 533 tion phase. Since the expansion is mainly isotropic the resulting particle flow is
 534 isotropic with small anisotropic corrections that are of the order of 10% at most.
 535 The isotropic part of flow is referred to as radial flow.

536 The transverse momentum spectra dN/dp_T in heavy-ion collisions is shown

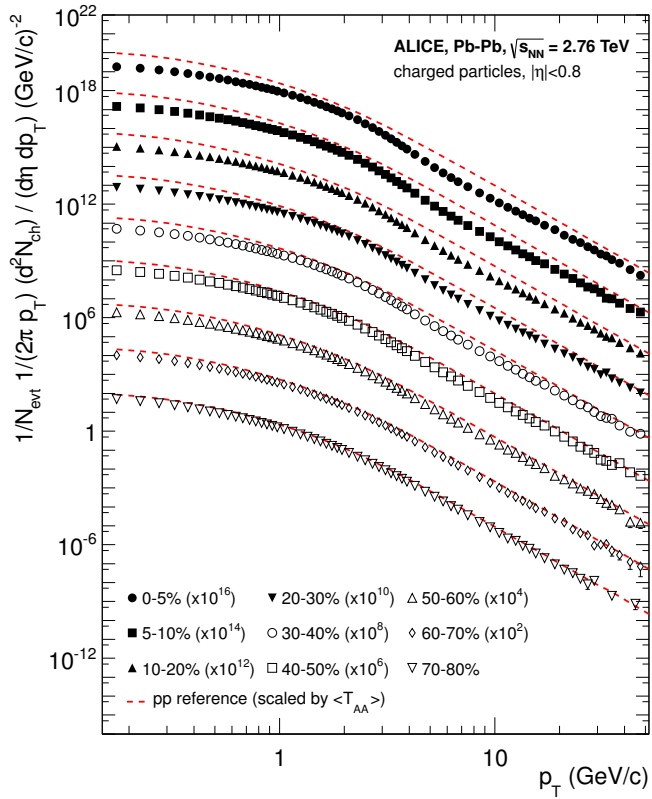


Figure 8: Charged particle spectra measured by ALICE [54] for the 9 centrality classes given in the legend. The distributions are offset by arbitrary factors given in the legend for clarity. The distributions are offset by arbitrary factors given in the legend for clarity. The dashed lines show the proton-proton reference spectra scaled by the nuclear overlap function determined for each centrality class and by the Pb-Pb spectra scaling factors [54].

537 in Fig. 8. The vast majority of produced particles have small p_T . The difference
 538 between the yield of 1 GeV/c and 4 GeV/c particles is already 2-3 orders of mag-
 539 nitude. Any observables that are integrated over p_T are therefore dominated by
 540 the small momentum particles.

541 1.4.1 Anisotropic Flow

542 In a non-central heavy-ion collision the shape of the impact zone is almond-like.
 543 In peripheral collisions the impact parameter is large which means a strongly
 544 asymmetric overlap region. In a central collision the overlap region is almost
 545 symmetric in the transverse plane. In this case the impact parameter is small.
 546 Collisions with different impact parameters are shown in Fig. 4.

547 The pressure gradient is largest in-plane, in the direction of the impact pa-
 548 rameter b , where the distance from high pressure, at the collision center, to low
 549 pressure, outside the overlap zone, is smallest. This leads to stronger collective
 550 flow into in-plane direction, which in turn results in enhanced thermal emission
 551 through a larger effective temperature into this direction, as compared to out-of-
 552 plane [5, 6, 55]. The resulting flow is illustrated in Fig. 9. Flow with two maxima
 553 in the direction of the reaction plane is called elliptic flow. This is the dominant

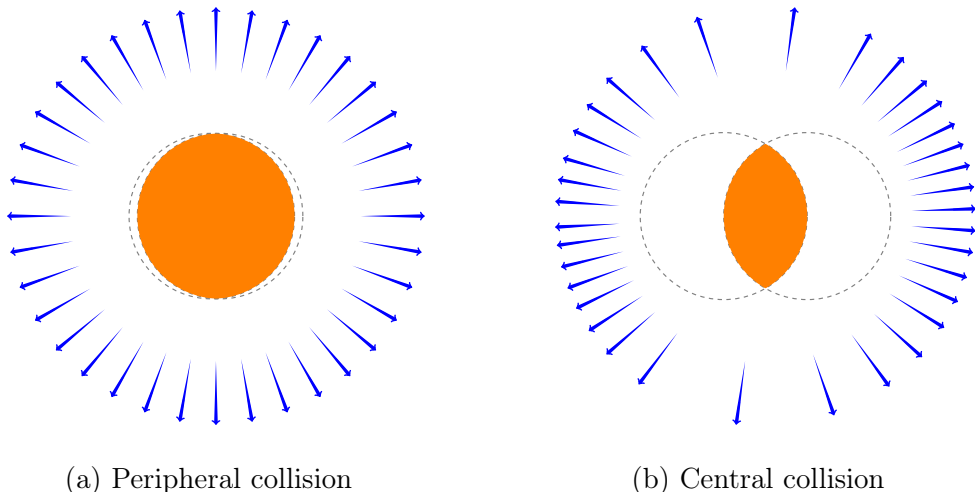


Figure 9: Illustration of flow in momentum space in central and peripheral collisions. The density of the arrows represent the magnitude of flow seen at a large distance from the collision in the corresponding azimuthal direction. In a peripheral collision momentum flow into in-plane direction is strong and flow into out-of-plane direction is weak. In a central collision anisotropy in flow is smaller, but the total yield of particles is larger.

554 part of anisotropic flow. Also more complex flow patterns can be identified. The
555 most notable of these is the triangular flow, which is mainly due to fluctuations in
556 the initial conditions.

557 Flow is nowadays usually quantified in the form of a Fourier composition

$$E \frac{d^3N}{dp^3} = \frac{1}{2\pi p_T} \frac{d^2N}{dp_T d\eta} \left(1 + \sum_{n=1}^{\infty} 2v_n(p_T, \eta) \cos(n(\phi - \Psi_n)) \right), \quad (13)$$

558 where the coefficients v_n give the relative strengths of different anisotropic flow
559 components and the overall normalisation gives the strength of radial flow. Elliptic
560 flow is represented by v_2 and v_3 represents triangular flow. The first coefficient,
561 v_1 , is connected to directed flow. This will however in total be zero because of
562 momentum conservation. It can be nonzero in some rapidity or momentum regions
563 but it must be canceled by other regions.

564 The first approaches to quantifying the anisotropy of flow did not use the
565 Fourier composition. Instead they approached the problem with a classic event
566 shape analysis using directivity [56] or sphericity [5, 57] to quantify the flow.

567 The first experimental studies of anisotropy were performed at the AGS [58]
568 in 1993. They noted that the anisotropy of particle production in one region
569 correlates with the reaction plane angle defined in another region.

570 The first ones to present the Fourier decomposition were Voloshin and Zhang in
571 1996 [59]. This new approach was useful for detecting different types of anisotropy
572 in flow, since the different Fourier coefficients give different harmonics in flow.
573 They also show the relative magnitude of each harmonic compared to radial flow.

574 Some parts of the Fourier composition approach were used for Au-Au collisions
575 at $\sqrt{s_{NN}} = 11.4\text{GeV}$ at AGS in 1994 [60]. This analysis still focused on event
576 shapes but they constructed these shapes using Fourier composition from different
577 rapidity windows.

578 Add a paragraph on the lessons learned from flow studies.

579 1.5 Hard processes

580 1.5.1 pQCD factorization

581 The term Hard Scattering is used in connection with the scattering of two point-
582 like constituents (partons) of colliding nucleons, when the momentum transfer Q^2
583 is large ($Q \gg \Lambda_{\text{QCD}}$). Figure 11 shows the incoming partons, quarks or gluons, as
584 they exchange a space-like virtual gluon and produce two highly virtual outgoing
585 partons. The outgoing partons will eventually fragment into collimated showers of
586 partons, referred to as jets

587 Jet fragmentation can be factorised into three components; the parton distribu-
588 tion functions f_a, f_b that give the probability of getting a parton with momentum

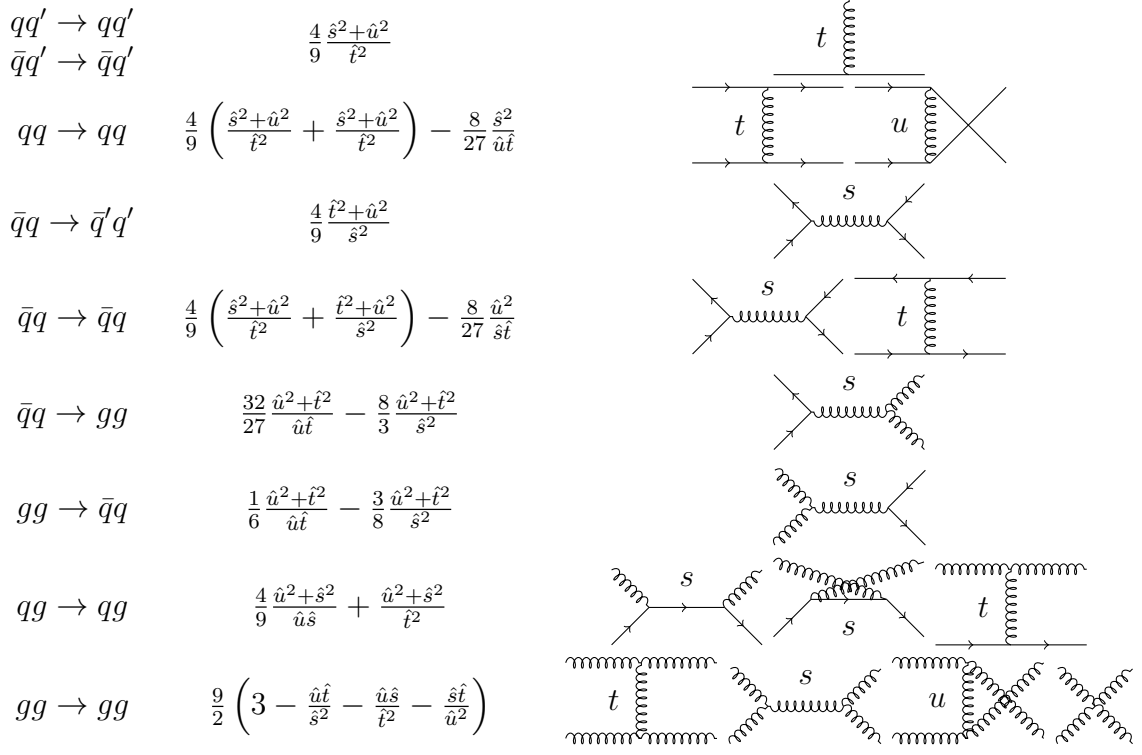


Figure 10: The basic pQCD processes and their quadratic matrix elements

fraction x of the proton, the cross section of the elementary scattering $ab \rightarrow cd$ (Fig. 10) and the fragmentation functions that give the probability of getting hadron h from the parton.

$$\frac{d\sigma_{pp}^h}{dy d^2 p_T} = K \sum_{abcd} \int dx_a dx_b f_a(x_a, Q^2) f_b(x_b, Q^2) \frac{d\sigma}{dt} (ab \rightarrow cd) \frac{D_{h/c}^0}{\pi z_c}, \quad (14)$$

where

$$x_{a,b} = \frac{|p_{a,b}|}{|p_{proton}|}.$$

Parton Distribution Function

Parton Distribution Functions (PDFs) are essential to calculate the scattering cross section. They are extracted from comprehensive global analysis of experimental results from a variety of fixed-target and collider experiments. PDFs $f_a(x)$ give the

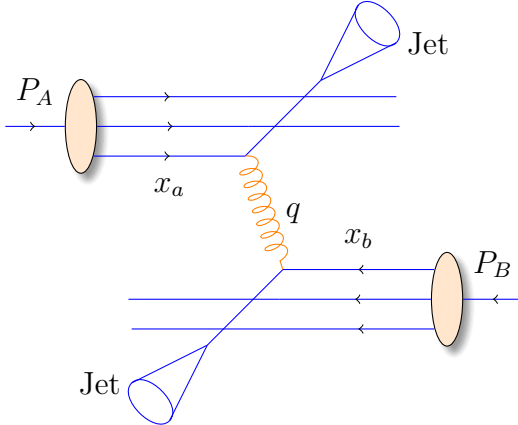


Figure 11: Schematic view of hard scattering process of $p + p \rightarrow 2 \text{ jets}$

597 differential probability for parton a to carry momentum fraction x of the proton
598 momentum.

599 As the PDFs cannot be calculated from first principles. In practice the PDFs
600 are measured in Deeply Inelastic Scattering (DIS) experiments and are extrapolated
601 to the relevant momentum scales at LHC using the Dokshitzer-Gribov-Lipatov-
602 Altarelli-Parisi (DGLAP) evolution scheme [61–63]

$$\mu_F^2 \frac{\partial f_i(x, \mu_F^2)}{\partial \mu_F^2} = \sum_j \frac{\alpha_s(\mu_F)}{2\pi i} \int_x^1 \frac{dz}{z} P_{ij}(z) f_j\left(\frac{x}{z}, \mu_F^2\right), \quad (15)$$

603 where μ_F is a factorization scale. The splitting functions P_{ij} describe a probability
604 to radiate parton i from parton j as a function of the momentum fraction z carried
605 away by the offspring parton.

606 Fragmentation functions

607 The final component in the factorization, fragmentation functions, describe the
608 distribution of the fractional momenta of particles radiated from the outgoing
609 parton. Fragmentation function are given with respect to the momentum fraction
610 z which is defined as the longitudinal momentum fraction of jet momentum p_{jet}
611 carried away by the jet fragment p_{part}

$$z = \frac{\bar{p}_{\text{part}} \cdot \bar{p}_{\text{jet}}}{p_{\text{jet}}^2} = \frac{p_{\text{part}}}{p_{\text{jet}}} \Big|_{\bar{p}_{\text{part}} \times \bar{p}_{\text{jet}} = 0} \quad (16)$$

612 Fragmentation function $D(z)$ then gives the average multiplicity m of jet frag-
613 ments having $z > z_0$ [1].

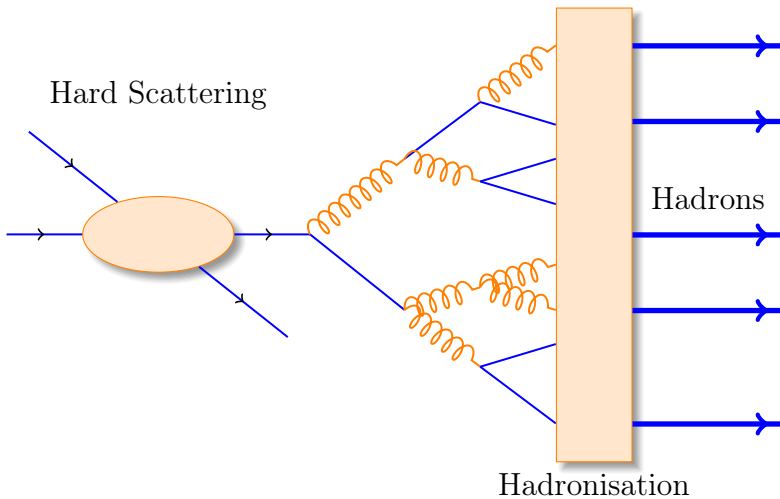


Figure 12: An illustration of jet showering. The highly virtual parton from the hard scattering will produce a shower of softer partons. When the virtuality is low enough the shower will go through a hadronisation process that produces the hadrons, which will be eventually observed in the detector.

$$m(z_0) = \int_{z_0}^1 D(z) dz \Rightarrow m(0) \equiv \langle m \rangle = \int_0^1 D(z) dz \quad (17)$$

614 Because of momentum conservation the sum of all jet fragments must be equal
615 to the jet momentum, i.e.

$$\sum p_{i,\text{part}} = p_{\text{jet}} \Rightarrow \sum z_i = 1 \Rightarrow \int_0^1 z D(z) dz = 1 \quad (18)$$

616 A natural consequence is that the average momentum fraction is the inverse of
617 the average multiplicity

$$\langle z \rangle = \frac{\int_0^1 z D(z) dz}{\int_0^1 D(z) dz} = \frac{1}{\langle m \rangle}. \quad (19)$$

618 1.5.2 Jet hadronisation

619 When the parton shower reaches a scale close to Λ_{QCD} , the perturbative descrip-
620 tion is no longer valid. Thus the hadronisation stage must be described in a
621 non-perturbative manner. One simple scenario that is used in several theory calcu-
622 lations is the so-called local parton-hadron duality [64]. In the local parton-hadron
623 duality hypothesis it is assumed that there exists a low virtuality scale Q_0 in which

the hadronisation happens, that is independent of the scale of the primary hard process. At this scale the partons are transformed into hadrons, assuming that the flow of momentum and quantum numbers for the hadrons can be directly obtained from those of partons introducing only small normalising constants.

628 Lund string model

One common implementation in MC generators is the Lund string fragmentation algorithm [65]. The string model is based on the fact that in QCD linear confinement is expected over large distances [66]. This can be modelled by imagining a colour flux tube being stretched between the outgoing partons. The left side of Fig. 13 illustrates this point for a $q\bar{q}$ -pair. The tube is assumed to have a uniform fixed transverse size of about 1 fm along its length, which leads to a linearly rising potential $V(r) = \kappa r$, where the string constant κ describes the amount of energy per unit length. A value of $\kappa \approx 1 \text{ GeV/fm} \approx 0.2 \text{ GeV}^2$ can be obtained from hadron mass spectroscopy.

The evolution of string fragmentation is illustrated schematically on the right side of Fig. 13. This figure is drawn in a light cone presentation, so the initial quark and antiquark are going to separate directions at the speed of light, which assumes them as massless. The string between them, illustrated in the figure by the red line, stretches until its potential energy becomes high enough that it can break, forming a new quark-antiquark pair. If the original pair was $q\bar{q}$ and the new pair $q'\bar{q}'$, now two new pairs $q\bar{q}'$ and $q'\bar{q}$ have formed. As these particles are also moving away from each other, the strings between them can stretch and break, creating yet more pairs. The process continues until the invariant mass of the system connected by the string becomes small enough and a final state meson is formed.

To mathematically model the string one can use a massless relativistic string with no transverse degrees of freedom. The gluons are represented as energy and momentum carrying kinks on the string with incoherent sums of one colour charge and one anticolour charge. When this string breaks, it is classically required that the created quark and antiquark are produced at a certain distance if they are to have any mass or transverse momentum. However, taking into account quantum mechanics, the pair must be created at one point and then tunnel out to the classically allowed region. Thus the probability to create a new quark-antiquark pair becomes proportional to the tunnelling probability [65].

$$P_{\text{tunnelling}} \propto \exp\left(\frac{-\pi m_\perp^2}{\kappa}\right) = \exp\left(\frac{-\pi m^2}{\kappa}\right)\left(\frac{-\pi p_\perp^2}{\kappa}\right), \quad (20)$$

where the transverse mass m_\perp is defined as $m_\perp^2 = m^2 + p_\perp^2$. The transverse momentum is now defined to be transverse to the string axis. This formula gives

660 flavour-independent Gaussian p_\perp -distribution for the created $q\bar{q}$ pairs.

661 As explained above the string fragmentation would only produce mesons in
662 the final state, but we know that also baryons are created in the process. In the
663 string fragmentation model baryon production is included by adding a probability
664 that a diquark-antidiquark pair is created instead of a quark-antiquark pair when
665 a string breaks.

666 The kinematics of each string breaking are determined iteratively. Since there
667 is no natural ordering, the string breaking can be considered in any order and
668 the answer obtained must be the same. One can start from the q leg and work
669 one's way to the \bar{q} leg, or vice versa. This give a left-right symmetry of the
670 string fragmentation. In the Lund model this is taken into account by defining a
671 symmetric fragmentation function

$$f(z) \propto \frac{1}{z} (1-z)^a \exp\left(-\frac{bm_\perp^2}{z}\right) \quad (21)$$

672 to break the string into a hadron and a remainder system. Here z is the fraction
673 of light-cone momentum p^+ given to the hadron in the string breaking, m_\perp is the
674 transverse mass of the hadron and a and b are tunable parameters of the model.

675 For heavy quarks this has to be modified as

$$f(z) \propto \frac{1}{z^{1+bm_Q^2}} (1-z)^a \exp\left(-\frac{bm_\perp^2}{z}\right) \quad (22)$$

676 The process can be thought as follows: first start from the q -leg of a $q\bar{q}$ system
677 and choose to consider the breaking to new $q'\bar{q}'$ pair closest to this leg. Now the
678 breaking will produce a hadron $q\bar{q}'$ and a remainder system spanning from $q'\bar{q}$.
679 Then the process is continued until the \bar{q} -leg is reached. A small detail here is
680 that in equation (21) it is assumed that the mass of the remainder system is large.
681 Thus some patching up is needed for the last two hadrons coming from a string.
682 The patching up is done such that the place where it happens looks as closely like
683 any other string break as possible.

684 One additional possibility one must consider is that a string can have such a
685 low mass that it cannot break at all. In this case a single hadron is generated out
686 of the string and if necessary energy and momentum are exchanged with other
687 partons in the event.

688 After all the hadrons are produced, the short-lived ones can still decay before
689 the set of final state particles in the simulation is obtained []

690 Cluster model

691 Instead of a string model HERWIG [] uses a cluster model [67] for hadronisation.
692 The advantage of cluster models is that they require a smaller number of param-

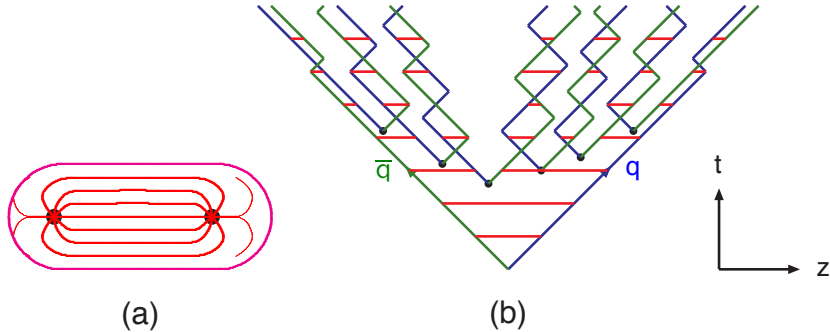


Figure 13: (a) A flux tube spanned between a quark and an antiquark. (b) The motion and breakup of a string system, with the two transverse degrees of freedom suppressed (diagonal lines are (anti)quarks, horizontal ones snapshots of the string field). [66]

eters than string models. The model is based on the preconfinement property of parton showers, i.e. the colour structure of the shower at any evolution scale Q_0 is such that colour singlet combinations of partons can be formed with an asymptotically universal invariant mass distribution. The invariant mass does not depend on the initial hard process scale Q , but only on Q_0 and the QCD scale Λ_{QCD} , when $Q \gg Q_0$.

The cluster model starts from transforming all gluons non-perturbatively into $q\bar{q}$ pairs, which requires that the gluons get a mass, which must be at least twice the lightest quark mass. After the gluons are transformed into quarks, the adjacent colour lines can be clustered together to colour singlet states with mesonic quantum numbers. The momentum of these clusters is defined to be the sum of the momenta of the clustering partons. According to preconfinement, the mass distribution of these clusters is independent of the details of the hard scattering. Additionally the clusters can be regarded as highly excited hadron resonances and decayed into the final state hadrons.

Some of these initial clusters are too heavy to reasonably describe an excited state of a hadron. These must be split before they are allowed to decay. The cluster C is split if its mass fulfills the condition []

$$M_C^p \geq M_{\max}^p + (m_1 + m_2)^p, \quad (23)$$

where $m_{1,2}$ are the masses of the constituents partons of the cluster and M_{\max} and p are the main parameters of the model. These have to be chosen separately for clusters containing light, charmed and bottom quarks. When a cluster is split, a pair of light quarks is generated from the vacuum and two new clusters are made, both containing one quark from the original cluster and one from the newly gen-

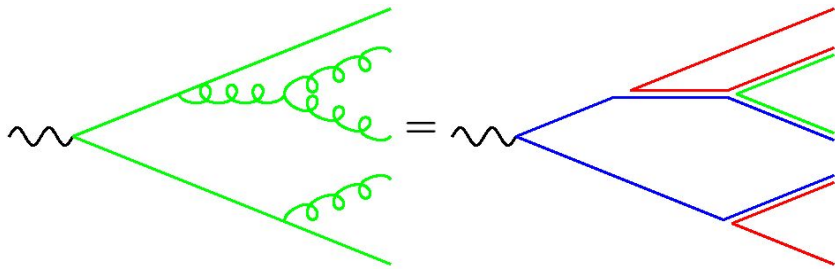


Figure 14: Colour structure of a parton shower to leading order in N_c . [66]

erated pair. The splitting is continued until no clusters with masses M_C fulfilling the equation 23 remains.

When the clusters are light enough, they decay into final state hadrons. If the mass of the cluster is high enough for decaying into a baryon-antibaryon pair, there is a parameter deciding whether the cluster undergoes mesonic or baryonic decay. For a mesonic decay a quark-antiquark pair is created from the vacuum and for the baryonic decay a diquark-antidiquark pair is made. Then the exact decay products are chosen and the cluster decays isotropically in the rest frame of the cluster. If there are partons produced in the perturbative phase involved in the decay, they retain their original direction in the cluster rest frame, up to some Gaussian smearing. If the cluster mass is too low to decay into a pair of mesons, it decays into the lightest possible hadron and some energy and momentum is exchanged with the adjacent clusters. At the end we are left with the final state hadrons, some of which might still decay until the end of the simulation if they are very short-lived. []

1.5.3 Jet energy loss

Discovery of jet quenching via leading hadron suppression

First evidence of jet quenching comes from observing high p_T tracks, i.e. the leading hadrons.

Jet quenching in heavy-ion collisions is usually quantized with the nuclear modification factor R_{AA} , which is defined as

$$R_{AA}(p_T) = \frac{(1/N_{AA}^{evt}) dN^{AA}/dp_T}{\langle N_{coll} \rangle (1/N_{pp}^{evt}) dN^{pp}/dp_T} \quad (24)$$

where dN^{AA}/dp_T and dN^{pp}/dp_T are the yields in heavy-ion and proton-proton collisions, respectively and $\langle N_{coll} \rangle$ is the average number of binary nucleon-nucleon collisions in one heavy-ion event. The number of binary collisions can be calculated from the Glauber model as shown in Sec. 1.3.2. From the point of view of direct

741 production a heavy-ion collision can be estimated relatively well to be only a series
 742 of proton-proton collisions.

743 If the medium has no effect on high p_T particles the nuclear modification factor
 744 should be 1. At RHIC and LHC this has been observed to be as low as 0.2 because
 745 of jet quenching. Measurements of R_{AA} from different sources are shown in Fig. 15

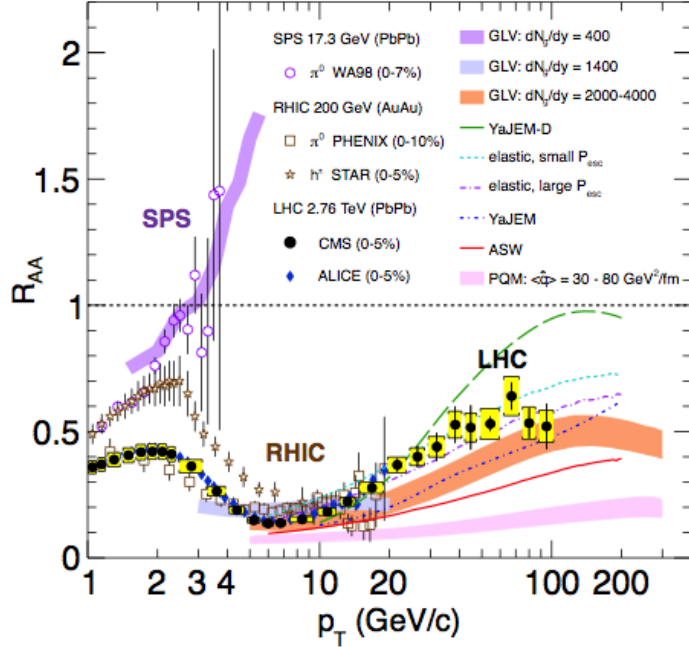


Figure 15: Measurements of the nuclear modification factor R_{AA} in central heavy-ion collisions at three different center-of-mass energies, as a function of p_T , for neutral pions (π^0), charged hadrons (h^\pm), and charged particles [68–72], compared to several theoretical predictions [34, 73–77]. The error bars on the points are the statistical uncertainties, and the yellow boxes around the CMS points are the systematic uncertainties. The bands for several of the theoretical calculations represent their uncertainties [78].

746 The nuclear modification factor can also be used to quantify anisotropy. In
 747 the study of anisotropy R_{AA} in-plane and out-of-plane can be compared. The
 748 distance traveled through medium is largest out-of-plane which leads to stronger
 749 suppression in this direction. The nuclear modification factor as a function of
 750 $\Delta\phi = \phi - \psi_n$ is given by

$$\begin{aligned}
R_{AA}(\Delta\phi, p_T) &= \frac{(1/N_{AA}^{evt}) d^2 N^{AA} / d\Delta\phi dp_T}{\langle N_{coll} \rangle (1/N_{pp}^{evt}) dN^{pp} / dp_T} \approx \frac{dN^{AA} / dp_T (1 + 2 \cdot v_2 \cos(2\Delta\phi))}{\langle N_{coll} \rangle dN^{pp} / dp_T} \\
&= R_{AA}^{incl}(p_T) (1 + 2 \cdot v_2 \cos(2\Delta\phi)). \tag{25}
\end{aligned}$$

The yield of proton-proton collisions is independent of the reaction plane and the yield in heavy-ion collisions is modulated by the second harmonics. In Eq. (25) R_{AA} is approximated only up to the second harmonics. From Eq. (25) it follows that

$$\frac{R_{AA}(0, p_T) - R_{AA}(\pi/2, p_T)}{R_{AA}^{incl}(p_T)} \approx \frac{R_{AA}^{incl}(p_T) (1 + 2 \cdot v_2 - (1 - 2 \cdot v_2))}{R_{AA}^{incl}(p_T)} = 4 \cdot v_2 \tag{26}$$

The observed $R_{AA}(\Delta\phi, p_T)$ from PHENIX measurements in Au-Au collisions at $\sqrt{s} = 200\text{GeV}$ [79] is compared to R_{AA} using v_2 via Eq. (25) in Fig. 16. They agree very well within the statistical errors for all centrality and p_T bins.

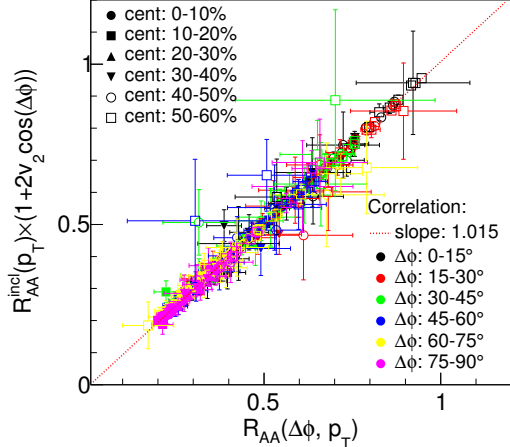


Figure 16: A comparison between observed $R_{AA}(\Delta\phi, p_T)$ and R_{AA} using v_2 from PHENIX measurements of Au-Au collisions at $\sqrt{s} = 200\text{GeV}$. On the X-axis is the measured $R_{AA}(\Delta\phi, p_T)$. On the y-axis is the inclusive R_{AA} multiplied by $1 + 2v_2 \cos(\Delta\phi)$ [79].

At high- p_T , the pQCD processes are dominant, hence the v_n (or $R_{AA}(\Delta\phi, p_T)$) characterize the pathlength-dependence of the energy loss process.

Jet quenching is not the only high p_T phenomenon studied in heavy-ion collisions. Another property is jet fragmentation. The high momentum parton created in the initial collision fragments into a number of partons with smaller p_T . Jet fragmentation occurs also in proton-proton collisions in the vacuum, but it can be modified due to the presence of the medium. In order to study the jet fragmentation function ($D(z)$, where $z = p_T^h/p_T^{part}$) modification due the medium, we use the two-particle correlations. The particle yield can be extracted from the correlation function. The background from the flow processes is correlated and needs to be subtracted to get the particle yield associated only with the jet. The ratio of the jet yields in Au-Au and p-p collision $I_{AA} = Y^{Au+Au}/Y^{p+p}$ characterizes the jet fragmentation modification [80]. I_{AA} probes the interplay between the parton production spectrum, the relative importance of quark-quark, gluon-gluon and quark-gluon final states, and energy loss in the medium.

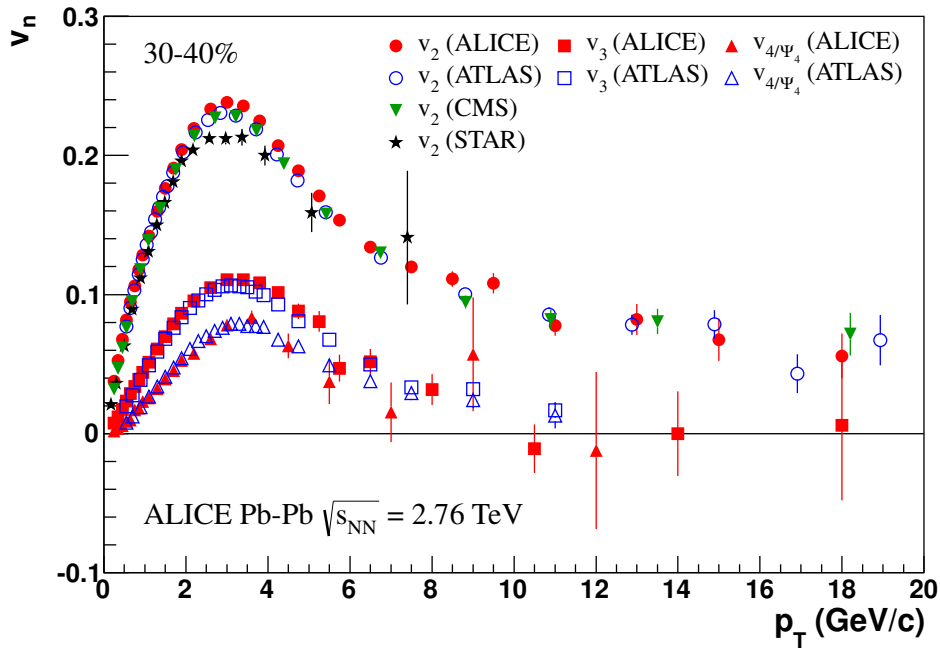


Figure 17

773 Theory of jet quenching

High momentum particles are very rare and they are only produced in the initial collisions. After they are created they escape the medium before a thermal equilibrium is reached. Thus they are not part of the pressure-driven collective expansion. Instead high momentum yield is suppressed because of energy loss in

778 the medium. When propagating through the medium these partons lose energy as
 779 they pass through the medium. This is referred to as jet quenching. Jet quenching
 780 depends on the path lengths through the medium. Thus anisotropy in this region
 781 is mainly dependent on the collision geometry and density of medium.

782 The energy loss of partons in medium is mainly due to QCD bremsstrahlung
 783 and to elastic scatterings between the parton and the medium.

784 The radiative energy loss mechanism is given in terms of the transport coef-
 785 ficient $\langle \hat{q} \rangle$, which describes the average momentum transfer between the medium
 786 and parton [81]. The exact definition of this depends on the theoretical formalism
 787 used to describe the energy loss mechanism.

788 Many of the energy loss models exploit the analogy between the QCD interac-
 789 tion of parton propagating through the colored medium and the QED energy loss
 790 of electron propagating through material. An electron propagating through matter
 791 loses its energy by photon Bremsstrahlung radiation. In the simplest case, each
 792 individual scattering center results in a single emission of a photon. This is known
 793 as the Bethe-Heitler regime [82]. The energy spectrum of radiated photons dN/dE
 794 is, in this case, proportional to $1/E$. However, the Bremsstrahlung photon, can be
 795 radiated only when the distance between the scattering centers is larger than the
 796 formation length. In the limit, when the scattering centers are closer than the
 797 formation length, the Bremsstrahlung process is suppressed. This phenomenon
 798 is known as the Landau-Pomeranchuk-Migdal (LPM) [83, 84] suppression. The
 799 radiated spectrum in this regime is proportional to $1/\sqrt{E}$.

800 Lower energy photons are further suppressed by the destructive interference
 801 leading to the suppression of Bremsstrahlung photons of $E < \gamma\omega_p$, where ω_p is
 802 the plasma frequency of the radiator. This is known as Dielectric suppression.
 803 The photon energy distribution in this regime is proportional to the energy of the
 804 photon. A schematic view of the effect of these three regimes is shown in Fig. 18.

805 The simplest energy loss process is elastic QCD scattering off the medium par-
 806 tons. In elastic scatterings the recoil energy of the scattered partons are absorbed
 807 by the thermal medium, which reduces the energy of the initial parton. The mean
 808 energy loss from elastic scatterings can be estimated by

$$\langle \Delta E \rangle_{\text{el}} = \sigma \rho L \langle E \rangle_{\text{1scatt}} \propto L, \quad (27)$$

809 where σ is the interaction cross section and $\langle E \rangle_{\text{1scatt}}$ is the mean energy transfer
 810 of one individual scattering [86]. This assumption holds if the mean energy is
 811 independent of the total energy of the parton (E). The transport coefficient of
 812 elastic scattering, $\langle \hat{q}_{\text{el}} \rangle = \langle \Delta E \rangle / L$, is defined as the mean energy loss per unit path
 813 length.

814 Another energy loss mechanism is medium-induced radiation. In QCD this
 815 radiation is mainly due to the elementary splitting processes, $q \rightarrow qg_r$ and $g \rightarrow gg_r$.

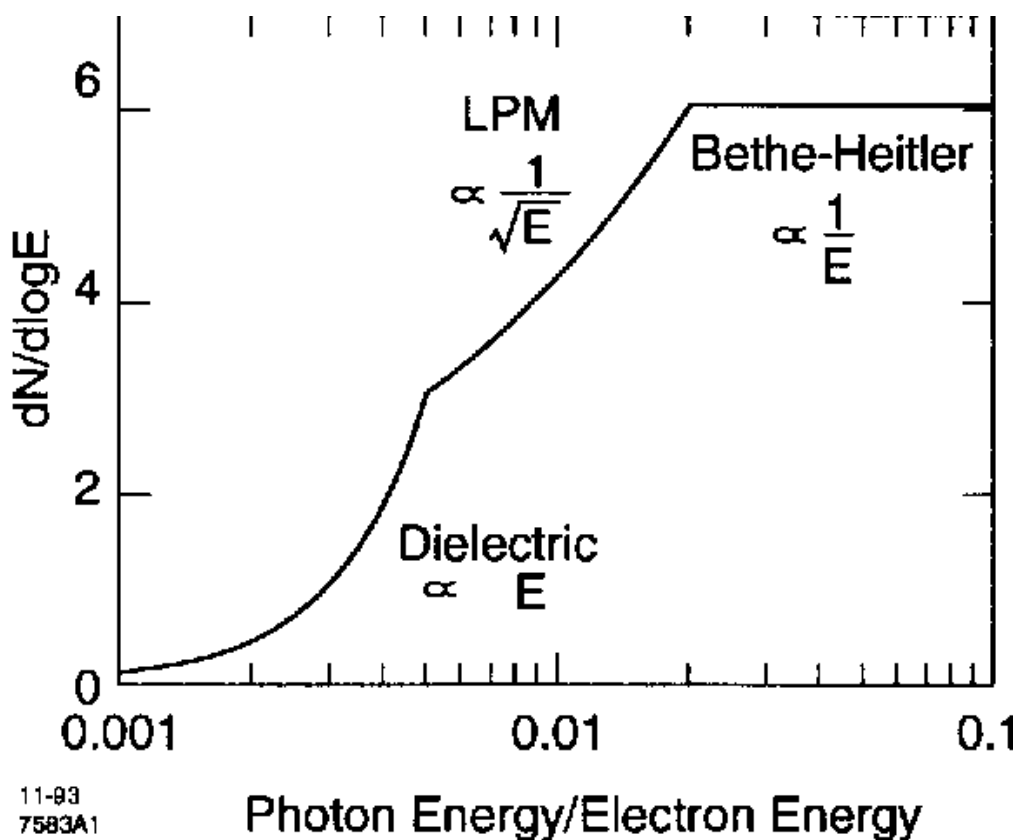


Figure 18: The expected bremsstrahlung spectrum for a electron propagating through material. [85].

816 Assuming that the parton is moving with the speed of light radiation energy loss
817 can be estimated by

$$\langle \Delta E \rangle_{rad} \propto T^3 L^2, \quad (28)$$

818 where L is the length of the medium and T is its temperature [87]. The differ-
819 ent exponents of L in equations 27 and 28 indicate that radiative energy loss is
820 dominant over elastic energy loss.

821 There are several models that attempt to describe the nature of the energy loss
822 mechanism. The most used models can be divided into four formalisms.

823 In the Gyulassy-Levai-Vitev (GLV) [88] opacity expansion model the radiative
824 energy loss is considered on a few scattering centers N_{scatt} . The radiated gluon
825 is constructed by pQCD calculation as summing up the relevant scattering am-
826 plitudes in terms of the number of scatterings. Another approach into opacity
827 expansion is the ASW model by Armesto, Salgado and Wiedermann [89].

828 Thermal effective theory formulation by Arnold, Moore and Yaffe (AMY) [90]
829 uses dynamical scattering centers. It is based on leading order pQCD hard thermal
830 loop effective field theory. This model assumes that because of the high temper-
831 ature of the plasma the strong coupling constant can be treated as small. The
832 parton propagating through the medium will lose energy from soft scatterings and
833 hard scatterings.

834 The above models calculate the energy loss while the parton propagates through
835 the medium, focusing on the pQCD part. The higher twist (HT) approach by Wang
836 and Guo [91] implements the energy loss mechanism in the energy scale evolution
837 of the fragmentation functions.

838 The last category is formed by the Monte Carlo methods. The PYTHIA event
839 generator [92] is widely used in high-energy particle physics. Two Monte Carlo
840 models based on PYTHIA describing the energy loss mechanism are PYQUEN [93]
841 and Q-Pythia [94]. Other Monte Carlo models include JEWEL [95] and Ya-
842 JEM [96].

843 1.5.4 New paradigm of jet Quenching

844 As described in the previous section there have been many experimental evi-
845 dences of jet energy loss, such as the suppression of inclusive hadron spectra at
846 high transverse momentum [97–101], the modification of back-to-back hadron-
847 hadron [80, 102] and direct photon-jet correlations [103], and the modification of
848 reconstructed jet spectra [104] and jet substructure [105–107], as compared to the
849 expectations from elementary proton-proton collisions.

850 The first indications of jet quenching, such as R_{AA} , looked essentially at the
851 leading hadrons of jets, the hard part, ignoring the soft scale part of jet phenomena.

852 However, experimental methods have since improved; jet reconstruction algorithms
 853 have become reliable in the LHC era. Instead of the leading hadron we can study
 854 the entire jet shower.

855 -Jet RAA -Jetscape

856 Thus the new paradigm in jet quenching in heavy-ion collisions involves multi-
 857 scale problems [108, 109]. The elementary scattering and the subsequent branching
 858 process down to non-perturbative scales are dominated by hard scales in the vac-
 859 uum as well as in the medium. Soft scales, of the order of the temperature of
 860 the medium, characterise the interactions of soft partons produced in the shower
 861 with the QGP. Soft scales also rule hadronisation, which is expected to take place
 862 in vacuum for sufficiently energetic probes, even though some modifications can
 863 persist from modifications of color flow [110–112]. Understanding the contribu-
 864 tions from the different processes to the jet shower evolution in medium and their
 865 scale dependence is crucial to constrain the dynamics of jet energy loss in the
 866 expanding medium, the role of colour coherence [113], and fundamental medium
 867 properties like temperature dependent transport coefficient [114, 115].

868 **Lund diagram**

869 The different momentum and angular scales are subject to different physical phe-
 870 nomena. Figure 19 shows the relevant medium modification phenomena for differ-
 871 ent regions of the phase space at time t , when a jet propagates through a thermal
 872 cloud of temperature T . As in practice jets propagate over a finite path-length
 873 L in QCD matter, Fig. 19 can be taken as a representation of the distribution of
 874 partonic jet fragments at moment $t \approx L$, when the jet escapes the medium.

875 The region marked as DGLAP is dominated by the primary vacuum splittings.
 876 This region is determined by $\theta > \theta_{\text{vac}}$ with

$$\theta_{\text{vac}} \propto 1/\sqrt{pt}. \quad (29)$$

877 Medium-induced parton branching fills the log p -log- θ -plane from the bottom
 878 up (in p) and from the inside out (in θ). This is because transverse momentum is
 879 acquired by Brownian motion in the medium, $k_{\perp}^2 \propto \hat{q}t$. Then the formation time
 880 constraint $t \geq p/k_{\perp}^2 \approx p/\hat{q}t$ implies that medium-induced quanta can be formed in
 881 the region $p \leq k_{\text{form}}$ where

$$k_{\text{form}}(t) = \hat{q}t^2$$

882 .

883 The probability of finding a splittee with a momentum p with $p < k_{\text{form}}$ is

$$\frac{dP_{\text{find}}(t)}{d \log p} \propto \alpha_s t/t_{\text{form}}(p) \propto \alpha_s \hat{q}^{nicefrac{1}{2}} p^{-1/2} t \quad (30)$$

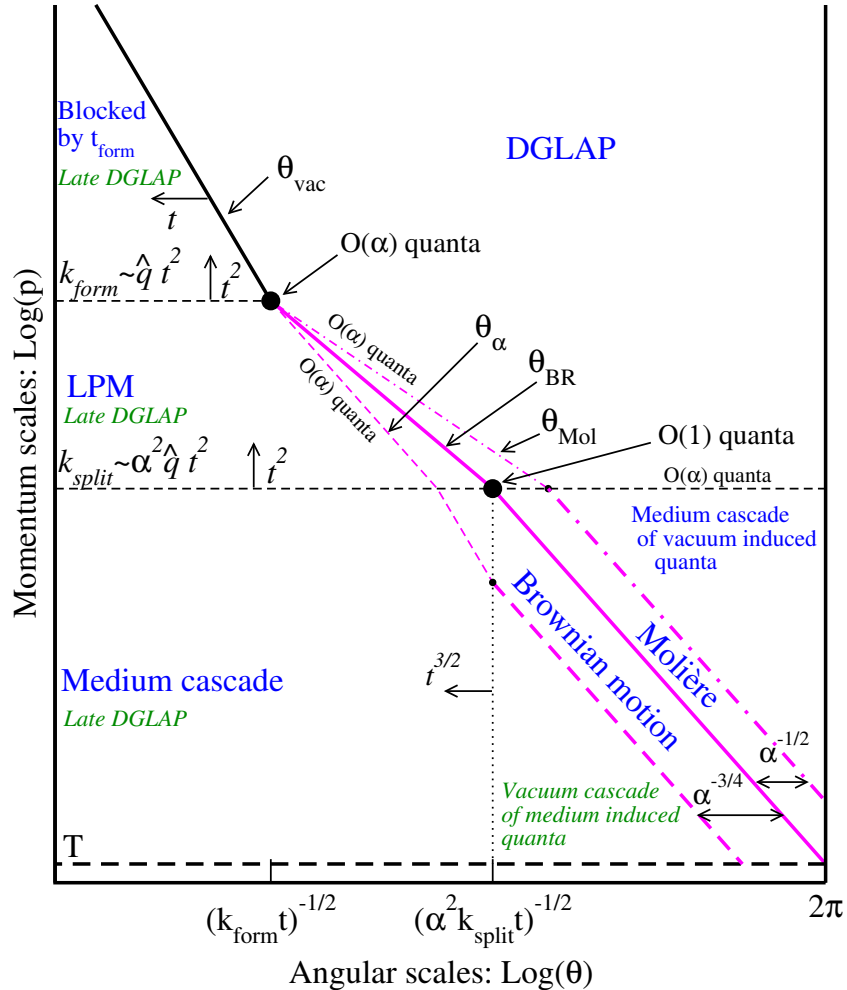


Figure 19: Parametrically accurate picture of how a medium-modified parton cascade fills the phase space. At time t , quanta can be formed up to momentum scale k_{form} and they are formed with $O(1)$ probability per $\log p$ at lower scale k_{split} . Quanta below k_{split} split further and their energy cascades to the thermal scale T in less than an epoch t . Transverse Brownian motion moves quanta up to the angle $\theta_{\text{BR}}(p)$ denoted by the thick purple line. The Molière region at larger θ is dominated by rare large angle scattering. At even larger angle, there are $O(\alpha_s)$ quanta per double logarithmic phase space from DGLAP ‘vacuum’ radiation, and for momenta below k_{split} these cascade within time t to T . After the jet escapes the medium, the jet and the emitted fragments will undergo vacuum radiation. This late time vacuum radiation emitted by the original parton dominates at sufficiently small $\log \theta$ (regions marked “late DGLAP” and bounded by θ_{vac} and θ_α), whereas the late time radiation of the fragments dominates in the region denoted by “Vacuum cascade of the medium induced quanta”. [108].

Not all quanta will stay where they were created. Those modes that have time to lose a significant fraction of their energy will cascade to a significantly lower scale p . For LPM-type radiation, the splitting that degrades energy the most is the hardest splitting.

The $\log p$ distribution has the same $\frac{1}{\sqrt{p}}$ dependence as in the LPM region

$$\frac{dn}{d \log p} = \frac{1}{p} \frac{d\epsilon}{d \log p} \approx \alpha_s \frac{\sqrt{\hat{q}t}}{\sqrt{p}} \quad (31)$$

Also the quanta originating from the DGLAP region will undergo medium interactions that will make the quanta radiate and split. The distribution of radiation is the same as from any other mode. Above a certain momentum scale k_{split} the distribution of originating daughters is

$$\frac{dP_{\text{find}}}{d \log p d \log \theta} \approx \alpha_s \frac{t}{t_{\text{split}}(p)}, \quad (32)$$

Note that the ratio t/t_{split} is smaller than 1 for nodes above k_{split} and therefore the number of daughters is smaller than the number of vacuum splitted quanta. Below k_{split} the cascade is similar to the medium cascade and the number of quanta become

$$\frac{dn}{d \log p d \log \theta} \approx \alpha_s \frac{t}{t_{\text{split}}(p)}, \text{ for } p < k_{\text{split}}(p) \quad (33)$$

The angular distribution is driven by two mechanisms; Multiple soft scatterings give rise to transverse Brownian motion, which determines the distribution at small angles. The typical angle reached in the LPM region is

$$\theta_{\text{BR}}(p) \approx \frac{\sqrt{\hat{q}t}}{p}, \text{ for } k_{\text{form}} > p > k_{\text{split}}, \quad (34)$$

while in the medium cascade region of the phase space this becomes

$$\theta_{\text{BR}}(p) \approx \left(\frac{T}{p}\right)^{\frac{3}{4}} \quad (35)$$

Large angular scales cannot be reached by Brownian motion, but can arise from rare large angle scatterings, described by Molière [].

1.5.5 Jet shape measurements

1.6 QGP in Small systems

After the existence of QGP in heavy-ion collisions has been established, attention has been turned to small systems. Proton-proton (pp) and proton-Lead (pPb)

907 collisions have been studied at LHC and RHIC has studied a host of different
 908 collision systems; namely proton-Gold (pAu), deuteron-Gold (dAu) and Helium³-
 909 Gold (³HeAu) collisions starting in 2000.

910 Already before the era of modern colliders, collective behaviour in proton-
 911 proton collisions was considered by names like Heisenberg, Fermi and Bjorken. [116]
 912 Eventually there were some experimental searches of QGP in pp and $p\bar{p}$ collisions
 913 in E735 at Tevatron [117] and MiniMAX [118]. However no conclusive evidence
 914 was found.

915 In the early years of RHIC these small systems were mostly considered as con-
 916 trol measurement, for example in constraining nuclear modified parton distribution
 917 functions (nPDFs) that determine the initial gluon distributions that determine
 918 the first epoch of heavy-ion collisions [119, 120].

919 In 2010 ultrahigh-multiplicity pp collisions were studied at CMS. The study
 920 found that particles had a weak but clear preference to be emitted along a com-
 921 mon transverse ϕ angle across all rapidities [121]. This seemed like behaviour
 922 were similar to AA collisions, but it was argued that it could as well come from
 923 momentum correlations present in the earliest moments of the collision.

924 In 2012 LHC ran its first pPb data taking period. Around the same time
 925 dAu data was reexamined at RHIC. Now it was revealed that most of the flow
 926 signatures attributed to hydrodynamic expansion in AA collisions also existed in
 927 smaller systems.

928 -Sub nucleonic structure needed to describe intial conditions in pA, pp

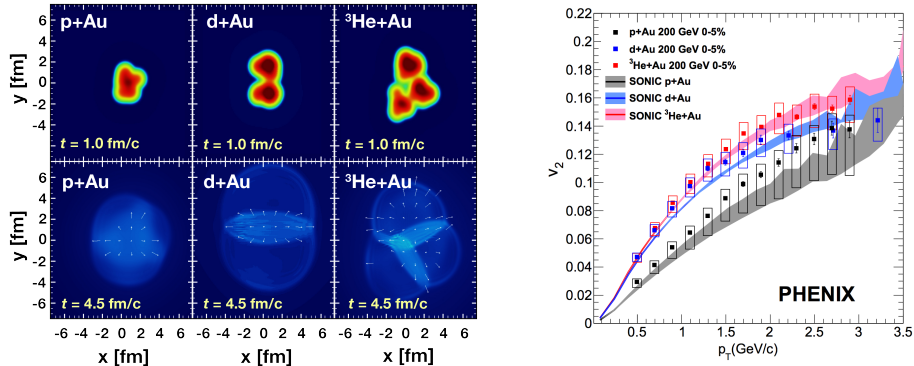


Figure 20: Calculations of the intial energy density in small collision systems at RHIC and the resulting hydrodynamic evolution.

929 **1.6.1 Collective phenomena**

930 The most rugged analysis of collective behaviour concerns the two (or more) parti-
 931 cle correlations, often parametrised via the relative azimuthal angle and pseudora-
 932 pidity differences, $\Delta\phi$ and $\Delta\eta$ respectively. Figure 21 shows two-particle correla-
 933 tions measurements in PbPb, pPb and pp collisions at the LHC. In PbPb collisions
 934 long-range correlations dominate over short-range phenomena. This shows in the
 935 two ridges at $\Delta\phi = 0$ and $\Delta\phi = \pi$. At $\Delta\phi \approx \Delta\eta \approx 0$, there is a peak coming from
 936 single jet fragmentation. Since the away-side jet can be spread out in $\Delta\eta$, this
 937 contribution disappears when compared to the flow contribution at the away side
 938 ridge. In pPb, and pp the near side peak is more distinguished and the away-side
 939 jet contribution starts to show. Still, one can see long-range correlations that seem
 940 like flow-like collective behaviour in both systems.

941 In addition to the two particle correlations, correlations have been observed in
 942 the form of v_n coefficients both at LHC and at RHIC. The results have also been
 943 described with hydrodynamical models, although the applicability of said models
 944 is questionable, because of the large Reynolds numbers in small systems. Figure
 945 20 shows results for v_2 in different collisions systems at RHIC as measured by
 946 PHENIX. These different systems provide also different initial geometries. dAu
 947 collisions naturally have an ellipsoidal form, while a He3 collision has a triangular
 948 form and thus produces larger triangular flow, v_3 components.

949 Other observations that produce flow-like results include mass ordered v_2 coeffi-
 950 cients and higher order harmonics coming from fluctuations in the initial geometry.
 951 Thus all the major collective flow phenomena observed in heavy-ion collisions have
 952 been also identified in small systems.

953 One open question is identifying the point the point, where flow-like correla-
 954 tions end. The question has proved challenging since low multiplicity events are
 955 dominated by non-flow phenomena. This makes observations in low multiplicity
 956 events model/method dependant. Different methods assess non-flow contributions

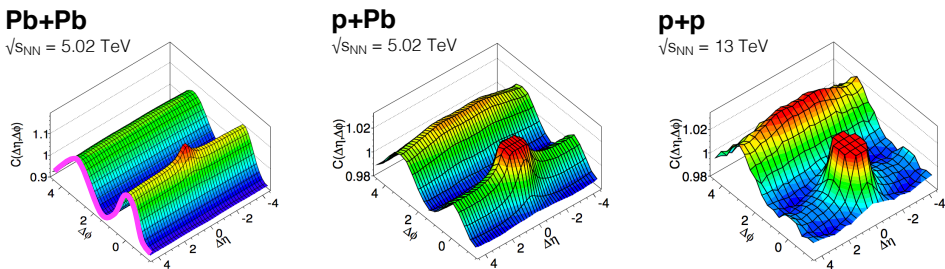


Figure 21: Two-particle correlation results in PbPb, pPb, and pp collisions at the LHC [1].

957 differently. Thus some methods fail to observe a signal in cases, where others do
958 and it is unclear whether this is true collective motion or it comes from non-flow
959 contributions.

960 1.6.2 Absence of jet quenching

961 In A+A collisions, an important confirmation of the standard model comes from
962 the energy loss of high p_T partons traversing the medium, referred to as jet quench-
963 ing [122–124]. In 2003 the jet quenching effect was observed to disappear in d+Au
964 collisions. This was taken as an indication that no QGP was created. Similarly at
965 LHC no jet modification has been observed in pPb collisions. Fig. 22 shows the
966 nuclear modification factor R_{pA} in pPb collisions as measured at the LHC.

967 The lack of jet modification seems surprising considering the multitude of flow
968 observations supporting the existence of QGP in small systems. One possible
969 explanation is simply the size of medium. In PbPb collision partons traversing
970 through the medium lose energy to the medium. If the medium is very small there
971 is limited time for interaction with the medium.

972 Calculations indicate that there should be modification in the most central
973 pPb collisions, but selecting these in the analysis is complicated. In PbPb colli-
974 sions most of the particle production comes from the medium and thus the total
975 multiplicity is a good indicator of centrality. In pPb collisions, however the total
976 multiplicity is smaller and is more strongly influenced by jet phenomena. Events
977 with jets have naturally larger multiplicities and are more likely to be classified as
978 central events.

979 So far the only observable indicative of jet quenching in pPb collisions is the
980 high $p_T v_2$. In heavy-ion collisions this is not explained by hydrodynamics. Instead
981 it is assumed to come from jet quenching with different path lengths through the
982 medium in different directions. In Fig.22 ATLAS and CMS measurements of v_2 in
983 pPb and PbPb collisions are shown. The pPb results seem to follow a very similar
984 pattern.

985 1.6.3 Centrality determination in small systems

986 In lead-lead collisions the total multiplicity of the event is a good indicator of the
987 centrality of the collision. In proton-lead collisions the connection of multipli-
988 city and centrality is less clear. In p-Pb collisions the impact parameter is only
989 loosely correlated to N_{part} or N_{coll} . Hence, although one uses traditionally the
990 term centrality to refer to these measurements, the relevant parameters are N_{part}
991 and N_{coll} [1].

992 The Glauber model [43] is generally used to calculate geometrical quantities of
993 nuclear collisions (A-A or p-A). In this model, the impact parameter b controls the

Table 2: Summary of observations in small system

Observable	PbPb	pPb	pp
Jet RpA/RAA	Modified	No modification	-
Hadron RpA/RAA	Modified	No modification	-
Heavy flavors			
Jet shape	Broadening	No observations	-
Two-particle correlations	Ridge	Ridge	Ridge
v_2	Observed	Observed	Observed
Mass ordered flow			
Higher ordered harmonics			
High $p_T v_2$	Observed	Maybe	-

994 average number of participating nucleons N_{part} and the corresponding number of
995 collisions N_{coll} . It is expected that variations of the amount of matter overlapping
996 in the collision region will change the number of produced particles, and parameters
997 such as N_{part} and N_{coll} have traditionally been used to describe those changes
998 quantitatively, and to relate them to pp collisions.

999 The problem in p–Pb collisions, is that fluctuations in multiplicity coming from
1000 for example hard scatterings are of the same order as the differences in multiplicity
1001 between centrality classes. In Pb–Pb collisions these multiplicity fluctuations have
1002 little influence on the centrality determination, the range of N_{part} or N_{coll} is large
1003 and $P(M|v)$ converges quickly to a Gaussian with a small width relative to the
1004 range of v .

1005 Thus in practice selecting high multiplicity one chooses not only large average

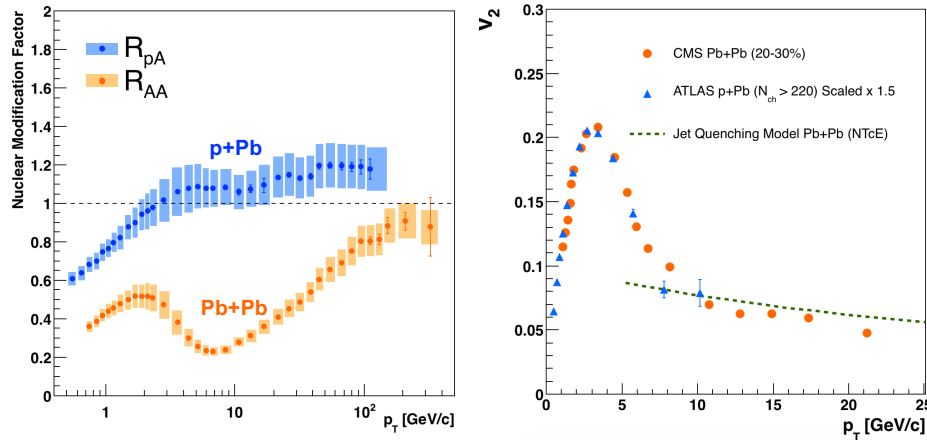


Figure 22: RpA in proton-lead collisions

1006 N_{part} , but also positive multiplicity fluctuations leading to deviations from the
 1007 binary scaling of hard processes. These fluctuations are partly related to qualita-
 1008 tively different types of collisions. High multiplicity nucleon-nucleon collisions
 1009 show a significantly higher particle mean transverse momentum. They can be
 1010 understood as harder collisions with larger momentum transfer Q^2 or as nucleon-
 1011 nucleon collisions where multiple parton-parton interactions (MPI) take place.
 1012 This is illustrated in Fig. 24.

1013 Of particular interest are estimators from kinematic regions that are causally
 1014 disconnected after the collision. The measurement of a finite correlation between
 1015 them unambiguously establishes their connection to the common collision ge-
 1016 ometry. Typically these studies are performed with observables from well sep-
 1017 arated pseudorapidity (η) intervals, e.g. at zero-degree (spectators, slow-nucleons,
 1018 deuteron break-up probability) and multiplicity in the rapidity plateau.

1019 One centrality selection that is argued not to induce a bias on the binary scaling
 1020 of hard processes is provided by the energy measurement with the Zero Degree
 1021 Calorimeters (ZDC) in ALICE, due to their large η -separation from the central
 1022 barrel detectors. They detect the "slow" nucleons produced in the interaction by
 1023 nuclear de-excitation processes or knocked out by wounded nucleons.

1024 Additional kinematic biases exist for events containing high- p_T particles, which
 1025 arise from the fragmentation of partons produced in parton-parton scattering with
 1026 large momentum transfer. Their contribution to the overall multiplicity increases
 1027 with increasing parton energy and thus can introduce a trivial correlation between
 1028 the centrality estimator and the presence of a high- p_T particle in the event. For
 1029 very peripheral collisions, the multiplicity range that governs the centrality for the
 1030 bulk of soft collisions can represent an effective veto on hard processes. For the

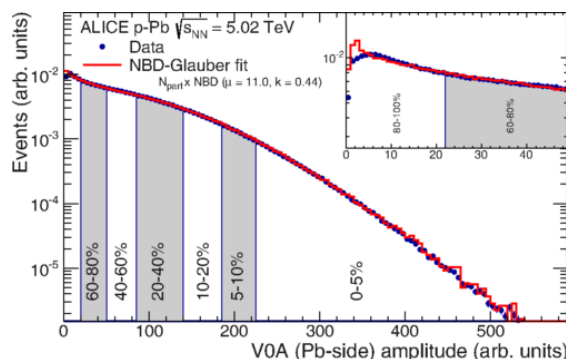


Figure 23: Distribution of the sum of amplitudes in the V0A hodoscopes (Pb-
 going), as well as the NBD-Glauber fit (explained in the text). Centrality classes
 are indicated by vertical lines. The inset shows a zoom-in on the most peripheral
 events. [1]

₁₀₃₁ nuclear modification factor this would lead to $R_{\text{pPb}} < 1$.

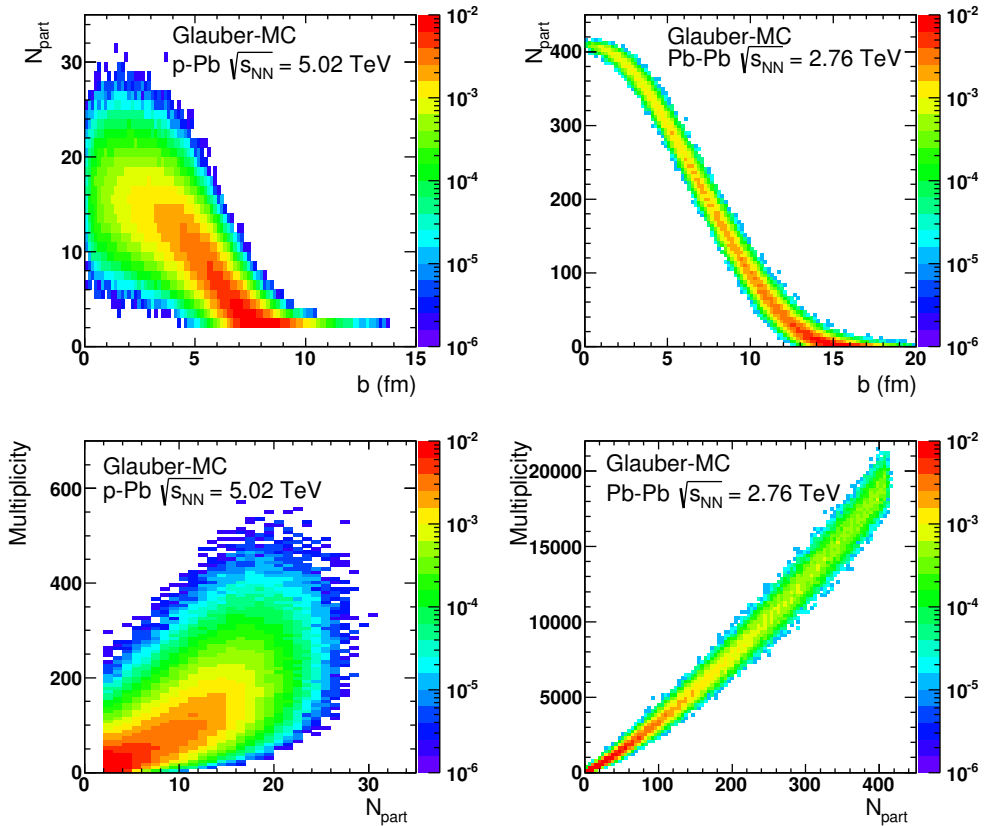


Figure 24: Top: Scatter plot of number of participating nucleons versus impact parameter; Bottom: Scatter plot of multiplicity versus the number of participating nucleons from the Glauber fit for V0A. The quantities are calculated with a Glauber Monte Carlo of p-Pb (left) and Pb-Pb (right) collisions. [1]

1032 2 Experimental Setup

1033 2.1 CERN

1034 The European Organization for Nuclear Research (CERN), established in 1954, op-
 1035 erates the largest particle physics laboratory in the world. In 2019 CERN consists
 1036 of 22 member states. Additionally CERN has contacts with a number of associate
 1037 member states and various individual institutions. The laboratory, also referred
 1038 to as CERN, itself is located near Geneva at the border of France and Switzerland
 1039 employs about 2500 people. Additionally some 12000 visiting scientists from over
 1040 600 institutions in over 70 countries come to CERN for their research.

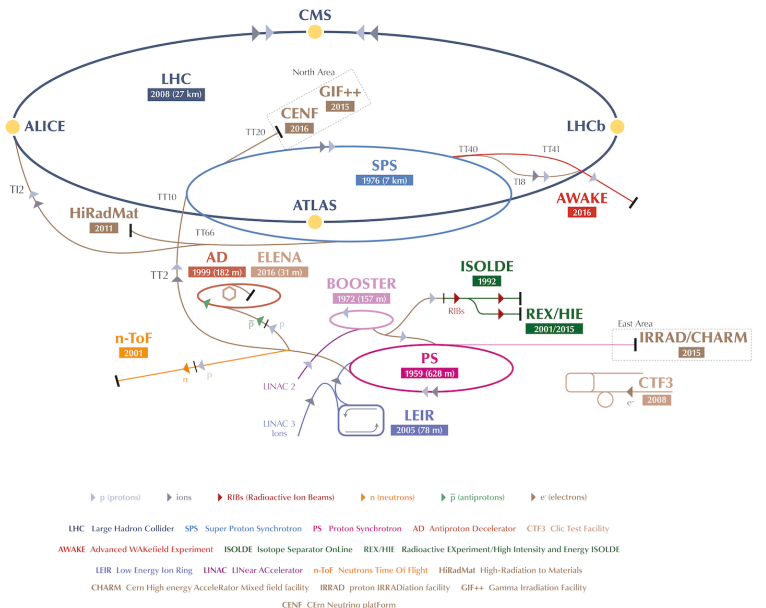


Figure 25: A schematic view of the accelerator complex at CERN. Before particles can be injected into the LHC they require a series of accelerators with increasing size. Until 2018 protons started their journey in LINAC2 (Linear Accelerator) and continue through the Booster, Proton Synchrotron (PS) and Super Proton Synchrotron (SPS). Between 2019 and 2020 LINAC2 will be replaced by LINAC4 [125]

1041 The laboratory includes a series of accelerators, which are used to accelerate
 1042 the particle beams used. A schematic view of the complex as of 2019 is shown in
 1043 Figure 25. In the framework of this thesis the most important component is the
 1044 Large Hadron Collider (LHC), the largest collider at CERN. LHC will be discussed

in more detail in Sec. 2.2. Other accelerators in the series are used to inject the particle beams into LHC, but they are also used in itself for various experimental studies.

The second largest accelerator is the super proton synchrotron (SPS). It is the final step before the particle beam is injected into LHC. Commissioned in 1976, it was the largest accelerator at CERN until the the Large Electron-Positron Collider (LEP) was finished in 1989. Originally it was used as a proton-antiproton collider and as such provided the data for the UA1 and UA2 experiments, which resulted in the discovery of the W and Z bosons [126]. At the moment there are several fixed target experiments utilising the beam from the SPS. These study the structure (COMPASS) and properties (NA61/SHINE) of hadrons, rare decays of kaons (NA62) and radiation processes in strong electromagnetic fields (NA63). Additionally the AWAKE and UA9 experiments are used for accelerator research and development.

The third largest accelerator in CERN is the proton synchrotron (PS). Capable of accelerating beams up to an energy of 25 GeV PS provides the beam to SPS. Additionally PS has experiments for studying strong force (DIRAC), the effect of cosmic rays on cloud formation (CLOUD) and neutron-nucleus interactions (nTOF).

Additionally PS provides the beam to the antiproton decelerator (AD), which uses the beam and a block of metal to produce antiprotons. These are then decelerated in AD into a useful low-energy beam, which is provided to a host of experiments studying the properties of antimatter.

PS gets proton beams from LINAC2 through BOOSTER and ion beams from LINAC3 through LEIR. From BOOSTER beams are also provided to the On-Line Isotope Mass Separator (ISOLDE). ISOLDE directs the beam into thick targets to produce low energy beams of radioactive nuclei. These beams are used to study the properties of even the most exotic of atomic nuclei in a host of experiments.

More information of the various experiments at CERN can be found online from [127].

2.2 Large Hadron Collider

The Large Hadron Collider (LHC) with its circumference of 26.7 km is the largest accelerator at CERN and the largest particle collider ever built. The LHC is designed to accelerate protons up to an energy of 8 TeV and lead ions up to 2.76 TeV per nucleon [128]. The design luminosity of the LHC is $10^{34} \text{ cm}^{-2}\text{s}^{-1}$. In 2017 it achieved a record peak luminosity of $2 \cdot 10^{34} \text{ cm}^{-2}\text{s}^{-1}$. For lead beams luminosities of up to $6 \cdot 10^{27} \text{ cm}^{-2}\text{s}^{-1}$ were reached in 2018. All this is achieved with a ring consisting of 1232 superconducting dipole magnets that keep particles in orbit.

1084 The LHC receives beams with energies of 450 GeV from the SPS. In the LHC
1085 the particles are accelerated through the use of radio-frequency (RF) cavities.
1086 Electromagnetic waves become resonant and build up inside the cavity. As they
1087 consist of electromagnetic waves, the field in the RF cavity oscillates. Charges
1088 passing through the cavity feel the overall force and are pushed forward along the
1089 accelerator. Particles must enter the cavity at the correct phase of oscillation to
1090 receive a forward push. When timed correctly, the particles will feel zero acceler-
1091 erating voltage when they have exactly the correct energy. Particles with higher
1092 energies will be decelerated and particles with lower energies will be accelerated.
1093 This focuses particles in distinct bunches. The RF oscillation frequency at the
1094 LHC is 400.8 MHz. Thus RF "buckets" are separated by 2.5 ns. However only 10
1095 % are actually filled with particles, so the bunch spacing in the LHC is 25 ns, at
1096 a bunch frequency of 40 MHz.

1097 With 7 TeV proton beams the dipole magnets used to bend the beam must
1098 produce a magnetic field of 8.33 T. This can be only achieved through making
1099 the magnets superconducting, which requires cooling them down with helium to a
1100 temperature of 1.9 K. The 1232 dipole magnets make up roughly 2/3 of the LHC
1101 circumference. The remaining part is made up of the RF cavities, various sensors
1102 and higher multipole magnets used to keep the beam focused. The most notable
1103 of these are the 392 quadrupole magnets.

1104 The LHC is divided into octants, where each octant has a distinct function.
1105 Octants 2 and 8 are used to inject beam into the LHC from SPS. The 2 beams
1106 are crossed in octants 1,2,5 and 8. The main experiments are built around these
1107 crossing points. Octants 3 and 7 are used for beam cleansing. This is achieved
1108 through collimators that scatter particles with too high momentum or position
1109 offsets off from the beam. The RF cavities used for acceleration are located in
1110 octant 4 and octant 6 is used for dumping the beam. The beam dump is made
1111 up of two iron septum magnets, one for each beam, that will kick the beam away
1112 from machine components into an absorber when needed.

1113 2.2.1 LHC experiments

1114 As of 2018 there are four main experiments at the LHC; ALICE, ATLAS, CMS
1115 and LHCb and three smaller ones LHCf, TOTEM and MoEDAL. ALICE will be
1116 covered in detail in section 2.3.

1117 ATLAS (A Toroidal LHC ApparatuS) and CMS (Compact Muon Solenoid) are
1118 the two largest experiments at the LHC. They are both multipurpose experiments
1119 designed to be sensitive to many different possible new physics signals, such as ex-
1120 tra dimensions and dark matter particles. The biggest discovery made by these so
1121 far is the discovery of the Standard Model Higgs boson, which was simultaneously
1122 published by the experiments in 2012 [129,130].

1123 The LHCb (LHC beauty) experiment [131] is made for studying the bottom
1124 (beauty) quark. Main physics goals of the LHCb include the measurement of the
1125 parameters of CP violation with decays of hadrons containing the bottom quark.
1126 One of the most important results published by LHCb is the first measurement of
1127 $B_s^0 \rightarrow \mu^+ \mu^-$ decay, which was found to be in line with the Standard Model.

1128 In addition to the four large experiments there are three smaller experiments
1129 along the LHC ring. LHCf (LHC forward) [?] is located at interaction point 1 with
1130 ATLAS. It aims to simulate cosmic rays by the particles thrown forwards by the
1131 collisions in ATLAS.

1132 TOTEM (TOTal Elastic and diffractive cross section Measurement) is located
1133 near the CMS experiment at point 5. This allows it to measure particles emerging
1134 from CMS with small angles. The main goals is to measure the total, elastic and
1135 inelastic cross-sections in pp collisions [132].

1136 The MoEDAL (Monopole and Exotics Detector At the LHC) experiment [?] is
1137 located at the interaction point 8 together with the LHCb experiment. MoEDAL
1138 tries to measure signatures of hypothetical particles with magnetic charge, mag-
1139 netic monopoles.

1140 2.3 ALICE

1141 ALICE (A Large Ion Collider Experiment) [133] is the dedicated heavy ion ex-
1142 periment at the LHC. ALICE was designed to cope with the expected very high
1143 multiplicity environment of heavy ion collisions. The design allows measurement
1144 of a large number of low momentum tracks. The different detector subsystems are
1145 optimised to provide high momentum resolution and excellent particle identifica-
1146 tion capabilities over a broad range of momentum.

1147 A schematic view of the ALICE detector in 2018 is presented in Figure 26.
1148 This section will go through the composition of ALICE as it has been during run 2
1149 between 2014 and 2018. The detector will go through significant upgrades during
1150 Long Shutdown 2 (LS2) in 2019-2020.

1151 As in all the major high energy physics experiments the positioning of the de-
1152 tectors follows a layered structure. Closest to the interaction point are the tracking
1153 detectors. The main task of these detectors is to locate the position of the pri-
1154 mary interaction vertex accurately and to record the tracks of charged particles.
1155 To achieve this they need a very good spatial resolution close to the interaction
1156 point. Tracking detectors do not significantly alter the tracks of traversing parti-
1157 cles. Thus they can be located in the innermost layers.

1158 Calorimeters are designed to stop any particles hitting them and use the ab-
1159 sorption to measure the energy of the particles. Thus they must be located behind
1160 the tracking detectors. ALICE has two separate calorimeter systems, the elec-
1161 tromagnetic calorimeters measure mainly electrons and photons, while the muon

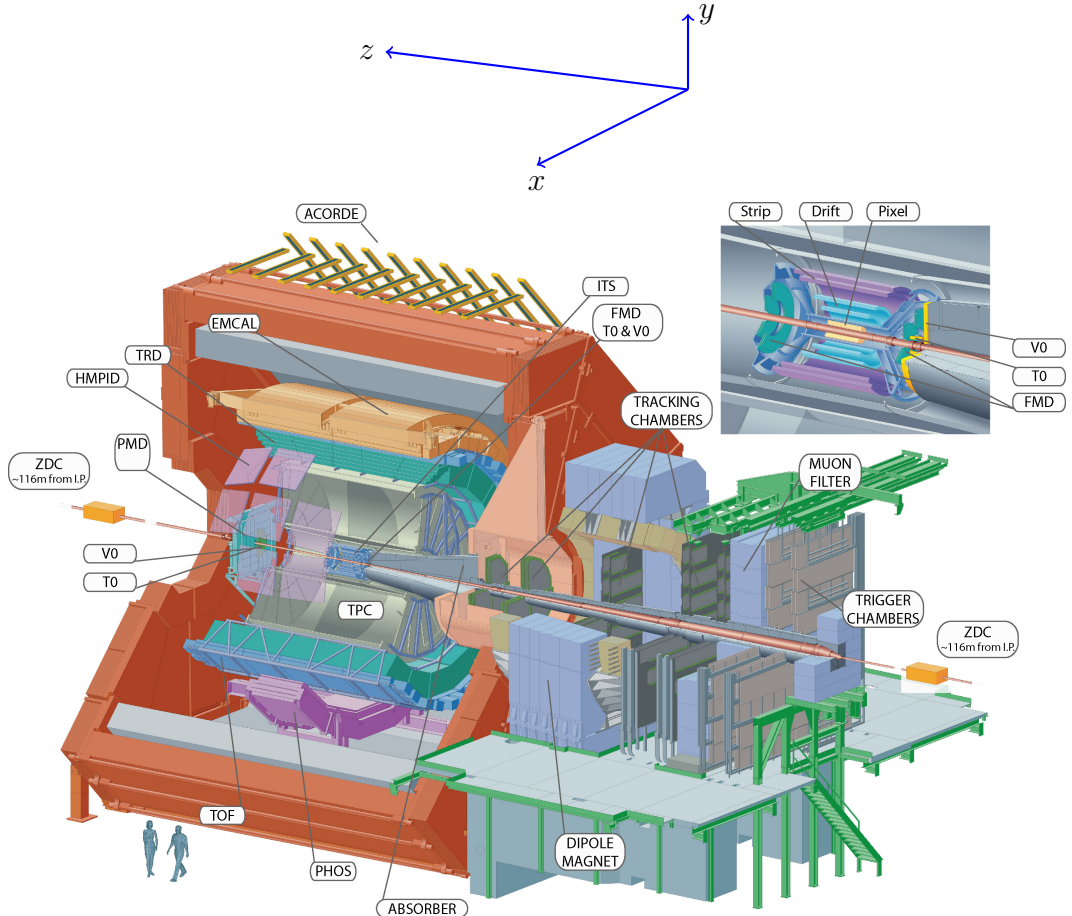


Figure 26: Schematic view of the ALICE detector with the definition of coordinates. The positive direction of *z* is also referred to as the A side and the negative direction as the C side

₁₁₆₂ detection system measures muons.

₁₁₆₃ 2.3.1 Tracking

₁₁₆₄ The main design guideline for the tracking detectors in ALICE was the require-
₁₁₆₅ ment to have good track separation and high granularity in the high multiplicity
₁₁₆₆ environment of heavy ion collisions. Before the LHC started heavy ion runs the
₁₁₆₇ wildest estimates put the particle density at 8000 charged particles per unit of ra-
₁₁₆₈ pidity [133]. In reality the particle density turned out to be significantly smaller,
₁₁₆₉ about 1600 charged particles per rapidity unit [?].

₁₁₇₀ The main tracking detector in ALICE is the Time Projection Chamber
₁₁₇₁ (TPC) [134]. TPS is discussed in more detail in section 2.3.2

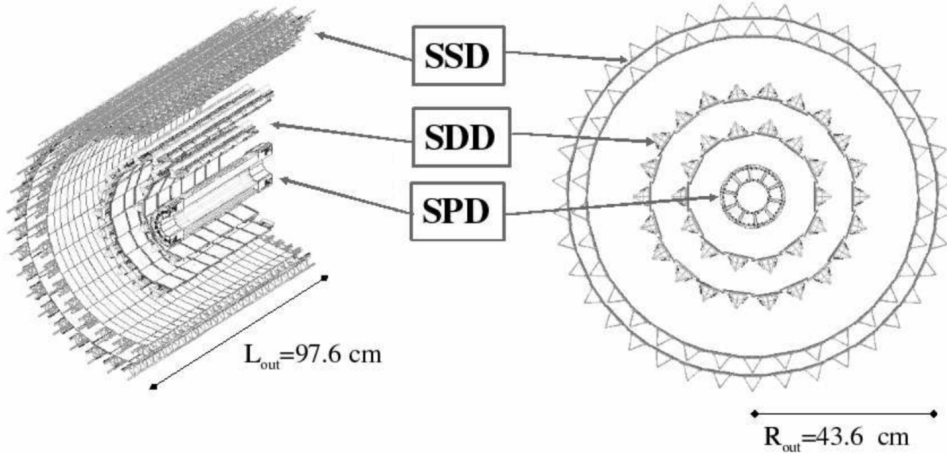


Figure 27: Schematic view of ALICE Inner Tracking System

1172 Between TPC and the beam pipe there is an array of six layers of silicon
 1173 detectors, called the inner tracking system (ITS) [135]. The main tasks of the
 1174 ITS are to locate the primary vertex with a resolution better than $100 \mu m$, to
 1175 reconstruct the secondary vertices from decaying particles, to track and identify
 1176 particles with momenta below 200 MeV and to compliment the momentum and
 1177 angle measurements of TPC. During long shutdown 2 in 2019-2020 the entire ITS
 1178 will be replaced [136]. As of 2018 the two innermost layers are made of the silicon
 1179 pixel detector (SPD). As it is the closest detector to the interaction point it requires
 1180 a very high spatial resolution. Thus the choice of pixel technology is natural. In
 1181 heavy ion collisions the particle density is around 50 particles per cm^2 .

1182 The next two layers together are the silicon drift detector (SDD). The layers
 1183 are made out of homogeneous neutron transmutation doped silicon, that is ionized
 1184 when a charged particle goes through the material. The generated charge then
 1185 drifts to the collection anodes, where it is measured. The maximum drift time
 1186 in SDD is about $5 \mu s$. This design gives very good multitrack capabilities and
 1187 provides two out of the four dE/dx samples in the ITS.

1188 The two remaining layers in the ITS are the silicon strip detector (SSD). The
 1189 strips work in a similar way as silicon pixels, but by itself one layer only provides
 1190 good resolution in one direction. Combining two crossing grids of strips provides 2
 1191 dimensional detection. Each charged particle will hit two intervening strips. The
 1192 position of the hit can be deduced from the place where the strips cross each other.

1193 **2.3.2 TPC**

1194 The time projection chamber (TPC) is a cylindrical detector filled with 88 m^3
1195 of Ne – CO₂ (90/10 %) gas mixture. The gas is contained in a field cage that
1196 provides an uniform electric field of 400 V/cm along the z-axis. Charged particles
1197 traversing through the TPC volume will ionise the gas along their path. This
1198 liberates electrons that drift towards the end plates of the cylinder. A schematic
1199 of the TPC is shown in Fig. 28.

1200 The field cage is separated into two detection volumes by the central high
1201 voltage electrode. Both sides have a drift length of 2.5 m and inner and outer
1202 diameters of 1.2 m and 5 m respectively. This means the central electrode must
1203 provide a maximum potential of 100 kV to achieve the design field magnitude. The
1204 maximum time required for electrons to drift through the chamber is about 90 μs .

1205 When electrons reach the end of the main cylinder they enter the readout
1206 chambers. The readout section of both sides consists of 18 outer chambers and
1207 18 inner chambers. Each of them is made of multiwire proportional chambers
1208 with cathode pad readouts. This design has been used in many TPCs before.
1209 During LS2 in 2019-2020, the multiwire chambers will be replaced by Gas Electron
1210 Multipliers (GEMs, see section 2.3.3).

1211 **2.3.3 TPC upgrade**

1212 During LS2 in 2019-2020 ALICE will go through significant modifications. The
1213 goal is to be able have continuous readout [137] in heavy ion collisions at an
1214 interaction rate of 50 kHz. ALICE will add a new Forward Interaction trigger
1215 (FIT) to replace the V0 and T0 detectors.

1216 Additionally the current inner tracking system (ITS) will be completely re-
1217 placed. The current layered structure with three different technologies will be
1218 replaced by an all pixel detector with significantly reduced pixel size. Additionally
1219 the first layer will be brought closer to the beam pipe. The new ITS will have
1220 better tracking efficiency and better impact parameter resolution.

1221 The muon detection will be complimented by the Muon Forward Tracker
1222 (MFT) [138]. Based on the same technology as the new ITS, MFT will be placed
1223 before the hadron absorber that sits in front of the existing muon spectrometer.
1224 MFT should significantly increase the signal/background ratio in heavy quark
1225 measurements.

1226 Many subdetectors will make small improvements to enhance the readout rate.
1227 The central trigger processor will be replaced and ALICE will introduce a new
1228 framework O^2 that combines both online data acquisition and offline analysis.

1229 The detector restricting the readout the most at the moment is the TPC.
1230 The current wire chamber based system limits the readout rate to 3.5 kHz. To

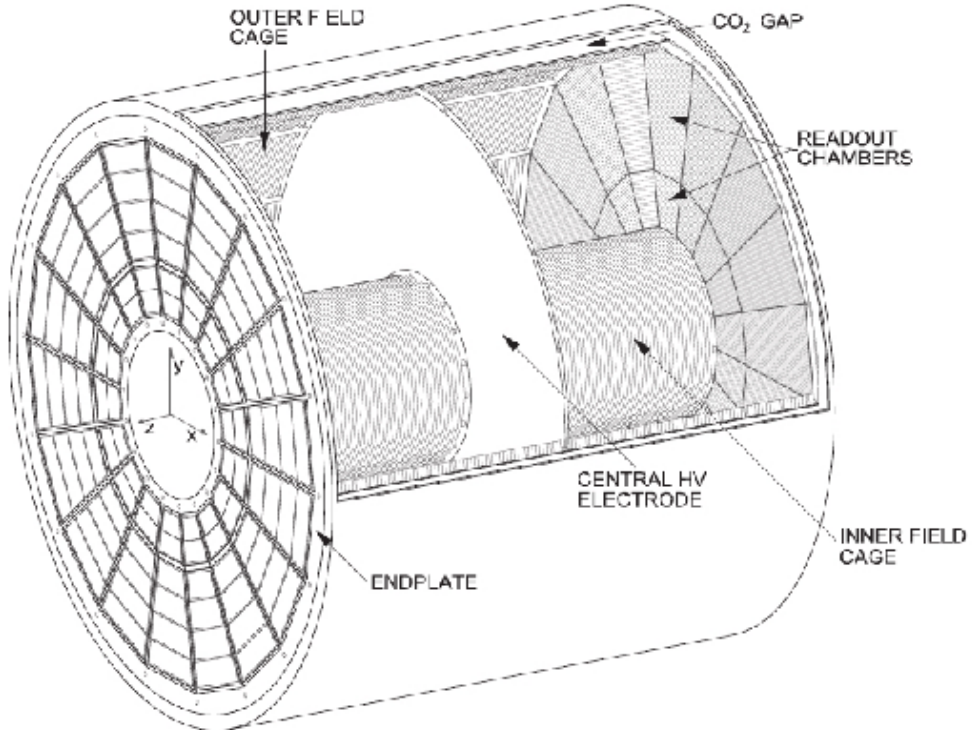


Figure 28: Schematic view of ALICE Time Projection Chamber

1231 achieve the 50 kHz readout rate goal the wire chambers will be replaced by a Gas
 1232 Electron Multiplier (GEM) based system. The GEMs are designed to minimise
 1233 ion backflow to allow continuous, ungated and untriggered readout. I have made
 1234 a personal contribution to the quality assurance of the new GEM readout of TPC.

1235 TPC has a total of 36 inner and 36 outer readout chambers. Each of these will
 1236 consist of 4 layers of GEM foils. The inner chambers will only have one foil for
 1237 each layer. The outer chambers are separated into three sections, each with its
 1238 own layer of foils. Each GEM foil is made up of a $50 \mu\text{m}$ thick resistive capton
 1239 layer, coated on both sides by $5\mu\text{m}$ thick layers of copper. Each foils is separated
 1240 into a number (20-24 depending on the size of the foil) of distinct active areas.
 1241 The active areas are pierced densely with holes. They have 50-100 holes in the
 1242 area of a single mm^2 . The density of holes changes from layer to layer. The two
 1243 middle layers of foils have a larger (double) pitch (smaller hole density) while the
 1244 top and bottom layers have a smaller (normal) pitch (larger hole density).

1245 The purpose of the multilayered structure is to reduce the ion backflow []; not
 1246 only one layer of GEM foils will be installed, but a 4 layer stack. In the stack there
 1247 are 2 standard pitch GEM foils, where the pitch size, i.e. the separation of the

holes inside a foil is around $140 \mu\text{m}$, and 2 large pitch GEM foils, there the hole spacing is two times larger, $280 \mu\text{m}$. The two outer layers will have standard pitch and the two middle layers have large pitch. The middle layers with large pitch serve as extra insulator against the ion backflow. Additionally the setup allows operating individual GEM foils at lower voltages and still have an increase in the gain of a few orders of magnitude. [139]

The holes have a conical shape which they acquire during a two step chemical etching process. The designed inner and outer diameters of the holes are $50 \pm 5 \mu\text{m}$ and $70 \pm 5 \mu\text{m}$ respectively. Fig. 29 shows the cross-section of a hole alongside with the operation principle of a GEM foil.

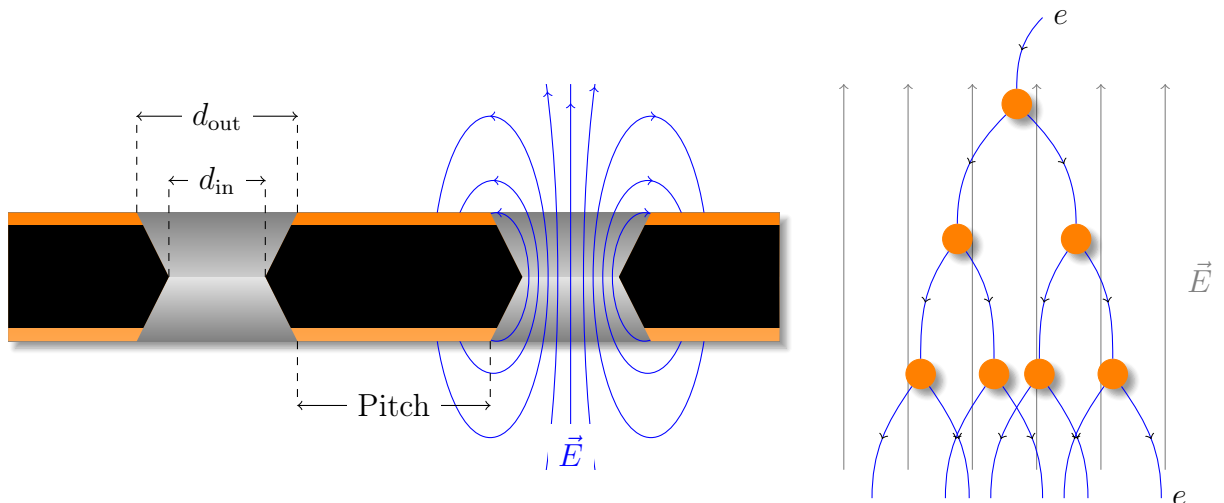


Figure 29: *left* Cross-section of a GEM foil. (Not to scale). The hole diameters are $d_{\text{in}} = 50 \pm 5 \mu\text{m}$ and $d_{\text{out}} = 70 \pm 5 \mu\text{m}$ and pitch is either 140 or $280 \mu\text{m}$. *right* The amplification of a GEM foil is based on the Townsend avalanche phenomenon. Electrons entering the electric field inside the hole are accelerated. If they gain enough energy before colliding with atoms they can liberate additional electrons, which are further accelerated leading to a chain reaction.

The working principle of these foils is based on the Townsend avalanche phenomenon, which is also used in proportional counters such as Geiger counters. There is a large potential difference (140-400 V) applied to the two sides of the foil, which results in large field in each hole. Electrons gain energy in the field and if the electric field is strong enough, the free electron can gain sufficient velocity (energy) to liberate another electron when it next collides with a molecule. The two free electrons then travel towards the anode and gain sufficient energy from the electric field to cause further impact ionisations, and so on leading to a chain reaction. Under the right conditions a single electron entering any hole will create

1267 an avalanche containing 100–1000 electrons; this is the gain of the GEM foil.

1268 As opposed to wire chambers, which typically have one voltage setting, a GEM-
1269 based detector requires several independent voltage settings: there is a drift voltage
1270 which drives the electrons from the ionisation point to the GEM, an amplification
1271 voltage, and an extraction voltage that brings electrons from the GEM exit to the
1272 readout plane. In a multilayer system this is further complicated by the voltages
1273 between layers of foils.

1274 Quality Assurance of the GEM foils

1275 The GEM foils are produced at CERN, where they will undergo a basic QA (QA-B)
1276 procedure, that includes a coarse optical inspection for any large defects ($\gtrsim 1\text{ mm}$)
1277 and a short term high voltage measurement. Afterwards the foils are sent for
1278 an advanced quality assurance (QA-A) procedure which is performed in one of
1279 the two QA-A centers, one in the Helsinki Institute of Physics (HIP) and one in
1280 the Wigner Research Centre in Budapest. Details of the QA-A procedure can be
1281 found in the thesis of Márton Vargyas [140] and in [?]. In the QA-A centers all foils
1282 are put through a detailed optical scanning process and a long term high voltage
1283 measurement. I was personally performing the QA production in Helsinki for the
1284 final 6 months of the project.

1285 The optical scan is performed with the help of a scanning robot. The setup
1286 along with most of the software was developed at the Detector Laboratory of the
1287 Helsinki Institute of Physics [?]. The optical scan is able to distinguish every
1288 single hole on the GEM foil and measure their properties. The purpose of the
1289 scan is two-fold; to catch defects that could affect the performance and classify the
1290 foils based on their hole parameters. It is expected that these are connected with
1291 the foil's electric properties [?]. For example, smaller holes create more intense
1292 and focused fields, which would result in larger amplification of their avalanche
1293 electrons, i.e. the local gain is expected to be larger.

1294 After the optical scanning, the foils are subjected to a long term (5-12 hours)
1295 high voltage leakage current measurement. Each segment of the GEM foil is con-
1296 nected to a high voltage of 500 V and the leakage current is measured separately
1297 for each segment. The accepted leakage current in each segment is 0.16 nA.

1298 Foils that fail the criteria are either trashed or sent to CERN for recleaning or
1299 repairing, after which they will go through the QA pipeline again.

1300 Additionally some foils will be put through a gain mapping procedure. As it is
1301 time consuming can only be performed in the QA-A center in Budapest it is only
1302 a small subset of foils. However, by measuring the gain in some foils the gain can
1303 be correlated with foil properties. Thus the single foil gain can be predicted based
1304 on the results of the optical scan. Details can be found in [140].

1305 **2.3.4 Particle identification**

1306 One guiding principle in the design of ALICE was to achieve good particle iden-
1307 tification (PID) over a large part of phases space and for several different particle
1308 types. In ALICE there are several detectors taking part in the identification of
1309 particles.

1310 One of the particle identification detectors is the transition radiation detector
1311 (TRD) [141]. Its main task is identifying electors with momenta larger than 1 GeV.
1312 Transition radiation is produced when highly relativistic particles traverse the
1313 boundary between two media having different dielectric constants. The average
1314 energy of the emitted photon is approximately proportional to the Lorentz factor γ
1315 of the particle, which provides an excellent way of discriminating between electrons
1316 and pion. ALICE TRD is made of a composite layer of foam and fibres. The
1317 emitted photons are then measured in six layers of Xe/CO₂ filled time expansion
1318 wire chambers.

1319 The time of flight (TOF) detector [142] uses a very simple physics principle,
1320 i.e. calculating the velocity of the particle using the time of flight between two
1321 points. Combining this with the momentum of particle, obtained from the tracking
1322 detectors, one can calculate the mass of the particle, which identifies particles. The
1323 TOF detector consists of multigap resistive wire chambers. These are stacks of
1324 resistive plates spaced equally. They allow time of flight measurements in large
1325 acceptance with high efficiency and with a resolution better than 100 ps.

1326 The third specific particle identification detector is the high momentum particle
1327 identification (HMPID) detector [143]. The HMPID uses a ring imaging Cherenkov
1328 counter to identify particles with momenta larger than 1 GeV. Particles moving
1329 through a material faster than the speed of light in the material will produce
1330 Cherenkov radiation. The velocity of the particle determines the angle at which
1331 the radiation is emitted. Measuring this angle gives the velocity of the particle.
1332 This can be again used to calculate the mass of the particle, if the momentum is
1333 known. In HMPID the material is a liquid radiator and the photons are measured
1334 with multiwire proportional chambers in conjunction with photocathodes.

1335 In addition to the specific particle identification detectors, the general purpose
1336 tracking detectors can be used for identification through the use of specific energy
1337 loss of charged particles traversing through a medium and the transition radiation
1338 emitted by charged particles when crossing the boundary between two materials.

1339 dE/dx measurements are provided by the last four layers of the ITS detector,
1340 i.e. the SDD and the SSD, thanks to their analog readout [144]. ITS can provide
1341 particle identification in the low p_T region, up to 1 GeV, and pions reconstructed in
1342 the standalone mode can be identified down to 100 MeV. Similar to ITS the TPC
1343 detector provides specific energy loss measurements. TPC can identify charged
1344 hadrons up to p_T 1 – 2 GeV as well as light nuclei, He3 and He4.

1345 **2.3.5 Electromagnetic Calorimeter**

1346 Calorimeters are designed to measure the energy of particles. Electromagnetic
1347 calorimeters specialise in detecting particles that interact primarily through the
1348 electromagnetic interaction, namely photons and electrons. They are required in
1349 many neutral meson and direct photon analyses. In addition the energy informa-
1350 tion enhance jet measurements.

1351 ALICE has two electromagnetic calorimeters, the photon spectrometer
1352 (PHOS) [145] and the electromagnetic calorimeter (EMCal) [146]. PHOS is a
1353 homogeneous calorimeter that consists of scintillating PbWO_4 crystals, which
1354 generate a bremsstrahlung shower and produce scintillation light. The energy of
1355 the particle determines the amount of light produced. To improve the charged
1356 particle rejection, PHOS includes a charged particle veto detector (CPV) [?].
1357 PHOS is built to have a very fine granularity, making it well suited for measuring
1358 direct photons and neutral mesons.

1359 In comparison to PHOS, EMCal has coarser granularity, but a significantly
1360 larger acceptance, making it suitable for jet physics. The acceptance of EMCal in
1361 the azimuthal angle is $80 \text{ deg} < \phi < 187 \text{ deg}$. During long shutdown 1 in 2013-
1362 2015, EMCal was extended with the di-jet calorimeter (DCal) [147], giving an
1363 additional acceptance region of $260 \text{ deg} < \phi < 320 \text{ deg}$. This provides partial
1364 back-to-back coverage.

1365 EMcal is segmented into 10 full size super modules (SM), 5 for A side and 5 for
1366 C side, and two 1/3 sized SMs, one for each side. This segmentation can be seen
1367 in Fig. 30. Each SM is divided into 24 strips, each covering full η (24 towers) and
1368 2 towers in η . Each strip is composed of 2×2 tower modules. Thus each full size
1369 super module includes 1152 towers and in total the EMCal is made up of 12288
1370 towers.

1371 The build of individual towers is shown in Fig. 31. Each tower is built up from
1372 76 alternating layers of 1.44 mm Pb and 77 layers of 1.76 mm polystyrene base
1373 injection moulded scintillator. The lead tiles produce the shower and scintillator
1374 tiles the light. Each tower scintillator is equipped with reflectors on all sides
1375 to provide better gain and keep the four towers inside one module isolated. The
1376 scintillation photons produced in the active volume of the tower are collected by 36
1377 longitudinally placed wave length shifting light guide fibres. The light is eventually
1378 directed to the Avalanche Photo Diodes (APD) for readout.

1379 **2.3.6 Forward and trigger detectors**

1380 ALICE includes a few small and specialised detectors of importance. The event
1381 time is determined with very good precision ($< 25 \text{ ns}$) by the T0 detector [148].
1382 T0 consists of two sets of Cherenkov counters that are mounted around the beam

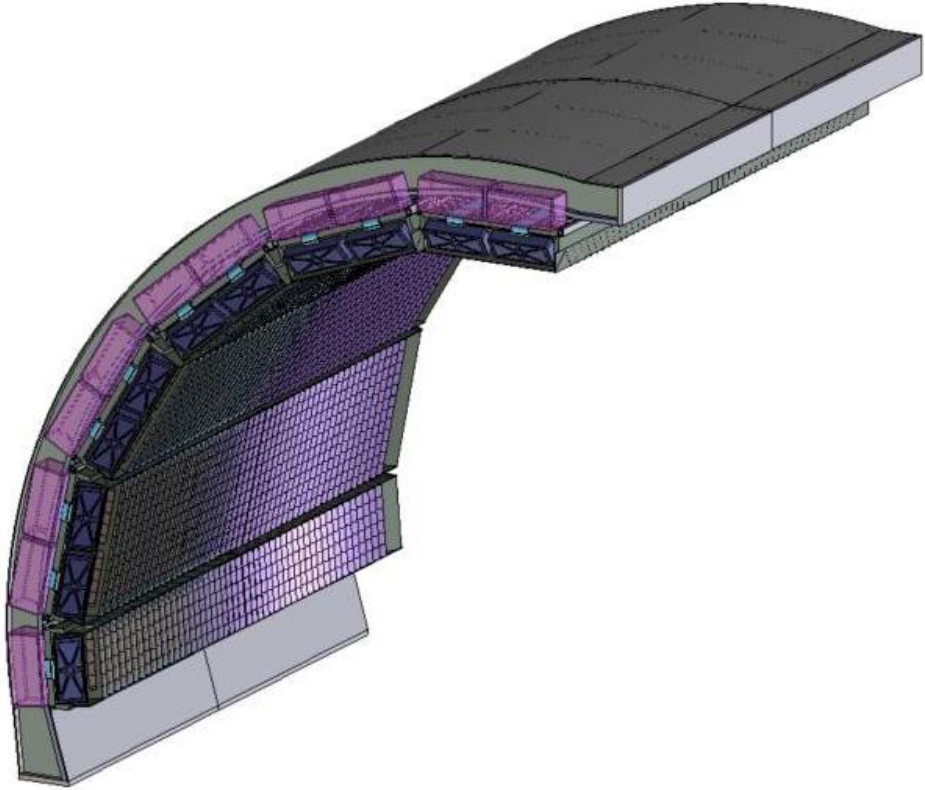


Figure 30: The EMCal detector arc, where the segmentation into 10 full size and 2 $\frac{1}{3}$ -sized (5 and 1 per side) supermodules can be seen.

1383 pipe on both sides of the interaction point. T0 gives the luminosity measurement
1384 in ALICE.

1385 Another small detector in the forward direction is the V0 detector [148]. This
1386 consists of two arrays of segmented scintillator counters located at $-3.7 < \eta <$
1387 -1.7 and $2.8 < \eta < 5.1$. V0 is used as a minimum bias trigger and for rejection
1388 of beam-gas background. Particle multiplicity in the forward direction can be
1389 related to the event centrality. Thus V0 is the main detector used in centrality
1390 determination in PbPb collisions.

1391 The multiplicity measurement of V0 is complimented by the forward multiplicity
1392 detector (FMD) [148]. FMD includes five rings of silicon strip detectors that
1393 make up the FMD. FMD gives acceptance in the range $-3.4 < \eta < -1.7$ and
1394 $1.7 < \eta < 5.0$.

1395 During long shutdown 2 in 2019-2020, V0 and T0 will be replaced by the Fast
1396 Interaction Trigger (FIT) detector [149]. For historical reasons elements of FIT are
1397 also referred to as V0+ and T0+. FIT will allow centrality, event plane, luminosity

THE EMCAL Module Components

Containment: 88 parts

- 1) Back (holes: 144 thru for fibers + springs + mech. support), 1
- 2) Compression (holes: 144 thru for fibers + springs), 1
- 3) Front Plate (holes: 144 thru for fibers + springs + mech. support), 1
- 4) 5) Plungers (10)
- 6) Belleville washers (75)

Tensioning and Insulation:

40 parts

- 7) Stainless steel straps (4)
- 8) Screws (24)
- 9) Flanges (8)
- 10) Light tight stickers (4)

Sandwich:

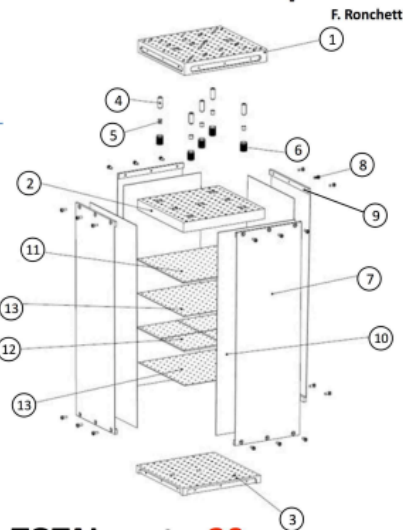
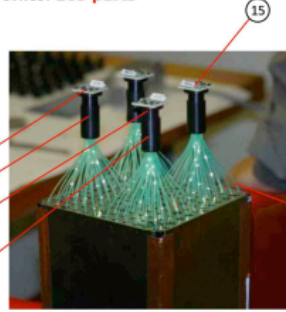
538 parts

- 11) Lead tiles (76)
- 12) Scintillator tiles (308)
- 13) Bond paper sheets (154)

Readout and Electronics:

165 parts

- 14) WLS fibers (144)
- 15) APD (4)
- 16) CSP (4)
- 17) Light guides (4)
- 18) Mount (4)
- 19) Collars (4)
- 20) Diffuser (1)



TOTAL parts: 20

TOTAL components: 831

Plus cabling, GMS and mech. supports

Figure 31: The exploded EMCAL tower view

1398 and interaction time determination in the continuous readout mode, that ALICE
1399 will operate in after 2020.

1400 For photon multiplicity measurement ALICE has the photon multiplicity de-
1401 tector (PMD) [150]. PMD uses two planes of gas proportional counters with a
1402 cellular honeycomb structure. PMD gives the multiplicity and spatial distribution
1403 of photons in the region $2.3 < \eta < 3.7$.

1404 On top of the ALICE magnet there is an array of 60 large scintillators called
1405 the ALICE cosmic ray detector (ACORDE) [151]. ACORDE is used as a trigger
1406 for cosmic rays for calibration and alignment.

1407 The only hadronic calorimeters in ALICE are the zero degree calorimeters
1408 (ZDC) [152], which are located next to the beam pipe in the machine tunnel
1409 about 116 m from the interaction point. There are two sets of calorimeters. One
1410 is made of tungsten, specialising in measuring neutrons, while the other, made of
1411 brass, is specialised in measuring protons. ZDC is meant to detect spectators, i.e.
1412 parts of the colliding ions that do not take part in the interaction. If there are
1413 more spectators, the collisions is likely to be more peripheral. Thus ZDC gives
1414 information about the centrality of the event especially in proton-lead collisions [1],
1415 but also in Pb-Pb collisions [?].

1416 A new detector installed during the long shutdown 1 is the ALICE diffractive
1417 detector (AD) [?]. AD consists of two assemblies, one in each side of the interaction
1418 point, both made of two layers of scintillators. These assemblies are situated about
1419 17 m and 19.5 m away from the interaction points. The pseudorapidity coverage is
1420 $-6.96 < \eta < -4.92$ and $4.78 < \eta < 6.31$. AD greatly enhances ALICE's capability
1421 for diffractive physics measurements that require a large pseudorapidity gap.

1422 2.3.7 Muon spectrometer

1423 Outside the main magnet, ALICE has a spectrometer dedicated to measuring
1424 muons [153]. In heavy ion physics muons are mainly used to measure the produc-
1425 tion of the heavy quark resonances J/ψ , Ψ' , Υ , Υ' and Υ'' .

1426 The muon spectrometer consists of three parts, the absorber, the muon tracker
1427 and the muon trigger. The absorber is meant to remove the hadronic background
1428 as efficiently as possible. After the absorber there are ten plates of thin cathode
1429 strip tracking stations with high granularity, the muon tracker. After the muon
1430 tracker there is a layer of iron to filter out any remaining particles, other than
1431 muons. The muon trigger is located behind this layer. The trigger consists of four
1432 resistive plate chambers.

1433 2.3.8 Triggers

1434 High energy physics experiments need triggers to select interesting physics. Ex-
1435 periments such as CMS and ATLAS at CERN look for extremely rare events with
1436 up to 40 million events each second. Such amounts can't be recorded real-time as
1437 many detectors require some time for the readout, up to 1 ms/event in ALICE.
1438 Thus one uses triggers, i.e. a set of very fast hardware based decisions on which
1439 events are to be saved. Additionally one needs some confirmation that an event
1440 has even occurred to tell other detectors that the event needs to be recorded.

1441 For ALICE the target event rates are 1 MHz for ppcollisions, 0.1-2 kHz for
1442 Pb–Pbcollisions and 200 kHz for the 2013 p–Pbcollisions.

1443 At ALICE the main system responsible for the trigger decisions is the AL-
1444 ICE Central Trigger Processor (CTP) [?]. The CTP generates three levels of
1445 hierarchical hardware triggers - Level 0, Level 1 and Level 2, (L0, L1 and L2 re-
1446 spectively) before an event is accepted and transmitted to the Data Acquisition
1447 system (DAQ). Afterwards additional software assessments are performed by the
1448 High Level Trigger (HLT).

1449 Triggers can be roughly put into two classes, minimum bias triggers that make
1450 sure no empty events are recorded, and rare triggers that require specific signatures
1451 in ALICE detectors, such as large energy deposits in EMCAL or two muons in the
1452 muon arm acceptance.

1453 **Minimum bias trigger**

1454 Several of the ALICE detectors are used to make the initial minimum bias trigger
1455 decisions. These include the SPD layers of ITS, V0 and T0. SPD can count the
1456 number of hits in the first two layers of ITS. Minimum bias ppcollisions typically
1457 require at least one hit in either SPD or V0A/V0C. Similarly Pb–Pbtriggers look
1458 at both V0 and SPD hits. The p–Pbdata has been mainly triggered using V0
1459 information.

1460 **EMCal trigger**

1461 In addition to the minimum bias triggers, the most relevant trigger for this thesis
1462 is the EMCal trigger. Much of the EMCal trigger has been developed at the
1463 University of Jyväskylä. Extensive details of the trigger and the development
1464 work can be found in the thesis of Jiří Král [154]. Personally I have spent time at
1465 CERN helping in the maintenance of the level 0 trigger.

1466 ALICE EMCal provides two levels of trigger signal, L0 and L1, which allows
1467 triggering on either single shower deposits or integrated energy deposits in larger
1468 ares, i.e. jets [155].

1469 As inputs the trigger gets exclusive sets of 2×2 EMCal towers, to limit the
1470 number of channels that need to be processed. The L0 trigger then checks for
1471 energy deposits within a rolling window of 2×2 trigger channels (4×4 towers).
1472 Areas of 4×4 towers most probably will contain only a single shower. (or two
1473 adjacent showers coming from a single decayed π^0) Thus the trigger is called the
1474 single shower trigger.

1475 For L0 the trigger decision is done in Trigger Region Units (TRU) that each
1476 cover 4×42 channels (8×48 towers). The amplitude from the sliding window
1477 is compared to a constant threshold. Additionally a peak finding algorithm is
1478 implemented to define correctly the time of the signal maximum. A single bit OR
1479 decision of all individual TRUs is forwarded to the CTP as the EMCal L0 trigger
1480 decision.

1481 The L0 information is additionally forwarded to the Level 1 trigger, which
1482 recomputes similar 2×2 channel decisions to produce the single shower trigger,
1483 but L1 can perform the calculation also on the borders between trigger units. In
1484 addition the L1 trigger can check for energy deposits inside a larger 16×16 channel
1485 (32×32 towers) window, which is considered to be the jet trigger.

1486 The L1 trigger can compare up to two thresholds for each single shower and
1487 jet trigger. There is a dedicated link in between the V0 detector and EMCal STU,
1488 which can provide centrality information that is used to compute a dynamical
1489 threshold as a function of the V0 multiplicity.

1490 The trigger subsystem provides both the L0 and L1 decisions to the CTP and

₁₄₉₁ DAQ.

1492 3 Event and track selection

1493 The $\sqrt{s_{\text{NN}}} = 5.02$ TeV p–Pb ($1.3 \cdot 10^8$ events, $\mathcal{L}_{\text{int}} = 620 \text{ nb}^{-1}$) collisions were
1494 recorded in 2013 by the ALICE detector [156]. The details of the performance of
1495 the ALICE detector during LHC Run 1 (2009–2013) are presented in Ref. [157].

1496 3.1 Event selection

1497 This analysis uses both a minimum bias trigger and an EMCal based trigger to
1498 select the analysed events. For the 2013 p–Pb collisions minimum bias events are
1499 required to have signals in both V0A and V0C. This condition is used later offline
1500 to reduce the contamination of the data sample from beam-gas events by using
1501 the timing difference of the signal between the two stations [157].

1502 EMCal is also used to provide the jet trigger used in triggered datasets. EMCal
1503 can be used to trigger on single shower deposits or energy deposits integrated over
1504 a larger area. Latter case is used for jet triggers. The EMCal trigger definition in
1505 the 2013 p–Pb collisions requires an energy deposit of either 10 GeV for the low
1506 threshold trigger or 20 GeV for the high threshold trigger in a 32×32 patch size.

1507 The EMCal

1508 Triggers, V0 and EMCal are discussed in more detail in sections 2.3.6, 2.3.8
1509 and 2.3.5.

1510 3.2 Track selection

1511 The analysis uses charged tracks that are reconstructed with the Inner Tracking
1512 System (ITS) [158] and the Time Projection Chamber (TPC) [159]. These are
1513 discussed in sections 2.3.1 and 2.3.2. A detailed overview of track reconstruction
1514 in ALICE can be found from [157].

1515 The main reconstruction of tracks starts in TPC. There are 159 tangential
1516 pad rows in the TPC readout chambers. The track reconstruction starts from the
1517 outermost layer and the clusters are paired with clusters in the next layer inwards,
1518 taking into account a proximity cut. When this track finding procedure hits the
1519 innermost pad row in TPC, this information is used as an initial seed for the track
1520 finding in ITS. Similar procedure of pairing adjacent layers with a proximity cut
1521 is repeated in ITS.

1522 After the reconstruction of tracks in ITS is completed, all the tracks are ex-
1523 trapolated to their point of closest approach to the preliminary interaction vertex.
1524 Then the second track fitting step begins, this time starting from the interaction
1525 point and proceeding outwards. A Kalman filter [160] technique is used to do
1526 the new fit using the clusters found in the previous stage. This time the tracks
1527 are matched also to the other detectors in the central barrel beyond TPC. When

1528 this step is complete, a final refit from the outermost TPC pad rows towards the
1529 interaction point is performed. The final track parameters come from this refit.

1530 With the final track parameters the primary vertex can be determined with
1531 better accuracy than with only SPD information. The tracks are extrapolated to
1532 the nominal beam line and a weighted average of the points of closest approach
1533 determines the accurate primary vertex position.

1534 The final step of the track reconstruction is the determination of the secondary
1535 vertices. For this, all the tracks whose distance of closest approach (DCA) to
1536 the primary vertex is larger than a defined minimum value (?? mm in p–Pb) are
1537 selected. For these tracks, points of closest approaches are determined for pairs of
1538 tracks. If the tracks are sufficiently close to each other and show characteristics of
1539 short lived particle decays, these points are identified as secondary vertices.

1540 Combining the information from the ITS and the TPC provides a resolution
1541 ranging from 1 to 10 % for charged particles with momenta from 0.15 to 100 GeV/c.
1542 For tracks without the ITS information, the momentum resolution is comparable
1543 to that of ITS+TPC tracks below transverse momentum $p_T = 10$ GeV/c, but for
1544 higher momenta the resolution reaches 20 % at $p_T = 50$ GeV/c [157, 161].

1545 In p–Pb collisions the tracks are selected following the hybrid approach [162]
1546 which ensures a uniform distribution of tracks as a function of azimuthal angle
1547 (φ). The parameters in the approach are summarised in table 3.

1548 The first requirements are on the quality of the track fit in ITS and TPC.
1549 The ITS requirement only removes tracks that are clear outliers. For TPC the
1550 requirement is much more strict. For step 1 it is required that a track has 3 out of
1551 the 6 possible hits in ITS, one of which must be in SPD. In step 2 this is replaced
1552 by an additional vertex constraint, where the primary vertex itself is added as a
1553 point to the track to improve the momentum resolution.

1554 For the TPC, 70 crossed pad rows out of the maximum 159 is required. This
1555 measures the effective track length inside the TPC. This takes into account the
1556 possibility of having pad rows missing in the middle of the track due to charge in
1557 these clusters being below the threshold for some reason. Additionally it is required
1558 that the ratio between crossed rows and findable clusters is at least 0.8. Findable
1559 clusters are defined as the number of geometrically possible clusters which can be
1560 assigned to a track, taking into account dead zones due to chamber boundaries
1561 and limited η -acceptance. For both steps of the hybrid cut is is required that the
1562 fraction of clusters shared with several tracks is less than 40%.

1563 The remaining cuts are meant to make sure that the measured tracks are
1564 really produced in the primary collision. A track might gain a kink due to a
1565 particle scattering decay. After this, it is no longer describing the properties of the
1566 primary collisions. The particle after such a kink, a kink daughter, is rejected in
1567 the cuts. The final cuts are on the distance of closest approach (DCA) of the track

Table 3: Parameters in the hybrid track cut

Track Cut	Step 1	Step 2
χ^2 / ITS cluster	< 36	< 36
χ^2 / ITS cluster	< 4	< 4
Hits in ITS	3	0
ITS hit requirements	1 in SPD	No requirement
Vertex constraint	No	Yes
Number of crossed rows in TPC	70	70
TPC crossed rows over findable clusters	> 0.8	> 0.8
Fraction of shared TPC clusters	< 0.4	< 0.4
Kink daughters	Rejected	Rejected
DCA _{xy}	< 3.2 cm	< 3.2 cm
DCA _z	< 2.4 cm	< 2.4 cm
Other		Rejected by step 1

1568 to primary vertex. To have confidence that the track comes from the primary
 1569 collision, the track must be close enough to the primary vertex. The cuts are
 1570 different for the distance along (DCA_z) and perpendicular to (DCA_{xy}) the beam
 1571 axis.

1572 The momentum resolutions of the two classes of particles are comparable up
 1573 to $p_T \approx 10 \text{ GeV}/c$, but after that, tracks without ITS requirements have a worse
 1574 resolution [157, 161].

1575 3.3 Cluster selection

1576 **Extend cluster reconstruction** Neutral particles used in jet reconstruction are re-
 1577 constructed by the Electromagnetic Calorimeter (EMCal [146]). The EMCal covers
 1578 an area with a range of $|\eta| < 0.7$ in pseudorapidity and 100 deg in azimuth. EMCal
 1579 is complimented with the Dijet Calorimeter (DCal) [147] and Photon Spectrom-
 1580 eter (PHOS) [145] that are situated opposite of the EMCal in azimuth. PHOS
 1581 covers 70 degrees in azimuth and $|\eta| < 0.12$. The DCal is technologically identical
 1582 to EMCal. The DCal coverage spans over 67 degrees in azimuth, but in pseudo-
 1583 rapidity the mid region is occupied by the PHOS. In between PHOS and DCal
 1584 active volumes, there is a gap of 10 cm. DCal is fully back-to-back with EMCal.

1585 The clusters used in the analysis were obtained from EMCal by the v2 clus-
 1586 teriser. Clusters matched to charged tracks are removed from the analysis as well
 1587 as clusters being identified as fake. The parameters used in the clusteriser are
 1588 summarised in table 4

1589 The clusteriser searches for a tower with energy deposit greater than a defined
 1590 seed energy and merges all surrounding (sharing a side) towers with energy deposit

higher than a defined threshold. In the next step all towers sharing a side with
 already included towers are added, again requiring that the energy deposits exceeds
 the threshold. The algorithm can identify local minima and halts the clustering
 in case that the neighbouring tower energy is higher. Already clustered towers are
 removed from the pool, so one tower can only be clustered once.

Highly energetic calorimeter hits should spread into several towers as the elec-
 tromagnetic shower evolves. However, some clusters with high energy have their
 energy located in a single tower. These are believed to come from slow neutron
 hitting the APD readout of the towers. These are called exotic clusters. The
 measure of exoticity is denoted as

$$1 - \frac{E_{\text{cross}}}{E_{\text{max}}}, \quad (36)$$

where E_{max} is the energy in the most energetic tower and E_{cross} is the sum of
 the four towers neighbouring the most energetic one. The closer to 1, the more
 exotic the cluster is and the more probability that it is fake. Cut of 0.97 has been
 adopted as default for EMCal analyses, including this one.

A method of matching the cluster position to TPC track extrapolation is used
 to suppress charged hadron contribution to hits in EMCal. Tracks identified by the
 tracking detectors are extrapolated close to the EMCal surface, where the closest
 cluster is found and the track extrapolation is continued until reaching the same
 depth as the cluster. The remaining distance in between the extrapolated track
 and the cluster is then used to reject hadronic hits.

Table 4: Parameters used in the EMCal clusteriser

Setting	Value	Description
Clusteriser seed	0.2 MeV	
Clusteriser cutoff	0.05 MeV	
Cells in cluster	> 1	
Track matching radius	0.025	
Fiducial cut	1 tower	
Exotic cut	0.97	
Minimal cluster Energy	0.3 GeV	

4 Analysis method

4.1 Jet Finding

The analysis uses reconstructed jets as estimates of the original parton. Essentially
 when reconstructing jets, nearby tracks are combined into jets. Collisions between

hadrons are never as clean as electron-electron collisions. Even for a proton-proton collision there are participant partons, that will produce a soft background in addition to the hard scattering products. Jet reconstruction must deal with this soft background. The reconstruction is never perfect, one can have uncorrelated tracks that get included in the jet and some tracks originating from the parton are missed by the reconstruction. There are several methods to perform the reconstruction, all of which require some kind of size parameter, which cuts out jet participants too far from the jet axis. The tracks that are grouped into a jet are referred to as jet constituents.

The analysis is performed by analysing jet constituents. In each collision event, the jets are reconstructed using FastJet [163] with the anti- k_T algorithm [164]. Jets for $R=0.4$ are selected in $|\eta| < 0.25$ to satisfy the fiducial acceptance of the EMCAL. In jet reconstruction both charged tracks with $p_T > 0.15 \text{ GeV}/c$ and neutral clusters with $p_T > 0.30 \text{ GeV}/c$ are considered. In the analysis, results are presented in terms of the jet transverse momentum $p_{T\text{jet}}$.

4.1.1 Anti k_T algorithm

Jets are reconstructed using the anti- k_T algorithm [164]. The algorithm works by trying to undo the splittings through combining protojets. The algorithm creates a list of protojets. At the beginning the list is populated by converting each track in the event into a protojet. Then the algorithm proceeds by combining these protojets. A simplified picture of the process for a limited number of tracks is shown in Fig. 32

The algorithm calculates distance measures for each individual protojet and for each possible pair of protojets. For individual protojets this depends only on the transverse momentum of the track.

$$k_{Ti}^2 = p_{Ti}^{2p} \quad (37)$$

For each pair of protojets the distance measure is calculated as

$$k_{Ti,j}^2 = \min(p_{Ti}^{2p}, p_{Tj}^{2p}) \frac{\Delta R_{i,j}^2}{D^2}, \quad (38)$$

where

$$R_{i,j} = (\phi_i - \phi_j)^2 + (y_i - y_j)^2. \quad (39)$$

If k_{Ti} is the smallest quantity then the protojet is a jet and it is removed from further consideration. If $k_{Ti,j}$ is the smallest quantity the two protojets are merged. This is iterated until no protojets are left.

The choice of the power p in the distance measure depends on the algorithm used

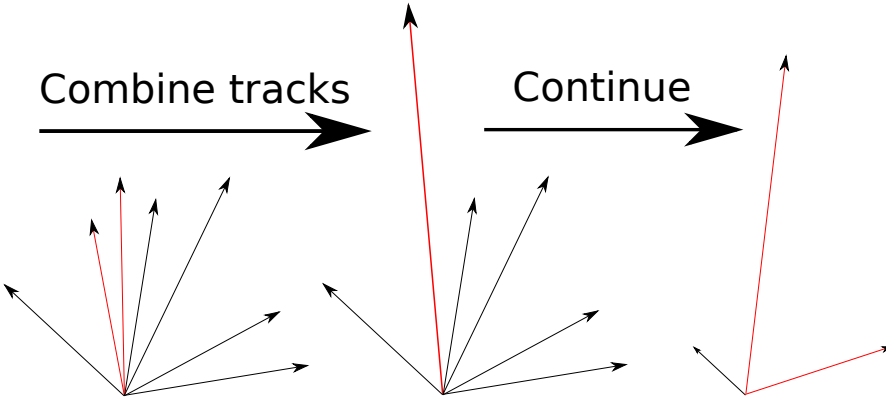


Figure 32: A simple example of the antil- k_{T} algorithm in progress. The red tracks in the leftmost figure are identified to have the smallest $k_{T,i}$ in the event and are combined into the red track of the middle figure. As this continues the remaining tracks are added to this or other jets. One track was deemed to be isolated enough to be counted as a protojet by itself. Note that the rightmost figure is zoomed out.

- 1647 • $p = 1$: k_{T} algorithm
- 1648 • $p = 0$: Cambridge Aachen algorithm
- 1649 • $p = -1$: anti- k_{T} algorithm

1650 With the choice $p = -1$ in anti- k_{T} algorithm, the softest splittings are un-
1651 done first. One consequence of the power choice in the anti- k_{T} algorithm is that
1652 reconstructed jets have a shape close to circular.

1653 4.2 Definition of j_{T}

1654 The jet fragmentation transverse momentum, j_{T} , is defined as the component of
1655 the constituent particle momentum, \vec{p}_{a} , transverse to the jet momentum, \vec{p}_{jet} . The
1656 resulting \vec{j}_{T} is illustrated in Fig. 33. The length of the \vec{j}_{T} vector is

$$j_{\text{T}} = \frac{|\vec{p}_{\text{jet}} \times \vec{p}_{\text{track}}|}{|\vec{p}_{\text{jet}}|}. \quad (40)$$

1657 It is commonly interpreted as a transverse kick with respect to the initial hard
1658 parton momentum that is given to a fragmenting particle during the fragmentation
1659 process, which is a measure of the momentum spread of the jet fragments [].

1660 The reconstructed jet axis is used for j_{T} reference. Any charged track within
1661 a fixed cone with radius R is taken as a jet constituent, as opposed to using the

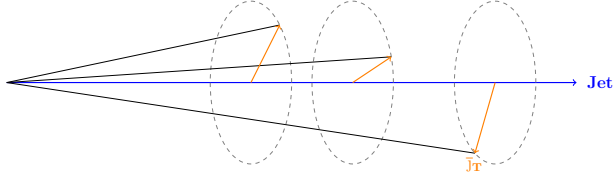


Figure 33: Illustration of \vec{j}_T . The jet fragmentation transverse momentum, \vec{j}_T , is defined as the transverse momentum component of the track momentum, \vec{p}_{track} , with respect to the jet momentum, \vec{p}_{jet} .

constituent list provided by the jet algorithm. Anti- k_T produces jets that are very circular in shape. Thus this doesn't change the constituent list considerably.

Neutral tracks are used only in jet reconstruction.

j_T results are shown as

$$\frac{1}{j_T} \frac{dN}{dj_T} \quad (41)$$

distributions. The logic behind this is that j_T is inherently a two-dimensional observable, comprised of j_{Tx} and j_{Ty} components. So the actual physical observable would be

$$\frac{d^2N}{d j_{Tx} d j_{Ty}} \quad (42)$$

Changing into polar coordinates with $j_{Tr} = j_T$ and θ gives

$$\frac{d^2N}{j_T dj_T d\theta}, \quad (43)$$

where j_T over the azimuth θ should stay constant and it can be integrated over, which gives

$$\frac{1}{2\pi} \frac{dN}{j_T dj_T}. \quad (44)$$

Results of the raw inclusive j_T distribution in four $p_{T,\text{jet}}$ bins with background are shown in figure 34. Background is further discussed in Sec. 4.4

4.3 Unfolding detector effects

The raw inclusive j_T distributions are corrected for the detector inefficiency using the unfolding method. The response matrix for the unfolding is obtained from a PYTHIA [165] simulation.

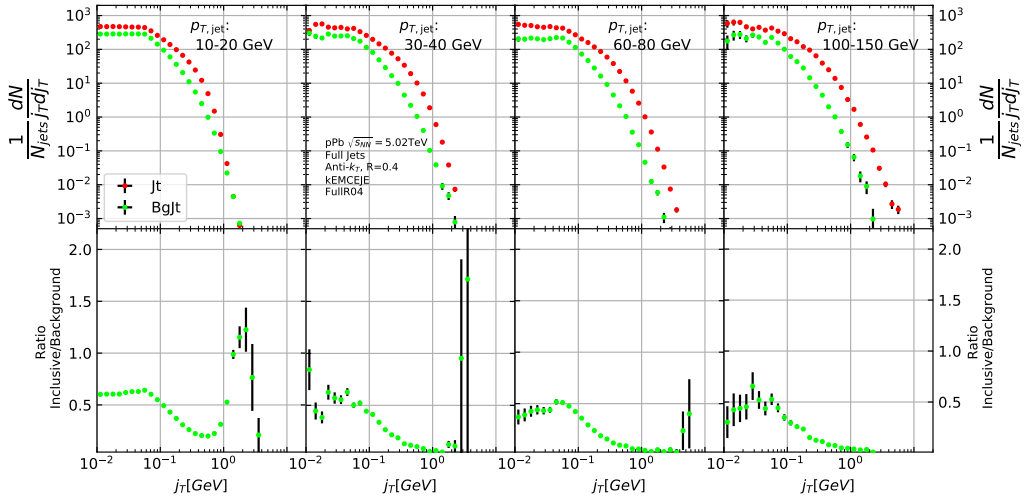


Figure 34: Inclusive j_T with background

Measured distributions are affected by two main factors; Limited acceptance -
The probability to observe a given event is less than one and limited resolution -
Quantity x cannot be determined exactly, but there is a measurement error. True
 $f(x)$ and measured $g(y)$ distributions are connected by a convolution integral.
Including statistical fluctuations this becomes

$$\hat{g}(y) = \int_a^b A(y, x) f(x) dx + \epsilon(y), \quad (45)$$

where A is the detector response obtained by (for example) Monte Carlo simulations and $\epsilon(y)$ is the term coming from statistical fluctuations. If x and y are discrete variables we have

$$\hat{g}_i = \sum_{j=1}^m A_{ij} f_j + \epsilon_i, \quad (46)$$

Or in matrix form

$$\hat{g} = Af + \epsilon \quad (47)$$

If the only detector effect is limited acceptance, A is a diagonal matrix. In a general discrete case the (naive) solution is obtained by the inverse matrix

$$\hat{f} = A^{-1} \hat{g} \quad (48)$$

However this usually leads to oscillating solutions and determining the inverse matrix can be difficult.

Two common methods to perform this inversion are Bayesian and SVD unfolding methods. Often the solution requires some additional *a priori* information. For example the solution should be smooth in most cases.

1694 **4.3.1 Bayesian unfolding**

The bayesian (iterative) method is based on the Bayes formula [].

$$P(C_i|E_j) = \frac{P(E_j|C_i) P_0(C_i)}{\sum_{l=1}^{n_C} P(E_j|C_l) P_0(C_l)},$$

1695 i.e. the probability of Cause ("truth") C_i given Effect ("observed") E_j is proportional to the probability of observing E_j given C_i (response matrix) and the 1696 truth distribution $P_0(C_i)$.
1697

At first P_0 is given some starting distribution, either a uniform distribution or some guess of the final distribution. Taking into account the inefficiency this gives

$$\hat{n}(C_i) = \frac{1}{\epsilon_i} \sum_{j=1}^{n_E} n(E_j) P(C_i|E_j),$$

where

$$P(C_i|E_j) = \frac{P(E_j|C_i) P_0(C_i)}{\sum_{l=1}^{n_C} P(E_j|C_l) P_0(C_l)},$$

1698 and

$$\hat{n}(C_i) = \frac{1}{\epsilon_i} \sum_{j=1}^{n_E} n(E_j) P(C_i|E_j). \quad (49)$$

First $P(C_i|E_j)$ is calculated with the uniform distribution or best guess of the shape of the distribution. This is then used to calculate the new distribution $\hat{P}(C_i)$

$$\hat{N}_{true} = \sum_{i=1}^{n_C} \hat{n}(C_i), \quad \hat{P}(C_i) = P(C_i|n(E)) = \frac{\hat{n}(C_i)}{\hat{N}_{true}}$$

1699 P_0 is then replaced with \hat{P} and the procedure is repeated until an acceptable
1700 solution is found.

1701 The bayesian procedure alongside with the SVD unfolding method are implemented in the RooUnfold package [166], which is used to perform the unfolding in 1702 practice. In RooUnfold the number of iterations is given beforehand. In practice 1703 this requires some trial and error. The number of iterations should be as low as 1704 possible, as the errors increase when going further in the iterations, but the number 1705 of iterations must be high enough so that the correct distribution is extracted.
1706

1707 **Error propagation in the Bayesian procedure**

1708 The measured distribution has some statistical uncertainty, this should be reflected
1709 in the unfolded distribution. Additionally the response matrix may have some
1710 uncertainty if the statistics used in the Monte Carlo simulation were limited.

1711 For errors originating from the measured distribution RooUnfold uses the error
1712 propagation matrix

$$\frac{\partial \hat{n}(C_i)}{\partial n(E_j)} = M_{ij} + \frac{\hat{n}(C_i)}{n_0(C_i)} \frac{\partial n_0(C_i)}{\partial n(E_j)} - \sum_{k=1}^{n_E} \sum_{l=1}^{n_C} \frac{n(E_k) \epsilon_l}{n_0(C_l)} M_{ik} M_{lk} \frac{\partial n_0(C_l)}{\partial n(E_j)}, \quad (50)$$

1713 where $\hat{n}(C_i)$ is the unfolded result from Eq. 49. This depends upon the matrix
1714 $\frac{\partial n_0(C_i)}{\partial n(E_j)}$, which is $\frac{\partial \hat{n}(C_i)}{\partial n(E_j)}$ from the previous iteration. In the first iteration, $\frac{\partial n_0(C_i)}{\partial n(E_j)} = 0$
1715 and $\frac{\partial \hat{n}(C_i)}{\partial n(E_j)} = M_{ij}$.

1716 The error propagation matrix V is used to obtain the covariance matrix on the
1717 unfolded distribution

$$V(\hat{n}(C_k), \hat{n}(C_l)) = \sum_{i,j=1}^{n_E} \frac{\partial \hat{n}(C_k)}{\partial n(E_i)} V(\hat{n}(E_i), \hat{n}(E_j)) \frac{\partial \hat{n}(C_l)}{\partial n(E_j)}, \quad (51)$$

1718 where $V(\hat{n}(E_i), \hat{n}(E_j))$ is the covariance matrix of the measurements. In count-
1719 ing experiments common in particle physics, each bin is independently Poisson
1720 distributed, with

$$V(\hat{n}(E_i), \hat{n}(E_j)) = n(E_i) \delta_{ij} \quad (52)$$

1721 The error propagation matrix for the response matrix is

$$\begin{aligned} \frac{\partial \hat{n}(C_i)}{\partial P(E_j|C_k)} &= \frac{1}{\epsilon_i} \left(\frac{n_0(C_i) n(E_j)}{f_j} - \hat{n}(C_i) \right) \delta_{ik} - \frac{n_0(C_k) n(E_j)}{f_j} M_{ij} + \\ &\quad \frac{\hat{n}(C_i)}{n_0(C_i)} \frac{\partial n_0(C_i)}{\partial P(E_j|C_k)} - \frac{\epsilon_i}{n_0(C_i)} \sum_{l=1}^{n_E} \sum_{r=1}^{n_C} n(E_l) M_{il} M_{rl} \frac{\partial n_0(C_r)}{\partial P(E_j|C_k)}, \end{aligned} \quad (53)$$

1722 where $\frac{\partial n_0(C_i)}{\partial P(E_j|C_k)}$ is the error propagation matrix from the previous iteration,
1723 $\frac{\hat{n}(C_i)}{\partial P(E_j|C_k)}$. From the first iteration, this is zero and the final two terms in Eq. 53
1724 disappear.

1725 The covariance matrix due to these errors is given by

$$V(\hat{n}(C_k), \hat{n}(C_l)) = \sum_{j,s=1}^{n_E} \sum_{i,r=1}^{n_C} \frac{\partial \hat{n}(C_k)}{\partial P(E_j|C_i)} V(P(E_j|C_i), P(E_s|C_r)) \frac{\partial \hat{n}(C_l)}{\partial P(E_s|C_r)}, \quad (54)$$

1726 where $V(P(E_j|C_i), P(E_s|C_r))$ can be taken as multinomial, Poisson or other
1727 distribution.

1728 **4.3.2 Toy Monte Carlo**

1729 **remove?** A toy Monte Carlo simulation was performed to see the performance
1730 in an ideal case. The simulations samples jet p_T values from the observed p_T
1731 distribution. Starting from this p_T the simulations starts creating tracks with

$$p_{\text{track}} = z_{\text{track}} p_{T\text{jet}} \quad (55)$$

1732 where z_{track} is sampled from the observed z distribution. All tracks below 0.15 GeV
1733 are discarded. Sampling is continued until the sum of the track transverse momenta
1734 exceeds the jet transverse momentum. Jet is then defined as the sum of the track
1735 momenta.

1736 Simultaneously a p_T dependant observation efficiency is applied to the tracks
1737 and a separate observed jet is calculated using only the observed tracks. Additionally
1738 a set of fake tracks is added to the observed jet. Tracks are always either
1739 observed or not at the true momentum. No smearing is added to the observed
1740 momentum.

1741 Afterwards the tracks are looped over for j_T calculation. For observed tracks
1742 we calculate j_T with respect to both the true jet axis and the observed jet. 2D
1743 Response matrix is filled with

$$(j_T^{\text{obs}}, p_{T\text{jet}}^{\text{obs}}, j_T^{\text{true}}, p_{T\text{jet}}^{\text{true}}) \quad (56)$$

1744 In practice this is done with a set of 3D histograms, where $p_{T\text{jet},\text{true}}$ determines
1745 the histogram index and the remaining three values the bin in the 3D histogram.

1746 After creating the response matrices, an identical procedure is carried out to
1747 the create testing data. Now instead of filling response matrices, 2D histograms
1748 are filled with $(j_T^{\text{obs}}, p_{T\text{jet}}^{\text{obs}})$ and $(j_T^{\text{true}}, p_{T\text{jet}}^{\text{true}})$

1749 The observed distributions are unfolded using RooUnfold's 2D Bayesian (iter-
1750 ative) algorithm. Results are shown in figure 35. Aside from some discrepancy at
1751 very low j_T the true distribution is retrieved well.

1752 **4.3.3 Pythia Response matrices**

1753 A PYTHIA6 simulation was carried out to determine the response matrices. [Details
1754 of the simulation](#)

1755 Response matrices are filled through correlation between MC detector and
1756 particle level jets and tracks.

1757 The ranges of both j_T and $p_{T\text{jet}}$ extend the ranges in end results. These are
1758 shown in Tab. 5. The ranges are the same in detector and particle level.

1759 When calculating j_T for MC particles the code checks whether a corresponding
1760 detector level track exists and if that track had a j_T value. Additionally the code

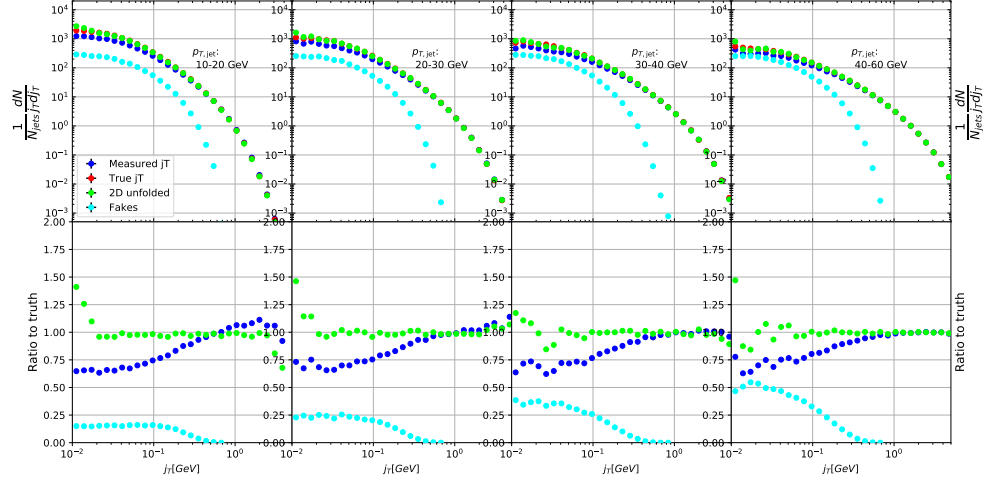


Figure 35: Results from unfolding in Toy Monte Carlo

Table 5: j_T and p_T ranges used in unfolding. The same ranges are used for detector and truth level.

	j_T	$p_{T\text{jet}}$
Min	0.01	5
Max	20	500

1761 checks for detector level tracks that don't have corresponding particle level track
1762 with a j_T value.

1763 There are several possibilities that have to be taken into account:

- 1764 We find a corresponding track with a j_T value, response matrix is filled
1765 normally with $(j_T^{\text{obs}}, p_{\text{Tjet}}^{\text{obs}}, j_T^{\text{true}}, p_{\text{Tjet}}^{\text{true}})$
- 1766 We don't find a corresponding track. Record $(j_T^{\text{true}}, p_{\text{Tjet}}^{\text{true}})$ as a miss
- 1767 We find a corresponding track, but it didn't have j_T value. Most likely
1768 because it was not part of a jet in the detector level set. Similary record
1769 $(j_T^{\text{true}}, p_{\text{Tjet}}^{\text{true}})$ as a miss
- 1770 For detector level tracks that have no correspondence in particle level set the
1771 code records $(j_T^{\text{obs}}, p_{\text{Tjet}}^{\text{obs}})$ as a fake

1772 In the analysis code the response matrix is made of an array of 3 dimensional
1773 histograms, with $(j_T^{\text{obs}}, p_{\text{Tjet}}^{\text{obs}}, j_T^{\text{true}})$ as axes. The histogram index gives the $p_{\text{Tjet}}^{\text{true}}$
1774 value.

1775 4.3.4 Unfolding algorithm

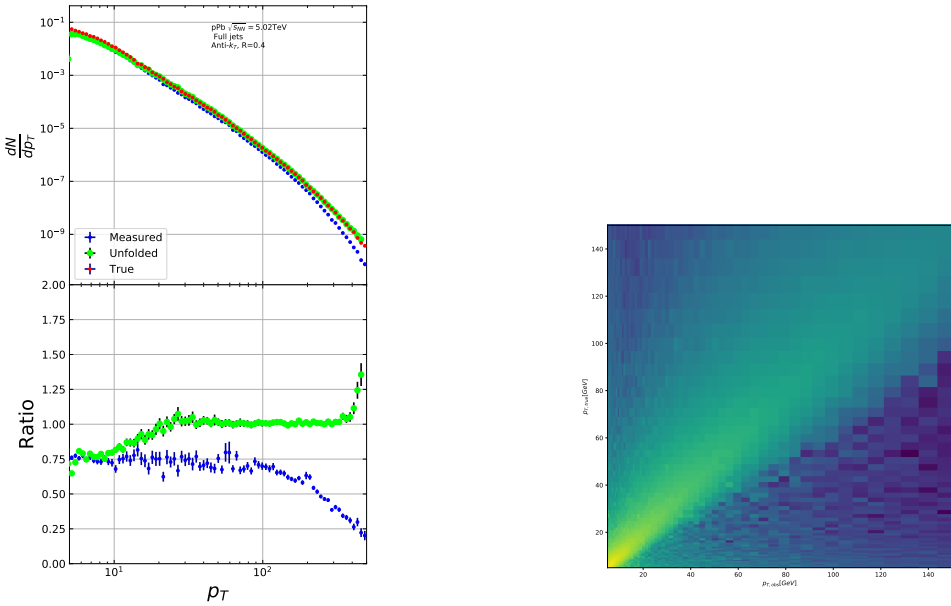
1776 As a primary method unfolding is performed with an iterative (bayesian) algorithm
1777 using the RooUnfold [166] package. The number of iterations used is 4.

1778 4.3.5 Unfolding closure test

1779 Pythia set is divided in 2 halves. First is used to fill the response matrices, as well
1780 as record missed and fake tracks. Second half is used to test the effectiveness of
1781 the unfolding method. Jet p_T distributions are shown in figure 36a and response
1782 matrix are shown in figure 36b.

1783 Response matrices within single jet p_T bins are shown in figure 37. Results
1784 from the closure test are shown in figure 38. In the lowest jet p_T bins unfolding
1785 fails to recover the true distribution. The lowest jet p_T bins are dominated by
1786 combinatorial jets and thus the true detector response is likely not retrieved.

1787 Above $30 \text{ GeV} < p_{\text{Tjet}} < 40 \text{ GeV}$ the distribution is recovered well in the mid
1788 j_T region. At $j_T < 0.1 \text{ GeV}$ there is clear discrepancy. The final results are shown
1789 only for $j_T > 0.1 \text{ GeV}$. Additionally there is some discrepancy at very high j_T .
1790 This is taken into account in the unfolding systematics. (TODO: Show this)



(a) Unfolded jet p_T distribution in PYTHIA closure test (b) Jet p_T response matrix from unfolding closure test

Figure 36: Jet p_T in unfolding closure test

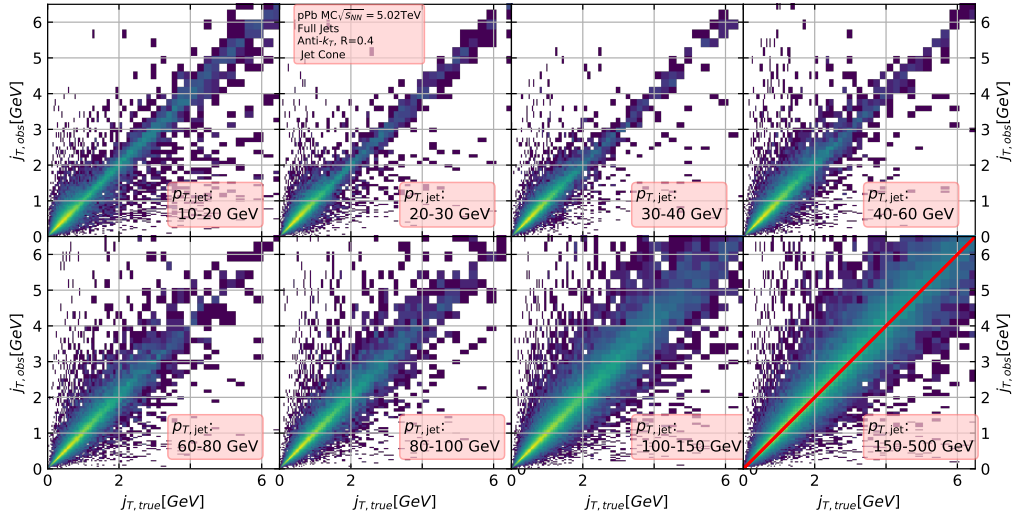


Figure 37: j_T Response matrices in individual $p_{T,jet}$ bins

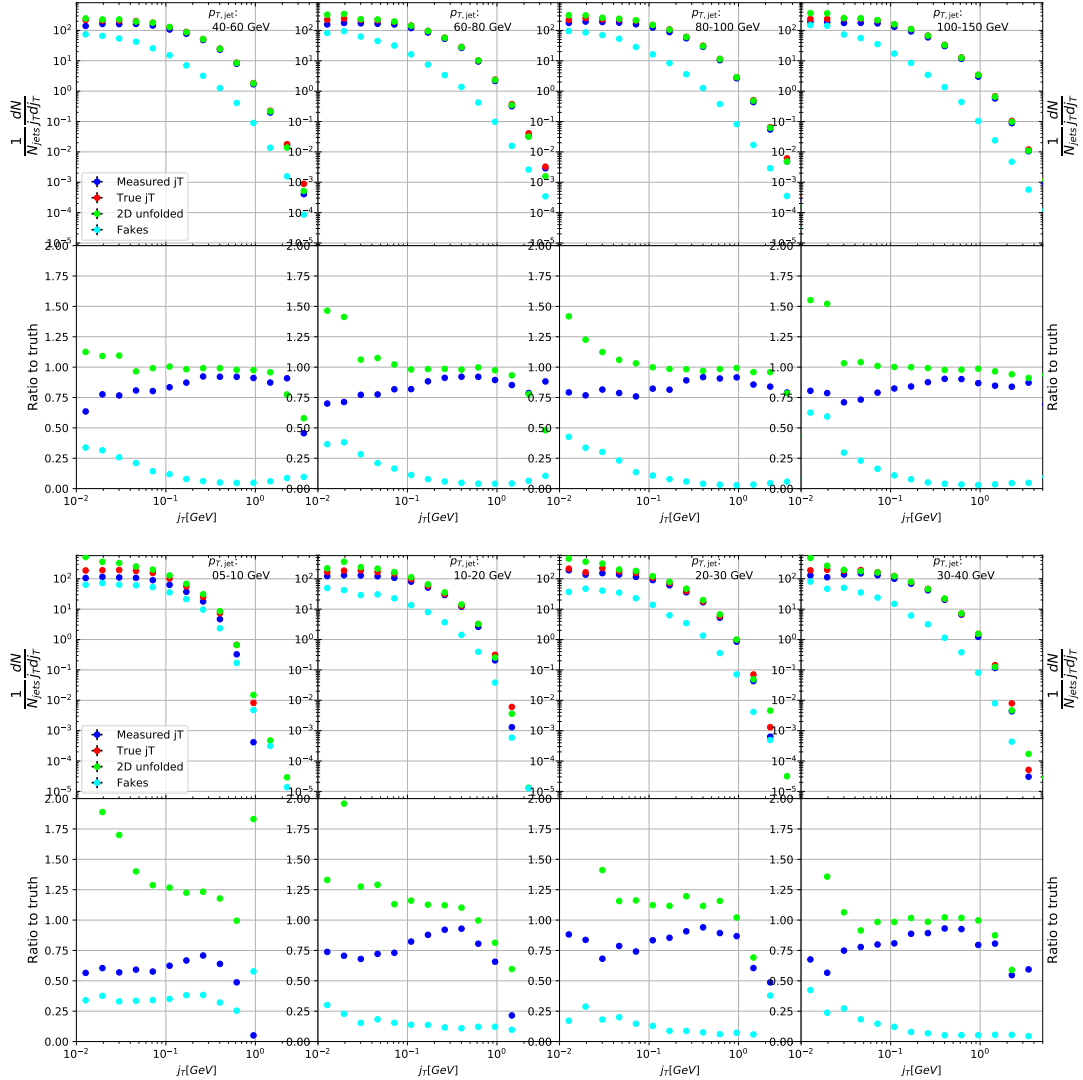


Figure 38: Pythia closure test results. Fake tracks include also tracks that do exist in the true dataset, but for one reason or another were not given j_T values. j_T is only calculated for tracks that are associated with jets

1791 4.4 Background

1792 When calculating j_T distribution for jet constituents there is a contribution from
1793 underlying event (UE), i.e. tracks that just happen to be close to the jet axis.
1794 To find the signal coming from the actual jet we need to subtract the background
1795 (UE) contribution. On a jet-by-jet basis this is impossible, so one must estimate
1796 the background contribution in the inclusive distribution. A schematic view of the
1797 background contribution is shown in Fig. 39.

1798 We have two methods for background estimation. In the first we look at the
1799 direction perpendicular to the jet. This is assumed to be the region least likely to
1800 contain jet contributions. In the second method we randomly assign the tracks of
1801 event new ϕ and η values. The result is thus guaranteed to be uncorrelated.

1802 4.4.1 Perpendicular cone background

1803 As a primary method to estimate the background we look at regions of the detector
1804 where there are no tracks from jets, but only uncorrelated tracks from the under-
1805 lying event. The underlying event is thus estimated by looking at an imaginary
1806 jet cone perpendicular to the observed jet axis ($\frac{\pi}{2}$ Rotation in ϕ).

1807 After calculating the j_T values for tracks in the jet, we rotate the jet axis by
1808 $\frac{\pi}{2}$ in positive ϕ direction. We check that there are no other jets closer than $2R$ to
1809 the rotated axis. If there are then background calculation is skipped for this jet.
1810 Probability of this happening is 1-2% depending on the jet p_T bin.

1811 If we don't find other jets in the vicinity we move on to estimate the background.
1812 We find all tracks within a cone of radius R around the rotated axis and calculate
1813 j_T of these tracks with respect to the rotated axis. Auto-correlations are added to
1814 match effect to jet. (see 4.4.3)

1815 4.4.2 Random background

1816 In the random background method we look at all tracks in the event, except for
1817 tracks close to jets found by the jet algorithm. We randomly assign new η and ϕ
1818 values to all tracks using uniform distributions with $|\eta| < 1.0$. p_T values are kept
1819 the same. To increase statistics there is a possibility to create a number of random
1820 tracks for each actual track. In the analysis we do this 10 times for each track.
1821 Again the track p_T value is kept the same.

1822 We create a random jet cone from uniform η and ϕ distributions. Here $|\eta| <$
1823 0.25. Now we calculate j_T of the random tracks with respect to the random cone
1824 axis. Auto-correlations are added before calculating j_T (see 4.4.3)

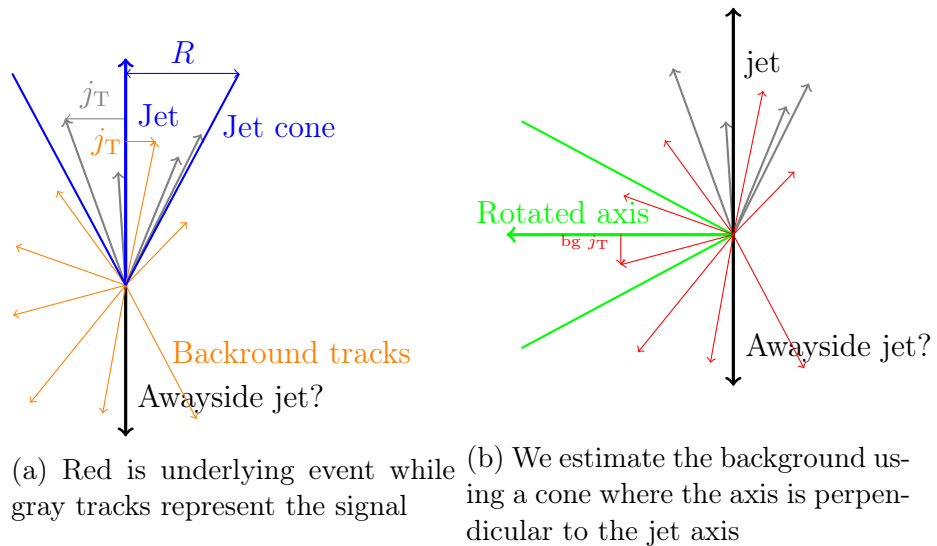


Figure 39: Background estimation

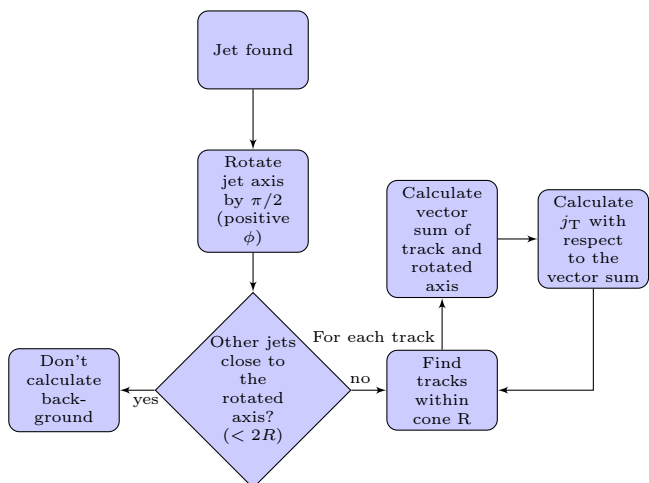


Figure 40: Flowchart representation of the perpendicular cone background procedure

1825 **4.4.3 Auto-correlations**

1826 Jet axis is simply a vector sum of all its constituents. Thus having an additional
1827 track in the jet from the underlying event moves the jet axis towards this track.
1828 Since the axis is now closer to the track, it has a smaller j_T value. Assuming
1829 a 1 GeV background track at the edge of a $R = 0.4$ cone the j_T value would be
1830 0.4 GeV. If this is added to a 5 GeV jet, the j_T value becomes 0.33 GeV. In a 50 GeV
1831 jet it would be 0.39 GeV. This is a region where the inclusive j_T distribution is
1832 dominated by background. The distribution is also steeply falling. Overestimating
1833 the background can lead to a situation where the background estimation exceeds
1834 the inclusive distribution.

1835 To take this effect into account we can't use a fixed axis for background, but
1836 it has to behave like a jet would when additional tracks are added. Thus before
1837 calculating j_T values we make a vector sum of the track and the axis used for back-
1838 ground, which is either the perpendicular cone axis or the random axis depending
1839 on the background method. In each case the momentum of this background axis
1840 is assumed to be the same as the jet which initiated the background estimation.

1841 In pPb data there is on average about one underlying event track in a $R = 0.4$
1842 cone. If there would be more, one should consider taking the vector sum of all
1843 tracks inside the cone. As there is usually only one track and if there are more it's
1844 unlikely that more than one has high momentum, taking the vector sum track-by-
1845 track should be enough.

1846 **4.4.4 Background methods**

1847 Comparison between perpendicular cone and random background in figure 41. The
1848 advantage of the random background method is the added amount of statistics as
1849 the procedure can be repeated several times for each event. However, it seems
1850 that, especially in the highest $p_{T\text{jet}}$ bins there is some jet contribution left at the
1851 high end. Naturally there is no correlation between the tracks and the background
1852 axis, but if some high momentum tracks originating from jets were not subtracted
1853 and happen to hit the edge of the background cone, they can increase the high j_T
1854 yield in the background estimation.

1855 One should note that the results from perpendicular cone background show no
1856 observable change between $p_{T\text{jet}}$ bins. It is a good indication that the background
1857 is actually dominated by the underlying event over the entire j_T region.

1858 **4.5 Fitting**

1859 After unfolding and background subtraction the resulting signal distributions are
1860 fitted with a 2 component function shown in Eq. 57. Gaussian distribution is used

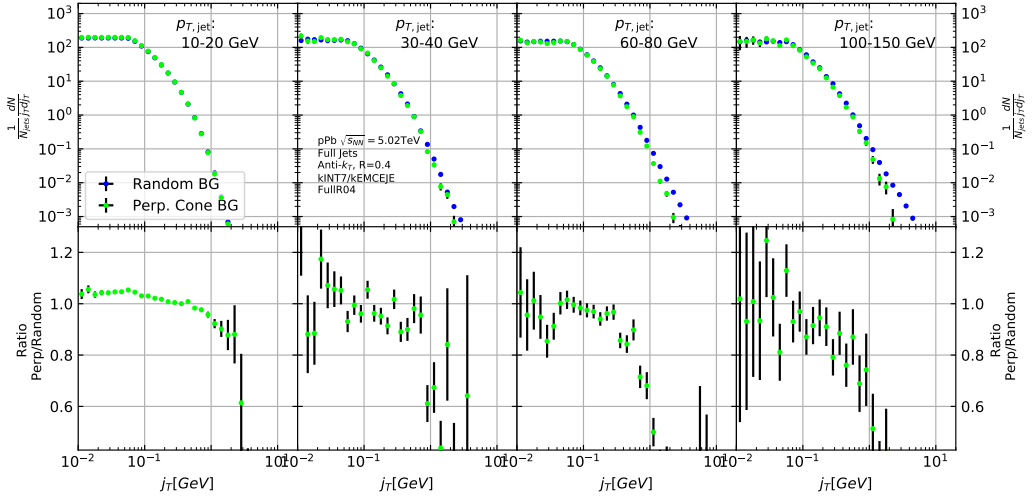


Figure 41: j_T background with two different methods

for low j_T and an inverse gamma function is used for high j_T . The gaussian is taken to have the center at $j_T = 0$. In total this gives 5 parameters. The fitting procedure was inspired by the dihadron j_T analysis by ALICE [2]. The complete fitting function is

$$\frac{1}{N_{\text{jets}} j_T d j_T} \frac{dN}{d j_T} = \frac{B_2}{B_1 \sqrt{2\pi}} e^{-\frac{j_T^2}{2B_1^2}} + \frac{B_3 B_5^{B_4}}{\Gamma(B_4)} \frac{e^{-\frac{B_5}{j_T}}}{j_T^{B_4+1}}. \quad (57)$$

To achieve stable results the fitting is performed in two steps. First both components are fitted separately. Gaussian component is fitted to the low end in j_T . Inverse gamma component is fitted to j_T above 1 GeV/c. After getting the results from the individual fits they are combined into a single function with initial values from the individual results and an additional fit is performed.

After getting the fit function $\sqrt{\langle j_T^2 \rangle}$ (RMS) and yield values are extracted separately from each component. The narrow component RMS is

$$\sqrt{\langle j_T^2 \rangle} = \sqrt{2} B_1,$$

and the wide component RMS value is calculated as

$$\sqrt{\langle j_T^2 \rangle} = \frac{B_5}{\sqrt{(B_4 - 2)(B_4 - 3)}},$$

where it is required that $B_4 > 3$.

₁₈₇₄ The statistical errors can be calculated with the general error propagation
₁₈₇₅ formulas. As a result one gets errors for the narrow component RMS

$$\delta \sqrt{\langle j_T^2 \rangle} = \sqrt{2} \delta B_1 \quad (58)$$

₁₈₇₆ and for the wide component RMS

$$\delta \sqrt{\langle j_T^2 \rangle} = \sqrt{\left(\frac{(5 - 2B_4) B_5 \delta B_4}{(2(B_4 - 2)(B_4 - 3))^{\frac{3}{2}}} \right)^2 + \left(\frac{\delta B_5}{\sqrt{(B_4 - 2)(B_4 - 3)}} \right)^2} \quad (59)$$

1877 5 Systematic errors

1878 **Extend Systematics** The main systematic uncertainties in this analysis come from
1879 the background estimation, the unfolding procedure and uncertainty in the track-
1880 ing efficiency.

1881 The systematics in background estimation were studied using an alternative
1882 method to extract the background, the random background method.

1883 The systematic uncertainty that arises from the unfolding procedure is esti-
1884 mated by performing the unfolding with two separate methods. Data corrected
1885 by the iterative unfolding method are used as the results and the SVD unfolding
1886 method is employed to estimate the uncertainty. In a PYTHIA closure test the
1887 true distribution was in general found to be between the unfolded distributions
1888 from the iterative and SVD method. The difference between the methods when
1889 unfolding data should give a reasonable estimate of the unfolding uncertainty. The
1890 resulting uncertainty is below 8% for both wide and narrow component RMS.

1891 5.1 Background

1892 The uncertainty coming from background estimation is estimated by subtracting
1893 the background separately for the perpendicular cone and random background
1894 methods. Comparisons of the resulting signal distributions are shown in Fig. 42.

1895 Fits are then performed on both perpendicular cone and random background
1896 signals. Difference between them is taken as the systematic error. The fits for
1897 individual bins from the random background method are shown in figure 43. Re-
1898 sulting differences between the methods for different components are shown in
1899 figure 44. The dotted lines are put at $\pm 5\%$ for the narrow component and at
1900 $\pm 8\%$ for the wide component. These are taken as systematic estimates for the
1901 entire $p_{T\text{jet}}$ range.

1902 5.2 Unfolding

1903 Unfolding is the second major source of systematic uncertainty. To estimate the
1904 uncertainty related to the unfolding procedure several checks are performed. The
1905 main systematic uncertainty estimation comes from comparing results performed
1906 using both SVD and Bayesian unfolding. Difference between the methods is taken
1907 as the systematic error. Since SVD unfolding does not have a 2 dimensional
1908 options, the unfolding is done bin by bin. The resulting distributions after SVD
1909 unfolding and background subtraction with the perpendicular cone method are
1910 shown in fig 45.

1911 As in the background systematic estimation, fits are performed for both cases
1912 separately. Resulting differences between the methods for different components

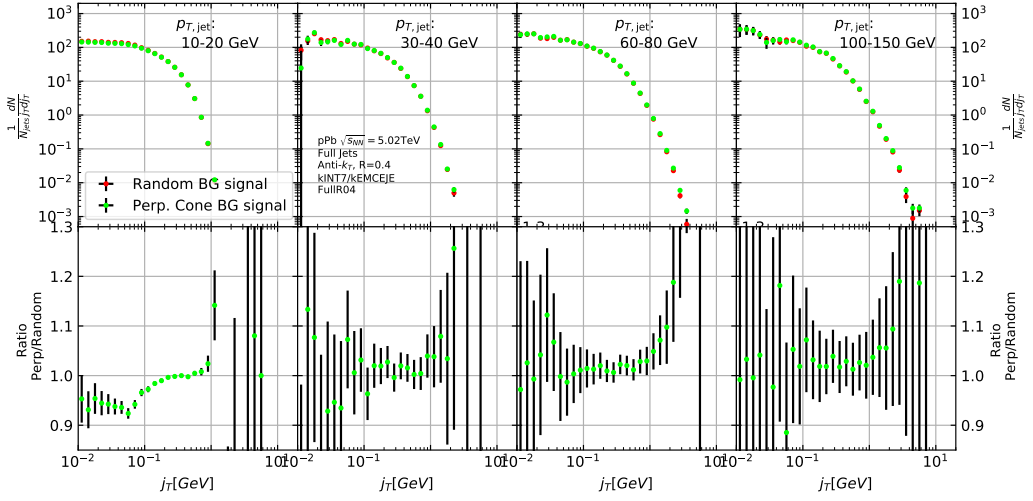


Figure 42: Comparison of the effect of background method on j_T signal.

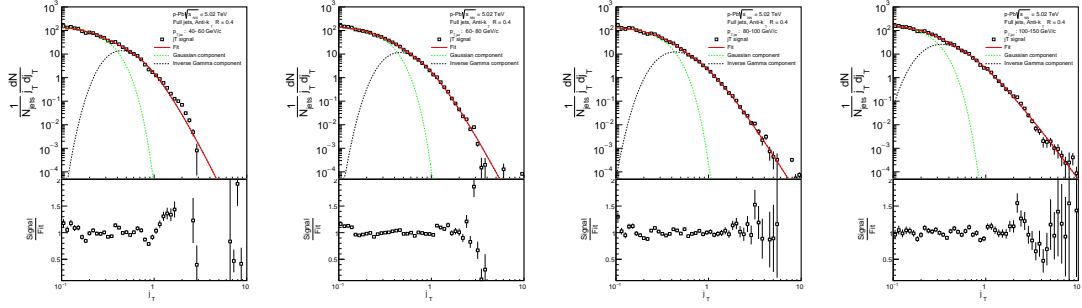


Figure 43: j_T signal with random background subtraction fits in different jet p_T bins

are shown in figure 46. The dotted lines are at $\pm 8\%$ for both components. These are taken to be the systematic uncertainty related to unfolding.

Several other systematic checks were performed with the Bayesian unfolding procedure. They are described in the following sections. As these are small compared to the main uncertainty they are not included separately.

5.2.1 Effect of number of iterations

The iterative unfolding algorithm permits the change of number of iterations. The unfolding procedure was carried out using different numbers of iterations. The results from these different cases are shown in Fig. 47. The results are compared to the default unfolding algorithm with 4 iterations. The difference in results

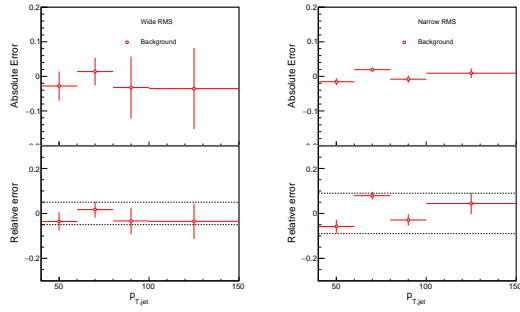


Figure 44: Differences between perpendicular cone and random background subtraction in the resulting RMS values.

Figure 45: Resulting signal distributions from SVD unfolding with the perpendicular cone background methods. These are compared to the results from the Bayesian algorithm to estimate the systematic uncertainty.

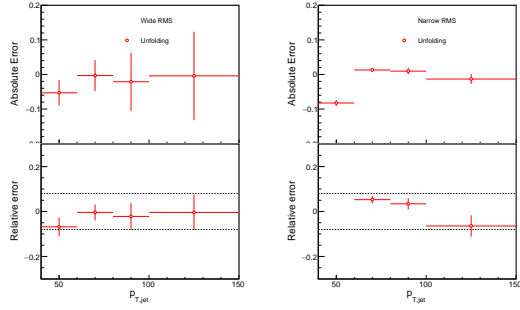


Figure 46: Differences between Bayesian and SVD unfolding in the resulting RMS values

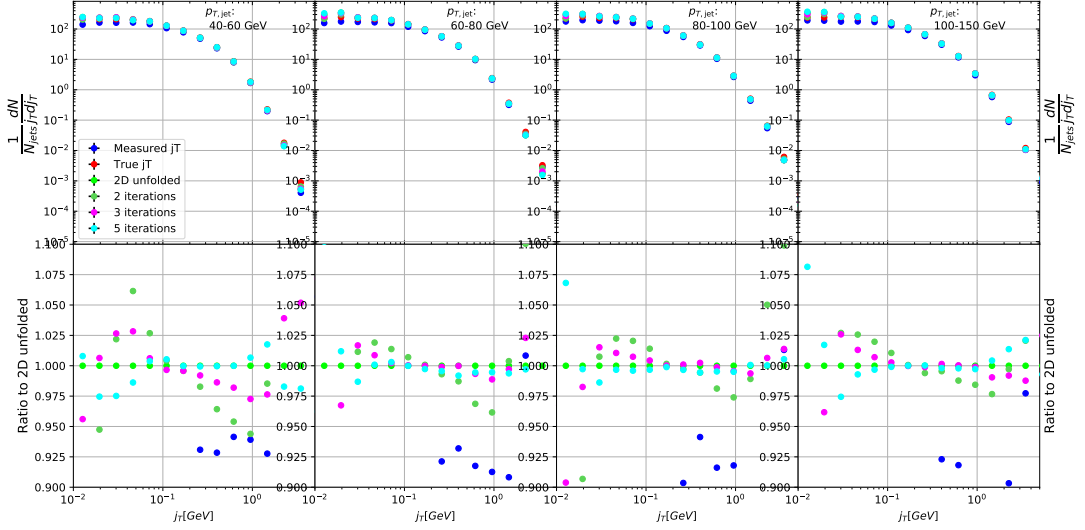


Figure 47: Unfolding with different number of iterations

Figure 48: Effect of changing prior from true distribution in PYTHIA to the unfolded distribution. [Missing figure](#)

1923 between the different cases is mostly less than 2.5%.

1924 5.2.2 Effect of different prior

1925 The iterative algorithm requires a prior estimate of the shape of the distribution.
1926 As a default prior the truth (particle level) distribution is used. To test the effect
1927 of changing the prior we instead use the unfolded j_T distribution as prior. The
1928 results are compared to the unfolding algorithm with the default prior. This is
1929 shown in Fig. 48. The difference in results between the different cases is mostly less
1930 than 2.5%.

1931 5.2.3 Effect of p_T truncation

1932 As an additional check the unfolding is carried out with different $p_{T\text{jet}}$ truncation
1933 values. By default the full range of $p_{T\text{jet}} > 5\text{GeV}$ is used. We test the unfolding
1934 by only using the response matrix for $p_{T\text{jet}} > 10\text{GeV}$. The results of this test are
1935 shown in Fig. 49. The effects are strongest in the lower $p_{T\text{jet}}$ bins. Also in this
1936 case the difference is less than 2.5 % in all $p_{T\text{jet}}$ bins.

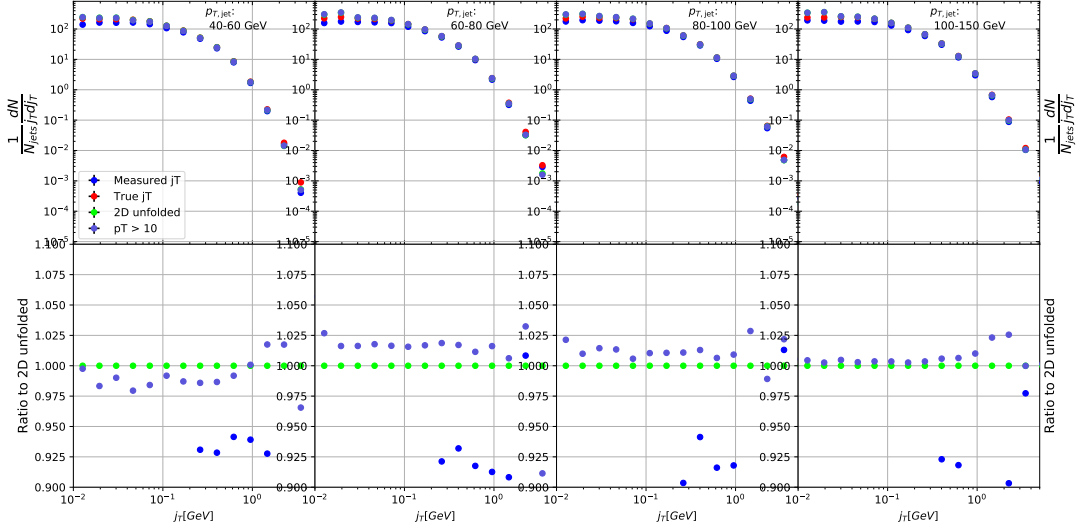


Figure 49: Effect of changing minimum jet p_T used in unfolding from 5 to 10 GeV

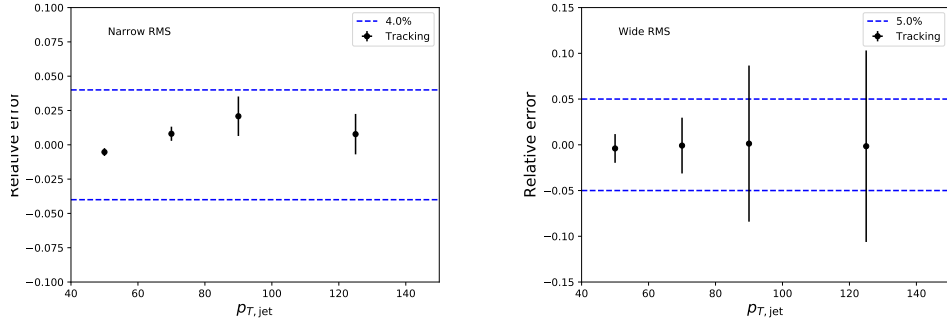


Figure 50: Relative systematic errors resulting from tracking efficiency uncertainty.

1937 5.3 Tracking

1938 Systematic effects originating from uncertainty in the tracking efficiency are es-
 1939 timated through a PYTHIA simulation, where an artificial inefficiency of 3% is
 1940 introduced i.e. 3 % of tracks are randomly removed from each event. The effect
 1941 of this artificial inefficiency is shown in Fig. 50. The systematic uncertainties as-
 1942 signed to tracking efficiency are 4 % for the narrow component and 5 % for the
 1943 wide component.

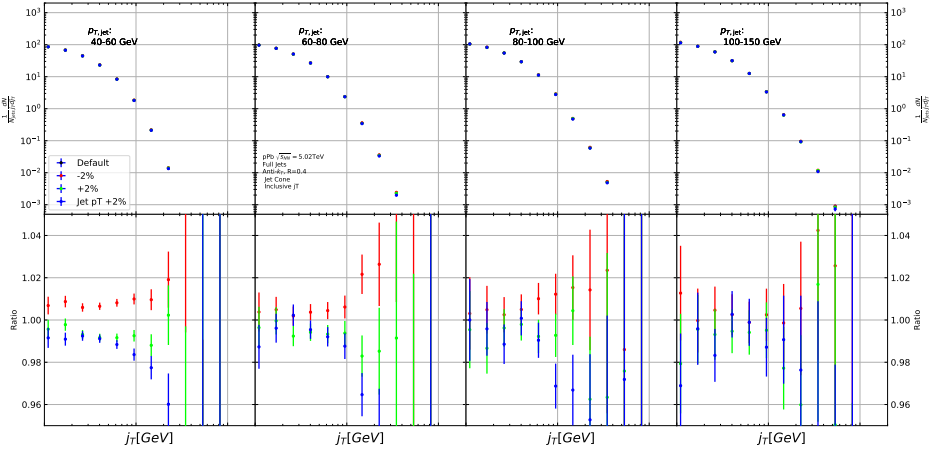


Figure 51: Results from PYTHIA simulations with Cluster energies scaled up and down by 2 %. Additionally jet momenta were scaled by 2 % when determining the jet p_T bin.

1944 5.4 EMCAL clusters

1945 The analysis uses EMCAL clusters only in the reconstruction of jets. Thus the only
 1946 way uncertainty in EMCAL performance can affect the results is through modifica-
 1947 tion of jet momentum or axis.

1948 Uncertainty related to the EMCAL energy scale was estimated by scaling cluster
 1949 energies up and down by 2 % in a PYTHIA particle level simulation. Similarly
 1950 the jet momentum was scaled by $\pm 2\%$ when determining the jet p_T bin. In the
 1951 analysis EMCAL is used only in jet reconstruction, not for calculating j_T . The only
 1952 ways EMCAL uncertainty can affect the analysis are changes in jet energy and jet
 1953 axis. Jet axis shouldn't significantly change, so the main contribution should be
 1954 changes in jet p_T bin.

1955 The resulting differences in the inclusive j_T distributions are shown in Fig. 51.
 1956 Qualitatively the effect of scaling cluster energies is the same as scaling the jet
 1957 energies.

1958 Like in the previous cases fits are performed for the unscaled case and for cases
 1959 with $\pm 2\%$ scaling. The resulting systematic uncertainties are shown in Fig. 52.
 1960 The uncertainty is taken to be 1% for both components.

1961 5.5 Summary/Combining systematics

1962 The different source of the systematic uncertainty are considered as uncorrelated
 1963 and the values of each source are summed in quadrature.

1964 Resulting systematic errors are shown in table 6. The different source of the

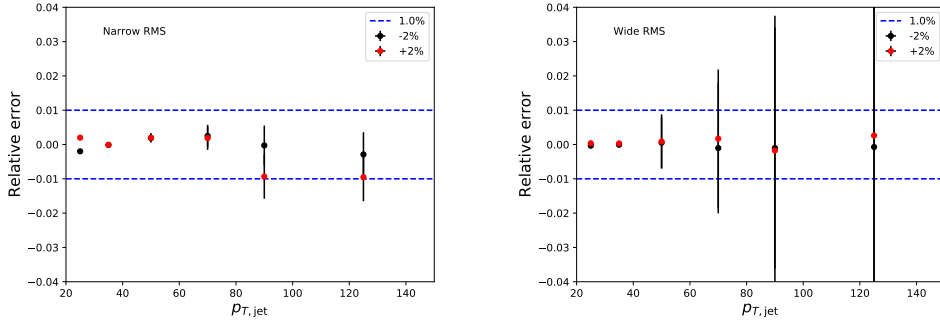


Figure 52: Relative systematic errors resulting from cluster energy uncertainty.

¹⁹⁶⁵ systematic uncertainty are considered to be uncorrelated and are thus combined
¹⁹⁶⁶ bin-by-bin in quadrature to get the total systematic errors. The resulting uncer-
¹⁹⁶⁷ tainty is approximately 9 % for the wide component RMS and 12 % for the narrow
component RMS.

Table 6: Summary of systematic errors

Systematic	Wide RMS	Narrow RMS
Background	5 %	9 %
Unfolding	8 %	8 %
Tracking	4 %	5 %
EMCal	1 %	1 %
Total	10 %	13%

¹⁹⁶⁸

¹⁹⁶⁹ 5.6 Additional checks

¹⁹⁷⁰ 5.6.1 Comparison between A and C side

¹⁹⁷¹ In 2013 there were issues with tracking. To rule out effects on j_T distributions
¹⁹⁷² a study was performed comparing j_T distributions between A and C side. (In
¹⁹⁷³ the p-Pb configuration the proton beam is travelling from A to C) No systematic
¹⁹⁷⁴ differences were observed. Figure 53 shows the comparison between inclusive dis-
¹⁹⁷⁵ tributions between the different sides, both for minimum bias and EMCal triggered
¹⁹⁷⁶ datasets.

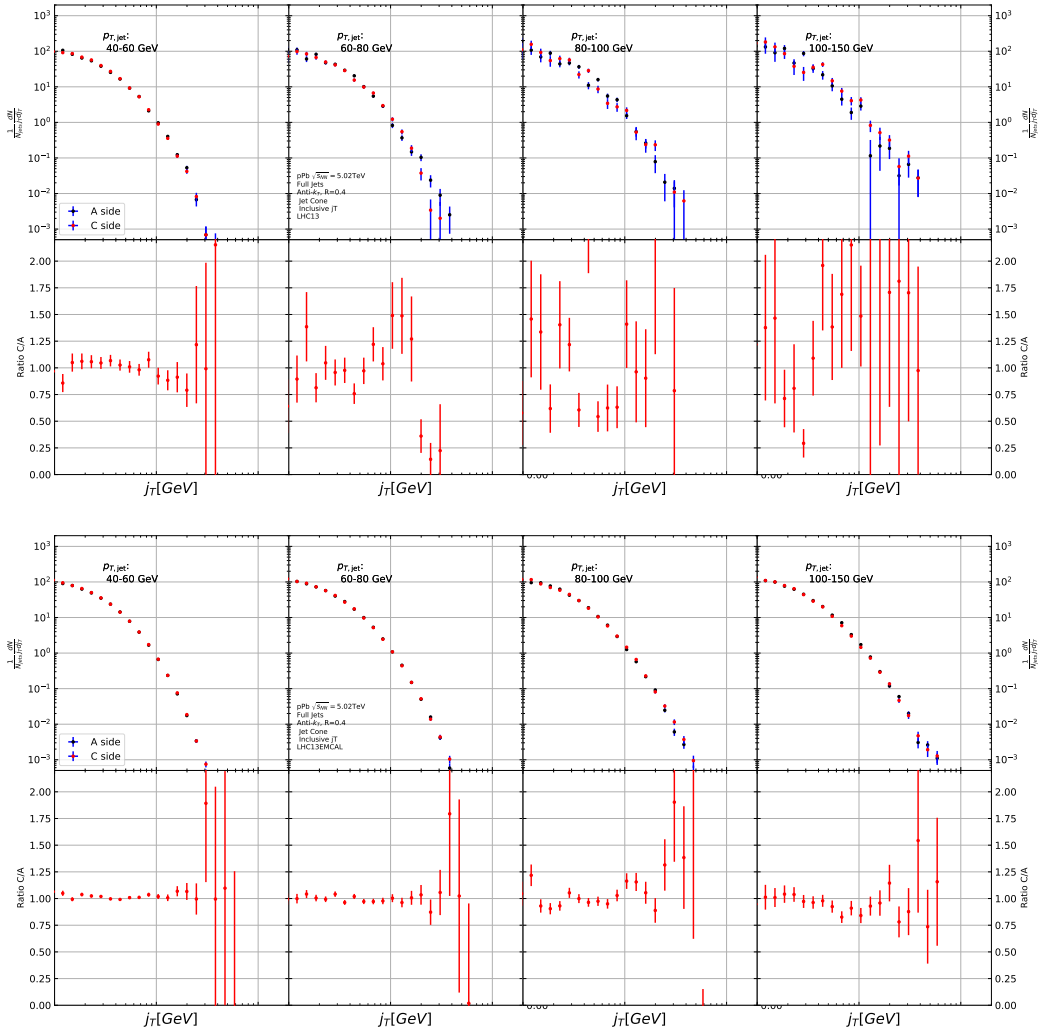


Figure 53: Comparison of inclusive j_T distributions between A and C side for minimum bias and EMCAL triggered data.

6 Results

6.1 Fitting

Fits of j_T distributions in different $p_{T\text{jet}}$ bins with $p_{T\text{jet}} > 40 \text{ GeV}$ are shown in figure 54. Additional $p_{T\text{jet}}$ bins are shown in appendix A. In lowest $p_{T\text{jet}}$ bins the jets are mainly combinatorial which makes background subtraction and unfolding difficult and thus the signal can't be trusted.

The fits describe the data well. There is some fluctuation of the order of 10 % around the fit function. At hight j_T the statistical errors in the signal are large.

6.1.1 RMS values from fitted distributions

RMS results with systematic errors are shown separately in figure 55. Figure 56 shows RMS values for both components combined. The figure also includes results from a PYTHIA simulation.

6.2 High multiplicity

The analysis was repeated taking only events with high multiplicity. Three different multiplicity cuts were used; 10 %, 1 % and 0.1 %. We used ZDC(TODO) as a centrality estimator. As argued in section 1.6.3 the zero-degree energy deposit should provide a centrality estimator with minimal bias from jets production. Resulting j_T distributions are shown Fig. 57. As the statistics are limited in the high multiplicity runs, it was hard to achieve stable fits to the distributions. Thus the RMS values are not shown.

From the figure one can observe no systematic modification when tighter multiplicity cuts are introduced.

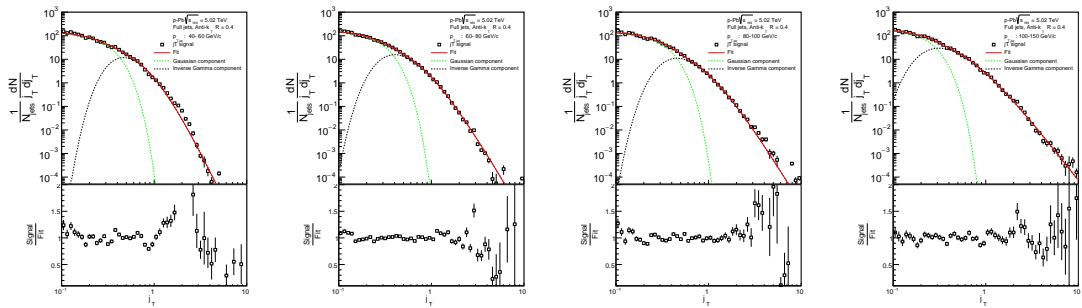


Figure 54: j_T signal fits in different jet p_T bins

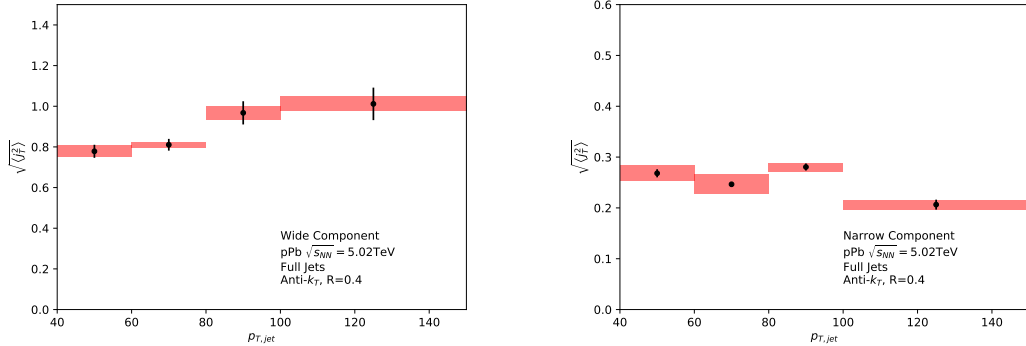


Figure 55: RMS values extracted from the fits for the gaussian (narrow) and inverse gamma (wide) components

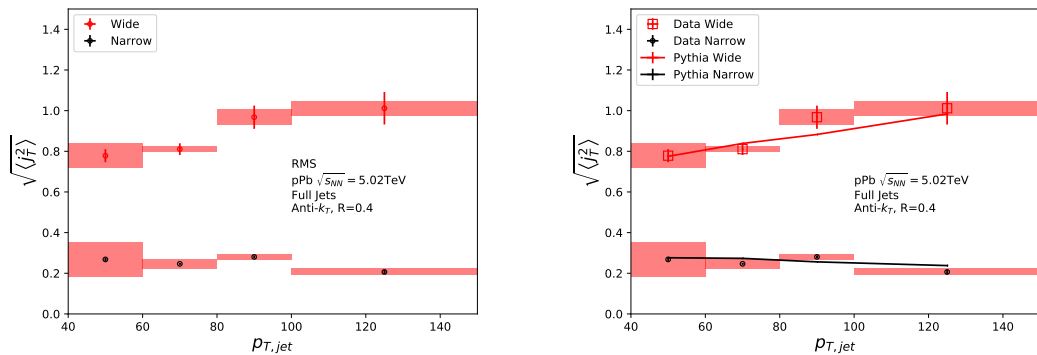


Figure 56: RMS values extracted from the fits for the gaussian (narrow) and inverse gamma (wide) components

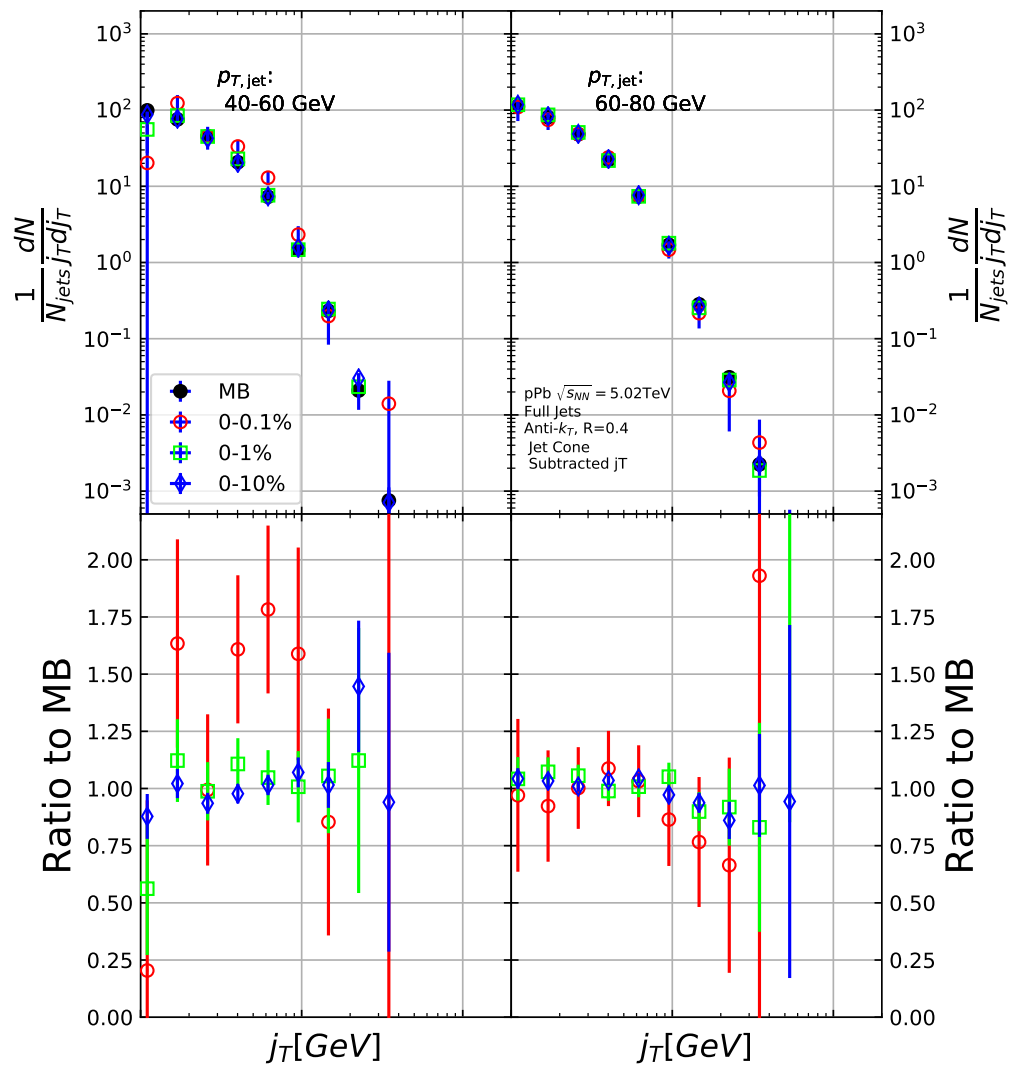


Figure 57: j_T distributions for high multiplicity p–Pb events. Replace figure

1999 7 Discussion

2000 [167, 168]

2001 7.1 Dihadron j_T

2002 The jet fragmentation transverse momentum j_T has been studied previously at
 2003 ALICE with dihadron correlations [2]. The study took the leading hadron in
 2004 each event and calculated j_T for any near-side tracks with respect to the leading
 2005 hadron. Thus there is no kinematical limit to j_T from the jet cone. In the analysis
 2006 the background shape is estimated using pairs with large $\Delta\eta$. The normalisation of
 2007 the background is done when fitting the j_T distribution. The inclusive and signal
 2008 distributions from the analysis are shown in Fig. 58. The inclusive distribution is
 2009 fitted with a three component function,

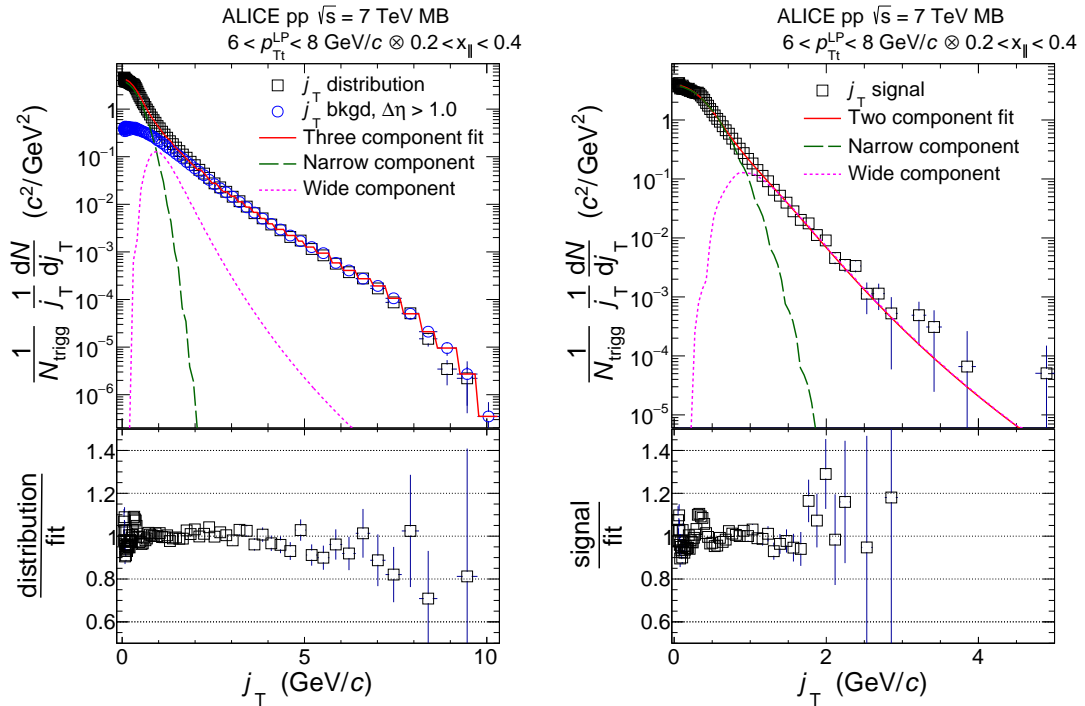


Figure 58: *Left:* Measured j_T distribution including a three-component fit. The three components describe the background (circular symbols), hadronization (long dashed line), and showering (short dashed line). *Right:* The same j_T distribution but with background subtracted.

2010 The analysis was the first to introduce this factorisation of j_T into components.

At $j_T \approx 0.4\text{GeV}$ there is a small bump in the distribution to fit ratio. This was attributed to cases where the trigger particle decayed after hadronisation. As it is difficult to correct for, this bump is included in the systematic errors of the results.

The RMS results from the fitting in both pp and p–Pb collisions are shown in Fig. 59. Qualitatively the results are similar to jet j_T results. The RMS value of the wide component has an increasing trend with respect to p_{Tt}/p_{Tjet} , while the RMS value of the narrow component stays constant. Both components are well described by PYTHIA simulations. As seen in the figures there is no difference between pp and p–Pb results in the dihadron analysis.

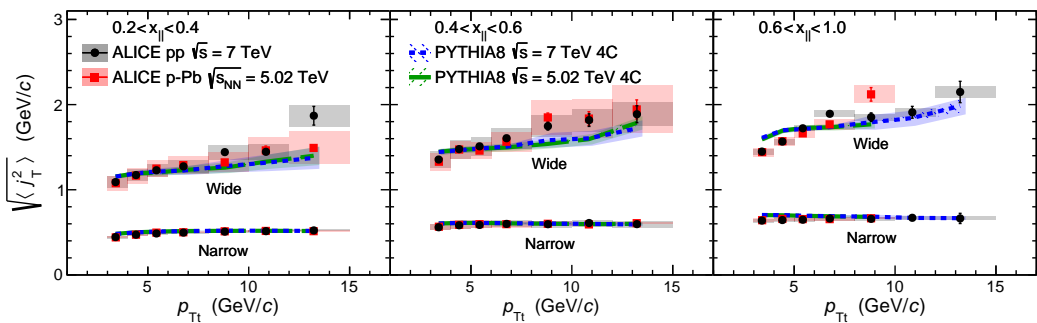


Figure 59: RMS values of the narrow and wide j_T components in the dihadron correlation analysis. Results from pp collisions at $\sqrt{s} = 7\text{ TeV}$ (circular symbols) and from p–Pb collisions at $\sqrt{s_{NN}} = 5.02\text{ TeV}$ (square symbols) are compared to PYTHIA 8 tune 4C simulations at $\sqrt{s} = 7\text{ TeV}$ (short dashed line) and at $\sqrt{s} = 5.02\text{ TeV}$ (long dashed line). Different panels correspond to different $x_{||}$ bins with $0.2 < x_{||} < 0.4$ on the left, $0.4 < x_{||} < 0.6$ in the middle, and $0.6 < x_{||} < 1.0$ on the right. The statistical errors are represented by bars and the systematic errors by boxes. [2]

7.2 Comparing dihadron and jet j_T results

Comparison to RMS values in dihadron analysis [2] are shown in figure 60. For comparison the dihadron trigger p_T bins are converted to jet p_T bins and vice versa. Bin-by-bin comparison is still not possible, but dihadron analysis gives systematically larger RMS values. This could be caused by several kinematical factors. In jet j_T analysis the jet cone limits possible j_T values and thus the width and RMS of the j_T distributions. The effect of this limitation can be studied by changing the cone size as is described in section 7.2.1.

The trends are similar in dihadron and jet j_T results. Wide component RMS values tend to increase with increasing $p_{T,trigger}/p_{Tjet}$. Narrow component RMS

increases slightly in dihadron analysis but not in jet j_T , WHY? (Depends on $x_{||}$ bin in dihadron)

In general dihadron j_T gives wider distributions with larger RMS values. In jet analysis the cone size limits width and thus the RMS values. The effect of this limitation can be studied by changing the cone size as is described in section 7.2.1.

Additionally the leading track is an imperfect estimate of the jet/original parton. Because the leading track in general is at an angle compared to the jet axis, the resulting j_T values are different. In practice the jet axis found by the jet finding algorithm tends to minimize the average j_T of jet constituents. Thus the yield at high j_T is limited and the RMS values are smaller. The effect of having the leading hadron as reference instead of the jet axis is discussed in section 7.2.2

Lastly the results from the dihadron analysis are done in $p_{T\text{trigger}}$ bins. This favours hard jets, i.e. jets where the leading hadron carries a large momentum fraction and the jet multiplicity is small. In $p_{T\text{jet}}$ bins jets are more likely to be soft, i.e. small leading momentum fraction and high multiplicity jets.

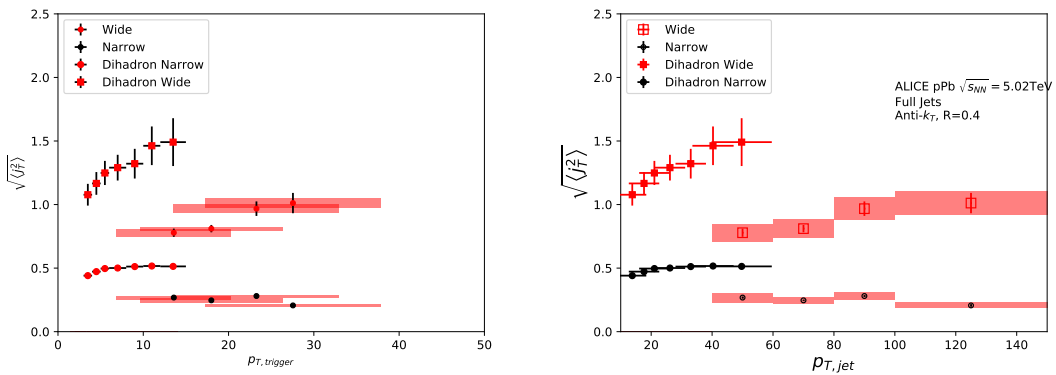


Figure 60: Jet j_T results are compared to results obtained in the dihadron analysis. Dihadron trigger p_T bins are converted to jet p_T bins using observed mean $p_{T\text{jet}}$ values in $p_{T\text{trigger}}$ bins. Dihadron results are for $0.2 < x_{||} < 0.4$

7.2.1 Different R parameters

The size of the jet cone gives a limit for j_T . For a track with a fixed momentum p this is a hard limit. This is conveniently seen as j_T can be given in terms of cone size R and momentum p in the small angle approximation limit as

$$j_T \approx p \cdot R \quad (60)$$

Thus for tracks with $p_{T\text{track}} < p_{T0}$, $j_T < p_{T0} \times R$.

2051 In practice the effect of cone sizes on j_T distribution is studied in a PYTHIA simulation.
 2052 Results of the individual distributions and resulting RMS values from this
 2053 simulation are shown in Fig. 61 and Fig. 62 respectively. Increasing the cone size
 2054 of jets gives more room for high j_T tracks. This is seen in the individual j_T distri-
 2055 butions as increased high j_T production. At low j_T there is no change.

2056 When looking at RMS values from wide component we see an increase/decrease
 2057 of about 10% when going from $R = 0.4$ to $R = 0.5/R = 0.3$.

2058 The message from narrow component RMS values is less clear. At low jet p_T
 the behaviour is similar, but at high p_T the order is reversed.

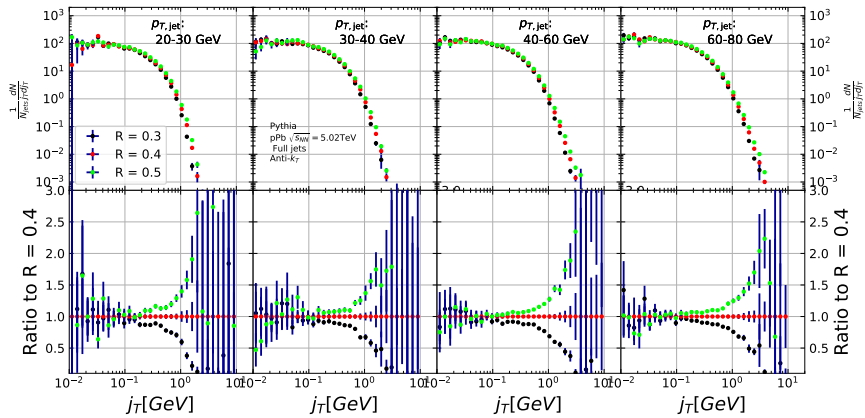


Figure 61: Effect of changing R parameter in jet finding on j_T distributions

2059

2060 7.2.2 Leading tracks versus jet

2061 The leading track is an imperfect estimate of the jet/original parton. Because the
 2062 leading track in general is at an angle compared to the jet axis, the resulting j_T
 2063 values are different. In practice the jet axis found by the jet finding algorithm
 2064 tends to minimize the average j_T of jet constituents. Thus the yield at high j_T is
 2065 limited and the RMS values are smaller.

2066 A PYTHIA study was performed where j_T was calculated with respect to the
 2067 leading track momentum, instead of the jet axis. The results are shown in Fig. 63.
 2068 The resulting j_T distributions are significantly wider than j_T distributions from
 2069 the typical method. The effect seems to be larger than the effect seen in comparing
 2070 different R values.

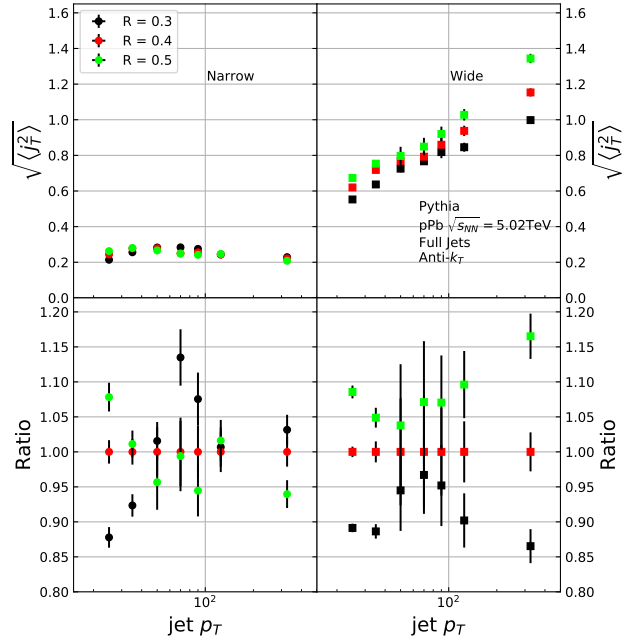


Figure 62: Effect of changing R parameter in jet finding on narrow and wide component RMS values. Wide component RMS values increase with increasing cone size.

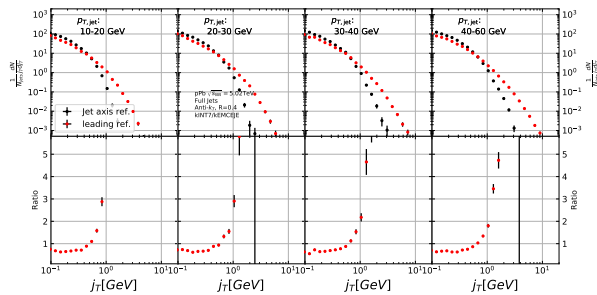


Figure 63: Results of calculating j_T with respect to the jet axis or the leading hadron. The assumption is that because the leading hadron is an imperfect estimate of the jet axis, low j_T tracks should on average be shifted to higher j_T

2071 **8 Summary**

2072 In this work two distinct j_T components were extracted for narrow and wide contri-
2073 butions using jet reconstruction in $\sqrt{s_{NN}} = 5.02$ TeV p–Pb collisions. RMS values
2074 for both components were obtained. The width of the wide component is found to
2075 increase for increasing $p_{T\text{jet}}$. This is in part explained by the changing kinemati-
2076 cal limits when going to higher $p_{T\text{jet}}$ which allows higher $p_{T\text{track}}$. Additionally the
2077 larger phase space allows stronger parton splitting. The results are qualitatively
2078 compatible with previous studies that studied j_T using two-particle correlations.

2079 [Extend summary](#)

2080 Appendices

2081 A Additional graphs

2082 **References**

- 2083 [1] ALICE, J. Adam *et al.*, Phys. Rev. **C91**, 064905 (2015), 1412.6828.
- 2084 [2] <https://alice-publications.web.cern.ch/node/3655>, 2018.
- 2085 [3] PHENIX Collaboration, K. Adcox *et al.*, Nucl.Phys. **A757**, 184 (2005), nucl-ex/0410003.
- 2086 [4] STAR Collaboration, J. Adams *et al.*, Nucl.Phys. **A757**, 102 (2005), nucl-ex/0501009.
- 2087 [5] J.-Y. Ollitrault, Phys. Rev. D **46**, 229 (1992).
- 2088 [6] U. Heinz and P. Kolb, Nucl. Phys. **A702**, 269 (2002).
- 2089 [7] E. Shuryak, Prog. Part. Nucl. Phys. **62**, 48 (2009).
- 2090 [8] ATLAS Collaboration, J. Jia, Nucl.Phys.A904-905 **2013**, 421c (2013), 1209.4232.
- 2091 [9] R. A. Lacey *et al.*, (2012), 1207.1886.
- 2092 [10] R. Bjorklund, W. Crandall, B. J. Moyer, and H. York, Phys. Review **77**, 213 (1950).
- 2093 [11] W. Heisenberg, Zeitschrift für Physik **77**, 1 (1932).
- 2094 [12] M. Gell-Mann, Phys. Rev. **125**, 1067 (1962).
- 2095 [13] M. Gell-Mann, Phys. Lett. **8**, 214 (1964).
- 2096 [14] O. Greenberg, Phys. Rev. Lett. **13**, 598 (1964).
- 2097 [15] Crystal Ball Collaboration, D. Williams *et al.*, Phys.Rev. **D38**, 1365 (1988).
- 2098 [16] W. Krolikowski, Nuovo Cim. **A27**, 194 (1975).
- 2099 [17] D. J. Gross and F. Wilczek, Physical Review Letters **30**, 1343 (1973).
- 2100 [18] H. D. Politzer, Physical Review Letters **30**, 1346 (1973).
- 2101 [19] D. J. Gross and F. Wilczek, Physical Review D **8**, 3633 (1973).
- 2102 [20] D. J. Gross and F. Wilczek, Physical Review D **9**, 980 (1974).
- 2103 [21] H. Georgi and H. D. Politzer, Physical Review D **9**, 416 (1974).

- 2108 [22] H. Fritzsch, M. Gell-Mann, and H. Leutwyler, Physics Letters B **47**, 365
2109 (1973).
- 2110 [23] I. Flegel and P. Söding, CERN courier (2004).
- 2111 [24] R. Brandelik *et al.*, Physics Letters B **86**, 243 (1979).
- 2112 [25] J. K. L. MacDonald, Phys. Rev. **43**, 830 (1933).
- 2113 [26] C. Berger *et al.*, Physics Letters B **86**, 418 (1979).
- 2114 [27] J. Collins and M. Perry, Phys. rev. Lett. **34**, 1353 (1975).
- 2115 [28] E. Shuryak, Phys. Reps. **61**, 71 (1980).
- 2116 [29] K. Rajagopal, SLAC Beam Line **31-2**, 9 (2001).
- 2117 [30] P. Kovtun, D. Son, and A. Starinets, Phys.Rev.Lett. **94**, 111601 (2005),
2118 hep-th/0405231.
- 2119 [31] R. A. Lacey *et al.*, Phys. Rev. Lett. **98**, 092301 (2007).
- 2120 [32] E. Lofgren, *ACCELERATOR DIVISION ANNUAL REPORTS, 1 JULY*
2121 *1972 12/31/1974* (, 1975).
- 2122 [33] D. S. Barton, Heavy ion program at bnl: Ags, rhic, in *Proc. 1987 Particle*
2123 *Accelerator Conference, Washington, D.C., March, 1987*, 1987.
- 2124 [34] I. Vitev and M. Gyulassy, Phys.Rev.Lett. **89**, 252301 (2002), hep-
2125 ph/0209161.
- 2126 [35] A. Kovalenko *et al.*, Status of the nuclotron, in *Proceedings of EPAC Vol. 94*,
2127 pp. 161–164, 1994.
- 2128 [36] NA61/SHINE, K. Grebieszkow, PoS **CPOD2013**, 004 (2013).
- 2129 [37] BRAHMS Collaboration, I. Arsene *et al.*, Nucl.Phys. **A757**, 1 (2005), nucl-
2130 ex/0410020.
- 2131 [38] B. Back *et al.*, Nucl.Phys. **A757**, 28 (2005), nucl-ex/0410022.
- 2132 [39] S. A. Voloshin, A. M. Poskanzer, and R. Snellings, (2008), 0809.2949.
- 2133 [40] S. A. Voloshin, A. M. Poskanzer, A. Tang, and G. Wang, Phys.Lett. **B659**,
2134 537 (2008), 0708.0800.

- ₂₁₃₅ [41] H. Holopainen, H. Niemi, and K. J. Eskola, Phys.Rev. **C83**, 034901 (2011), 1007.0368.
- ₂₁₃₇ [42] ALICE Collaboration, Phys. Rev. C **88**, 044909 (2013).
- ₂₁₃₈ [43] M. L. Miller, K. Reygers, S. J. Sanders, and P. Steinberg, Ann.Rev.Nucl.Part.Sci. **57**, 205 (2007), nucl-ex/0701025.
- ₂₁₄₀ [44] R. Glauber, Lectures in theoretical physics, 1959.
- ₂₁₄₁ [45] W. Czyż and L. Maximon, Annals of Physics **52**, 59 (1969).
- ₂₁₄₂ [46] A. Białas, M. Bleszyński, and W. Czyż, Nuclear Physics B **111**, 461 (1976).
- ₂₁₄₃ [47] PHENIX Collaboration, S. Afanasiev *et al.*, Phys.Rev. **C80**, 054907 (2009), 0903.4886.
- ₂₁₄₅ [48] J.-Y. Ollitrault, Eur.J.Phys. **29**, 275 (2008), 0708.2433.
- ₂₁₄₆ [49] P. Romatschke, Int.J.Mod.Phys. **E19**, 1 (2010), 0902.3663.
- ₂₁₄₇ [50] L. LD, Izv. Akad. Nauk Ser. Fiz. **17**, 51 (1953).
- ₂₁₄₈ [51] J. D. Bjorken, Phys. Rev. D **27**, 140 (1983).
- ₂₁₄₉ [52] G. Baym, B. L. Friman, J. P. Blaizot, M. Soyeur, and W. Czyz, Nucl. Phys. **A407**, 541 (1983).
- ₂₁₅₁ [53] H. von Gersdorff, L. McLerran, M. Kataja, and P. V. Ruuskanen, Phys. Rev. D **34**, 794 (1986).
- ₂₁₅₃ [54] K. A. *et al.* [ALICE Collaboration], Phys. Rev. Lett **106** (2011), 032301.
- ₂₁₅₄ [55] J.-Y. Ollitrault, Phys.Rev. D **48**, 1132 (1993), hep-ph/9303247.
- ₂₁₅₅ [56] P. Danielewicz and G. Odyniec, Physics Letters B **157**, 146 (1985).
- ₂₁₅₆ [57] P. Danielewicz and M. Gyulassy, Physics Letters B **129**, 283 (1983).
- ₂₁₅₇ [58] T. Abbott *et al.*, Phys. Rev. Lett. **70**, 1393 (1993).
- ₂₁₅₈ [59] S. Voloshin and Y. Zhang, Z.Phys. **C70**, 665 (1996), hep-ph/9407282.
- ₂₁₅₉ [60] E877 Collaboration, J. Barrette *et al.*, Phys.Rev.Lett. **73**, 2532 (1994), hep-ex/9405003.

- 2161 [61] V. N. Gribov and L. N. Lipatov, Sov. J. Nucl. Phys. **15**, 438 (1972), [Yad.
2162 Fiz.15,781(1972)].
- 2163 [62] G. Altarelli and G. Parisi, Nucl. Phys. **B126**, 298 (1977).
- 2164 [63] Y. L. Dokshitzer, Sov. Phys. JETP **46**, 641 (1977), [Zh. Eksp. Teor.
2165 Fiz.73,1216(1977)].
- 2166 [64] Y. I. Azimov, Y. L. Dokshitzer, V. A. Khoze, and S. I. Trovan, Zeitschrift
2167 für Physik C Particles and Fields **27**, 65 (1985).
- 2168 [65] B. Andersson, G. Gustafson, G. Ingelman, and T. Sjöstrand, Physics Reports
2169 **97**, 31 (1983).
- 2170 [66] A. Buckley *et al.*, Phys. Rept. **504**, 145 (2011), 1101.2599.
- 2171 [67] M. Bahr *et al.*, Eur. Phys. J. **C58**, 639 (2008), 0803.0883.
- 2172 [68] ALICE Collaboration, K. Aamodt *et al.*, Phys.Lett. **B696**, 30 (2011),
2173 1012.1004.
- 2174 [69] WA98 Collaboration, M. Aggarwal *et al.*, Eur.Phys.J. **C23**, 225 (2002),
2175 nucl-ex/0108006.
- 2176 [70] D. G. d'Enterria, Phys.Lett. **B596**, 32 (2004), nucl-ex/0403055.
- 2177 [71] PHENIX Collaboration, A. Adare *et al.*, Phys.Rev.Lett. **101**, 232301 (2008),
2178 0801.4020.
- 2179 [72] STAR Collaboration, J. Adams *et al.*, Phys.Rev.Lett. **91**, 172302 (2003),
2180 nucl-ex/0305015.
- 2181 [73] A. Dainese, C. Loizides, and G. Paic, Eur.Phys.J. **C38**, 461 (2005), hep-
2182 ph/0406201.
- 2183 [74] I. Vitev, J.Phys. **G30**, S791 (2004), hep-ph/0403089.
- 2184 [75] C. A. Salgado and U. A. Wiedemann, Phys.Rev. **D68**, 014008 (2003), hep-
2185 ph/0302184.
- 2186 [76] N. Armesto, A. Dainese, C. A. Salgado, and U. A. Wiedemann, Phys.Rev.
2187 **D71**, 054027 (2005), hep-ph/0501225.
- 2188 [77] T. Renk, H. Holopainen, R. Paatelainen, and K. J. Eskola, Phys.Rev. **C84**,
2189 014906 (2011), 1103.5308.

- 2190 [78] CMS Collaboration, S. Chatrchyan *et al.*, Eur.Phys.J. **C72**, 1945 (2012),
2191 1202.2554.
- 2192 [79] PHENIX Collaboration, S. Afanasiev *et al.*, Phys. Rev. C **80**, 054907 (2009).
- 2193 [80] ALICE Collaboration, K. Aamodt *et al.*, Phys.Rev.Lett. **108**, 092301 (2012),
2194 1110.0121.
- 2195 [81] R. Baier, Y. L. Dokshitzer, A. H. Mueller, S. Peigne, and D. Schiff, Nucl.
2196 Phys. **B484**, 265 (1997), hep-ph/9608322.
- 2197 [82] W. H. H. Bethe and, Proc.Roy.Soc.Lond. **A146** (1934).
- 2198 [83] L. D. Landau and I. Pomeranchuk, Dokl. Akad. Nauk Ser. Fiz. **92**, 535
2199 (1953).
- 2200 [84] A. B. Migdal, Phys. Rev. **103**, 1811 (1956).
- 2201 [85] P. Bosted *et al.*, Quantum-mechanical suppression of bremsstrahlung*, 1993.
- 2202 [86] A. Majumder and M. Van Leeuwen, Prog.Part.Nucl.Phys. **A66**, 41 (2011),
2203 1002.2206.
- 2204 [87] F. Dominguez, C. Marquet, A. Mueller, B. Wu, and B.-W. Xiao, Nucl.Phys.
2205 **A811**, 197 (2008), 0803.3234.
- 2206 [88] M. Gyulassy, P. Levai, and I. Vitev, Nucl.Phys. **B571**, 197 (2000), hep-
2207 ph/9907461.
- 2208 [89] U. A. Wiedemann, Nucl.Phys. **B588**, 303 (2000), hep-ph/0005129.
- 2209 [90] P. B. Arnold, G. D. Moore, and L. G. Yaffe, JHEP **0112**, 009 (2001), hep-
2210 ph/0111107.
- 2211 [91] X.-N. Wang and X.-f. Guo, Nucl.Phys. **A696**, 788 (2001), hep-ph/0102230.
- 2212 [92] T. Sjostrand, S. Mrenna, and P. Z. Skands, Comput.Phys.Commun. **178**,
2213 852 (2008), 0710.3820.
- 2214 [93] I. Lokhtin and A. Snigirev, Eur.Phys.J. **C45**, 211 (2006), hep-ph/0506189.
- 2215 [94] N. Armesto, L. Cunqueiro, and C. A. Salgado, Nucl.Phys. **A830**, 271C
2216 (2009), 0907.4706.
- 2217 [95] K. Zapp, G. Ingelman, J. Rathsman, J. Stachel, and U. A. Wiedemann,
2218 Eur.Phys.J. **C60**, 617 (2009), 0804.3568.

- 2219 [96] T. Renk, Phys.Rev. **C79**, 054906 (2009), 0901.2818.
- 2220 [97] PHENIX, K. Adcox *et al.*, Phys. Rev. Lett. **88**, 022301 (2002), nucl-ex/0109003.
- 2221
- 2222 [98] STAR, J. Adams *et al.*, Phys. Rev. Lett. **91**, 072304 (2003), nucl-ex/0306024.
- 2223 [99] BRAHMS, I. Arsene *et al.*, Phys. Rev. Lett. **91**, 072305 (2003), nucl-ex/0307003.
- 2224
- 2225 [100] CMS, V. Khachatryan *et al.*, JHEP **04**, 039 (2017), 1611.01664.
- 2226 [101] ALICE, S. Acharya *et al.*, JHEP **11**, 013 (2018), 1802.09145.
- 2227 [102] PHENIX, A. Adare *et al.*, Phys. Rev. **C77**, 011901 (2008), 0705.3238.
- 2228 [103] PHENIX, A. Adare *et al.*, Phys. Rev. Lett. **111**, 032301 (2013), 1212.3323.
- 2229 [104] ALICE, J. Adam *et al.*, Phys. Lett. **B746**, 1 (2015), 1502.01689.
- 2230 [105] CMS, A. M. Sirunyan *et al.*, Phys. Rev. Lett. **121**, 242301 (2018), 1801.04895.
- 2231
- 2232 [106] CMS, S. Chatrchyan *et al.*, Phys. Rev. **C90**, 024908 (2014), 1406.0932.
- 2233 [107] ALICE, S. Acharya *et al.*, JHEP **10**, 139 (2018), 1807.06854.
- 2234 [108] A. Kurkela and U. A. Wiedemann, Phys. Lett. **B740**, 172 (2015), 1407.0293.
- 2235 [109] JETSCAPE, Y. Tachibana *et al.*, Jet substructure modification in a QGP from a multi-scale description of jet evolution with JETSCAPE, 2018, 1812.06366.
- 2236
- 2237
- 2238 [110] P. Aurenche and B. G. Zakharov, Eur. Phys. J. **C71**, 1829 (2011), 1109.6819.
- 2239 [111] A. Beraudo, J. G. Milhano, and U. A. Wiedemann, Phys. Rev. **C85**, 031901 (2012), 1109.5025.
- 2240
- 2241 [112] A. Beraudo, J. G. Milhano, and U. A. Wiedemann, JHEP **07**, 144 (2012), 1204.4342.
- 2242
- 2243 [113] J. Casalderrey-Solana, Y. Mehtar-Tani, C. A. Salgado, and K. Tywoniuk, Phys. Lett. **B725**, 357 (2013), 1210.7765.
- 2244
- 2245 [114] F. D'Eramo, M. Lekaveckas, H. Liu, and K. Rajagopal, JHEP **05**, 031 (2013), 1211.1922.
- 2246

- ²²⁴⁷ [115] A. Ayala, I. Dominguez, J. Jalilian-Marian, and M. E. Tejeda-Yeomans, Phys. Rev. **C94**, 024913 (2016), 1603.09296.
- ²²⁴⁹ [116] J. L. Nagle and W. A. Zajc, Ann. Rev. Nucl. Part. Sci. **68**, 211 (2018), 1801.03477.
- ²²⁵¹ [117] E735, T. Alexopoulos *et al.*, Phys. Rev. **D48**, 984 (1993).
- ²²⁵² [118] MiniMax, T. C. Brooks *et al.*, Phys. Rev. **D61**, 032003 (2000), hep-ex/9906026.
- ²²⁵⁴ [119] C. Shen, Z. Qiu, and U. Heinz, Phys. Rev. **C92**, 014901 (2015), 1502.04636.
- ²²⁵⁵ [120] PHENIX, A. Adare *et al.*, Phys. Rev. **C94**, 064901 (2016), 1509.07758.
- ²²⁵⁶ [121] C. A. Salgado and J. P. Wessels, Ann. Rev. Nucl. Part. Sci. **66**, 449 (2016).
- ²²⁵⁷ [122] M. Gyulassy, I. Vitev, X.-N. Wang, and B.-W. Zhang, p. 123 (2003), nucl-th/0302077.
- ²²⁵⁹ [123] E. Norbeck, K. Šafařík, and P. A. Steinberg, Annual Review of Nuclear and Particle Science **64**, 383 (2014), <https://doi.org/10.1146/annurev-nucl-102912-144532>.
- ²²⁶² [124] A. Accardi, F. Arleo, W. K. Brooks, D. D'Enterria, and V. Muccifora, Riv. Nuovo Cim. **32**, 439 (2010), 0907.3534.
- ²²⁶⁴ [125] 2019.
- ²²⁶⁵ [126] P. M. Watkins, Contemp. Phys. **27**, 291 (1986).
- ²²⁶⁶ [127] Cern experiments, 2019.
- ²²⁶⁷ [128] O. S. Brüning *et al.*, *LHC Design Report*CERN Yellow Reports: Monographs (CERN, Geneva, 2004).
- ²²⁶⁹ [129] ATLAS, G. Aad *et al.*, Phys. Lett. **B716**, 1 (2012), 1207.7214.
- ²²⁷⁰ [130] CMS, S. Chatrchyan *et al.*, Phys. Lett. **B716**, 30 (2012), 1207.7235.
- ²²⁷¹ [131] LHCb, A. A. Alves, Jr. *et al.*, JINST **3**, S08005 (2008).
- ²²⁷² [132] TOTEM, G. Anelli *et al.*, JINST **3**, S08007 (2008).
- ²²⁷³ [133] T. ALICE Collaboration *et al.*, Journal of Instrumentation **3**, S08002 (2008).
- ²²⁷⁴ [134] ALICE, G. Dellacasa *et al.*, (2000).

- ²²⁷⁵ [135] ALICE, G. Dellacasa *et al.*, (1999).
- ²²⁷⁶ [136] ALICE, I. Belikov, EPJ Web Conf. **125**, 01004 (2016), 1607.01171.
- ²²⁷⁷ [137] ALICE Collaboration, B. Abelev *et al.*, CERN Report No. CERN-LHCC-2012-012. LHCC-I-022. ALICE-UG-002, 2012 (unpublished).
- ²²⁷⁸
- ²²⁷⁹ [138] Report No. CERN-LHCC-2015-001. ALICE-TDR-018, 2015 (unpublished).
- ²²⁸⁰ [139] The ALICE Collaboration, Report No. CERN-LHCC-2013-020. ALICE-TDR-016, 2013 (unpublished).
- ²²⁸¹
- ²²⁸² [140] M. Vargyas, *Jet shape modification in Pb-Pb collisions at $\sqrt{s_{NN}} = 2.76 \text{ TeV}$ using two-particle correlations*, PhD thesis, University of Jyväskylä, 2018.
- ²²⁸³
- ²²⁸⁴ [141] ALICE Collaboration, P. Cortese, *ALICE transition-radiation detector: Technical Design Report*Technical Design Report ALICE (CERN, Geneva, 2001).
- ²²⁸⁵
- ²²⁸⁶
- ²²⁸⁷ [142] ALICE, G. Dellacasa *et al.*, (2000).
- ²²⁸⁸ [143] ALICE, S. Beole *et al.*, (1998).
- ²²⁸⁹ [144] for the ALICE, C. Zampolli, Particle Identification with the ALICE detector at the LHC, in *Proceedings, PLHC2012: Physics at the LHC 2012 (PLHC2012): Vancouver, BC, Canada, June 4-9, 2012*, 2012, 1209.5637.
- ²²⁹⁰
- ²²⁹¹
- ²²⁹² [145] ALICE, G. Dellacasa *et al.*, (1999).
- ²²⁹³ [146] ALICE, P. Cortese *et al.*, (2008).
- ²²⁹⁴ [147] J. Allen *et al.*, Report No. CERN-LHCC-2010-011. ALICE-TDR-14-add-1, 2010 (unpublished).
- ²²⁹⁵
- ²²⁹⁶ [148] ALICE, P. Cortese *et al.*, (2004).
- ²²⁹⁷ [149] ALICE, A. I. Maevskaya, (2018), 1812.00594.
- ²²⁹⁸ [150] ALICE Collaboration, *ALICE Photon Multiplicity Detector (PMD): Technical Design Report*Technical Design Report ALICE (CERN, Geneva, 1999).
- ²²⁹⁹
- ²³⁰⁰ [151] ACORDE, A. Fernández *et al.*, Nucl. Instrum. Meth. **A572**, 102 (2007), physics/0606051.
- ²³⁰¹
- ²³⁰² [152] ALICE, G. Dellacasa *et al.*, (1999).
- ²³⁰³ [153] ALICE, S. Beole *et al.*, (1996).

- 2304 [154] J. Král, *Intrinsic transverse momentum distribution of jet constituents in*
2305 *p-Pb collisions at ALICE*, PhD thesis, University of Jyväskylä, 2014.
- 2306 [155] J. Kral, T. Awes, H. Muller, J. Rak, and J. Schambach, Nuclear Instruments
2307 and Methods in Physics Research Section A: Accelerators, Spectrometers,
2308 Detectors and Associated Equipment **693**, 261 (2012).
- 2309 [156] ALICE, K. Aamodt *et al.*, JINST **3**, S08002 (2008).
- 2310 [157] ALICE, B. B. Abelev *et al.*, Int. J. Mod. Phys. **A29**, 1430044 (2014),
2311 1402.4476.
- 2312 [158] ALICE, K. Aamodt *et al.*, JINST **5**, P03003 (2010), 1001.0502.
- 2313 [159] J. Alme *et al.*, Nucl. Instrum. Meth. **A622**, 316 (2010), 1001.1950.
- 2314 [160] R. Fruhwirth, Nucl. Instrum. Meth. **A262**, 444 (1987).
- 2315 [161] ALICE, B. Abelev *et al.*, JHEP **03**, 053 (2012), 1201.2423.
- 2316 [162] ALICE, B. Abelev *et al.*, Phys. Lett. **B719**, 29 (2013), 1212.2001.
- 2317 [163] M. Cacciari, G. P. Salam, and G. Soyez, Eur. Phys. J. **C72**, 1896 (2012),
2318 1111.6097.
- 2319 [164] M. Cacciari, G. P. Salam, and G. Soyez, JHEP **04**, 063 (2008), 0802.1189.
- 2320 [165] T. Sjöstrand, S. Mrenna, and P. Z. Skands, Comput. Phys. Commun. **178**,
2321 852 (2008), 0710.3820.
- 2322 [166] Roounfold: Root unfolding framework, <http://hepunx.rl.ac.uk/~adye/software/unfold/RooUnfold.html>, 2013.
- 2324 [167] CMS, S. Chatrchyan *et al.*, Phys. Rev. **D90**, 072006 (2014), 1406.0324.
- 2325 [168] M. Dasgupta, L. Magnea, and G. P. Salam, JHEP **02**, 055 (2008), 0712.3014.